Characterization of interface adhesion and acoustic attenuation in multilayer systems

Doctoral thesis for obtaining the

academic degree Doctor of

Natural Sciences

(Doctor rerum naturalium)

submitted by

Martin Großmann

at the

Faculty of Sciences

Department of Physics

Konstanz, 2017

Date of the oral examination: October 27, 2017

1. Reviewer: Prof. Dr. Thomas Dekorsy

2. Reviewer: Prof. Dr. Vitalyi Gusev

Contents

Chapter 1

Introduction

Everything you see exists together in a delicate balance.
[...] you need to understand that balance [...].
- Mufasa (*The Lion King*)

Everybody has an idea of the concept of temperature. This, however, is mostly the effect of heat conduction between the surroundings (air) and a sensor (skin). As described by Fourier's law, heat flows from a region of higher temperature to a region of lower temperature. To explain heat conduction microscopically different fields of physics, like crystallography, statistical mechanics, and quantum mechanics must be combined. In this thesis heat transfer by atomic interactions is investigated, e.g. the exchange of energy and momentum between the atom masses – leading to macroscopic vibrations. The energy quanta of these macroscopic vibrations of a monochromatic lattice wave are called phonons in analogy to photons as the energy quanta of light.

The temperature T of a solid in equilibrium can be described by the average kinetic energy of its atoms. Every atom oscillates around its lattice's equilibrium position (even when approaching T=0 K) with no correlation to each other. Those vibrations are out of phase and incoherent. These so-called thermal phonons are populated with an average energy of $k_B T$ (determined by the Bose-Einstein distribution with k_B the Boltzmann constant), which corresponds to an average phonon frequency of $f_{th} = 6.1\,\mathrm{THz}$ at room temperature. However, the incoherent and broad frequency spectrum prevents a good insight into fundamental mechanical properties and processes. It is like studying photons emitted from a light bulb without the possibility to look at the different wavelengths (colors) individually.

Coherent phonons are used to further investigate these phenomena. In the low frequency range from 16 to 20 kHz phase stable oscillations can be launched into the surroundings relatively easily: by speaking. It can be done in the ultrasonic regime starting at 20 kHz by electronic coupling of a generator to a substrate for up to 10 GHz at which point the electronic speeds become limited. Additionally, in the hypersonic frequency range above 1 GHz, where thermal phonons start to excite the vibrational states, different methods have to be found.

A common technique for the excitation and detection of coherent acoustic phonons is optical femtosecond pump-probe time-domain spectroscopy (often referred to as picosecond ultrasonics) [Mat15]. A short pump laser pulse rapidly changes the electronic equilibrium and thus also the

atomic equilibrium in a sample thereby generating coherent phonons. The temporal evolution is then probed by a time-delayed laser pulse. Depending on the absorption profile of the pump pulse the initial phonon spectrum can be tailored. Different mechanical material properties can be extracted non-destructively: speed of sound, dissipation, scattering intensities at boundaries like (rough) surfaces and interfaces, and adhesion of thin films.
Intrinsic damping properties for phonons at those high frequencies and extrinsic effects of roughness and interfacial features are not very well-known for most materials [Maz13, Cuf13]. Today, this topic is of great importance for thermoelectric materials and the semiconductor industry. Computer processors are fabricated mostly out of Si, the main material investigated in this thesis. As an example, processors' transistors are already as small as 5 nm in size leading to a large surface to volume ratio which leads to a high impact of the surface on thermal properties [Ant]. Phonon-boundary scattering (reflection, transmission, dephasing) has to be taken into account. But also phonon-phonon scattering has to be considered as the lifetimes of the individual modes depend strongly on the available (given by the sample geometry) decay processes. By understanding these effects, it will be possible to manipulate and control phonon transport and tailor nanoscopic structures to the desired performance.
This thesis advances some of these topics. First, the principles of phonons in solids are discussed in Chapter 2. After the introduction of the necessary mathematical tools and terms the description of coherent acoustic phonons at bulk, surfaces and interfaces is given. Thin plate and bilayer eigenmodes are derived and discussed. Additionally, phonon dissipation mechanisms are covered and a method for the numerical solution of the wave equation is presented. In Chapter 3 the generation, propagation and detection of coherent acoustic phonons is reviewed for metals and semiconductors. Here, the focus is on bilayer interfaces with perfect and imperfect adhesion, analyzed by employing a spring model. In Chapter 4 the experimental setup, principles of pump-probe measurements and sample fabrication techniques are introduced.
Thereafter the experimental results obtained in this thesis are presented. Phonon lifetime measurements of acoustic mechanical eigenmodes in surface-roughened membranes are presented in Chapter 5. In Chapter 6 acoustic pulses and in particular acoustic frequency combs confined in bilayer systems are investigated in great detail, allowing quantitative values for adhesion, intrinsic damping, thicknesses, and impedances to be found. This is followed by a discussion of guided acoustic waves in a Si membrane in Chapter 7. Optical phonons of multilayers of nanosheets of tin diselenide ($SnSe_2$) are investigated in Chapter 8.
At last, the results are summarized individually, a short conclusion connects the different topics, and an outlook of promising further investigations is given. Material parameters, a list of publications and indispensable acknowledgments are collected in the Appendix.

Chapter 2

The principles of mechanics in solids

2.1. Introduction

Acoustics is the study of mechanical waves in solids, liquids or gases. Solid state materials are composed of atoms, which are normally seen as rigid in their atomic lattice. But, upon displacing individual atoms from their equilibrium position restoring forces become apparent trying to equilibrate the system. The restoring forces between atoms and the moment of inertia of the atoms lead to the phenomena discussed in the following sections. The superposition of many atoms moving together leads to oscillations extending over several units cells which are called phonons. The occurring vibrations can be in phase between the neighboring atoms (acoustic phonons) or out-of-phase between neighboring atoms (optical phonons). As the wavelengths of the acoustic phonons are much larger than the distance between the individual atoms, the material can be described as a continuum.
In this chapter the theory regarding longitudinal acoustic phonons propagating in two-layer systems including different kinds of adhesion will be discussed. First, to introduce the necessary nomenclature, the linear theory of elasticity in continuum mechanics will be discussed. Then, in comparison to light ray propagation, the equation of motion for the displacement field will be solved and the boundary and continuity conditions are stated. After those effects of sound propagation in bulk and confinement in one direction will be discussed. First, the effects of confinement of a material in one dimension to form a thin plate - with the acoustic waves traveling guided between both surfaces - is deduced. Afterwards two materials are brought together and the reflection and transmission coefficients at that interface are derived including the spectral transformation an acoustic pulse undergoes upon reflection on/in a thin film. In detail the eigenmodes of a bilayer are evaluated and phenomena, which are induced by the quantization of modes, are discussed. It follows the theoretical and mathematical implementation of dissipation in a mechanical system. Finally, a finite difference time domain (FDTD) method for the numerical solution of the wave equation is introduced.

2.2. Linear elasticity

In this section the necessary mathematical tools will be developed to describe the occurring phenomena. Further details can be found in references [Aul73a, Cle03]. First, the displacement of an arbitrary particle A in the atomic lattice at point $\vec{r}$ to the point $\vec{q}$ is described. This is shown in Fig. 2.1. The displacement is given by: $\vec{u}(\vec{r},t) = \vec{q} - \vec{r}$. However, in order to describe

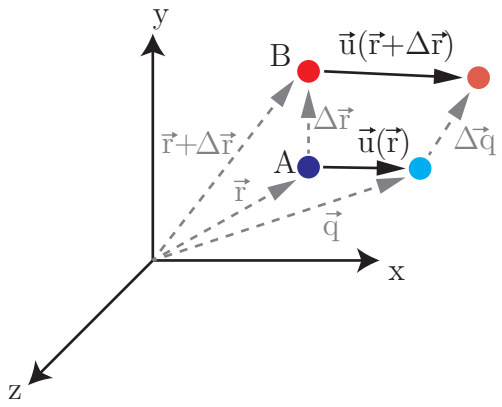

Figure 2.1.: Particle positions in equilibrium and at an arbitrary displaced position.

acoustic phenomena (e.g. vibrations and waves) it is not sufficient to describe the displacement of just one particle. Instead, the relative displacement between different atoms is of importance. Consider two atoms A and B, where A is at the position $\vec{r}$ and B is at $\vec{r}+\Delta\vec{r}$. By deforming the material in which the atoms are embedded, atom A will be displaced by $\vec{u}(\vec{r})$ while atom B will be displaced by $\vec{u}(\vec{r}+\Delta\vec{r})$. After the deformation the relative displacement $\Delta\vec{u}$ between the two atoms can be written as: $\Delta\vec{u} = \vec{u}(\vec{r}+\Delta\vec{r}) - \vec{u}(\vec{r})$. By expanding $\vec{u}(\vec{r}+\Delta\vec{r})$ in a Taylor series in dependence of $\Delta\vec{r}$ and neglecting higher orders, one gets for the relative displacement of each component:

$$\Delta u_i = \sum_j \partial_j u_i \, \Delta r_j \qquad (i,j = x,y,z) \tag{2.1}$$

This can be rewritten in tensor notation:

$$\Delta\vec{u} = \mathbf{D}\Delta\vec{r} = (\varepsilon + \Omega)\Delta\vec{r} \tag{2.2}$$

with $\mathbf{D} = \nabla\vec{u}$, which can be separated in a symmetric part ε and an asymmetric part Ω. The tensor ε is called the symmetric *strain tensor*. It does not describe rotational deformations but longitudinal and transverse:

$$\varepsilon_{ij} = \frac{1}{2}\left(\partial_i u_j + \partial_j u_i\right). \tag{2.3}$$

To illustrate the meaning of strain in one dimension the example of the deformation of a thin plate or membrane is considered in Fig. 2.2. The membrane is dilated (see the explanation of stress below) from the equilibrium thickness L to the thickness $L+\Delta L$, leading to the relative

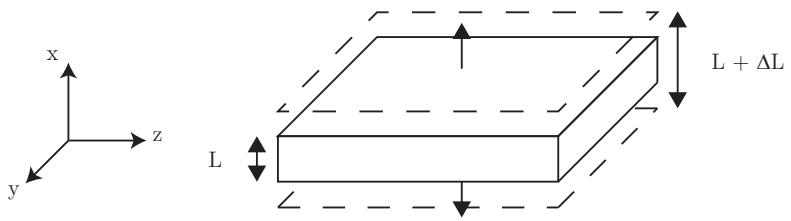

Figure 2.2.: Membrane dilatation due to strain from thickness L to thickness $L+\Delta L$.

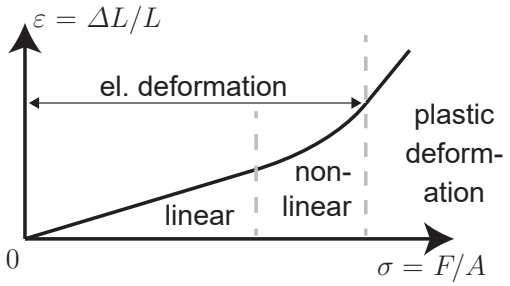

Figure 2.3.: Typical stress-strain-curve.

thickness change $\frac{\Delta L}{L}$. By placing the origin in the center of the membrane, a particle at $x = x_0$ will be displaced to $x_0(1 + \frac{\Delta L}{2L})$ and one can write for the displacement u of this particle: $u_x(x_0) = \frac{\Delta L}{L} x_0$. This yields for the strain:

$$\varepsilon = \partial_x \vec{u}(x) = \frac{\Delta L}{L} \tag{2.4}$$

In conclusion, the strain in one dimension is equal to the relative change in length. In this thesis most occurring effects can be explained using a one dimensional approach.
In general a body will be deformed - strain will be induced - by stress. The stress tensor σ is the ratio of the applied force over unit area:

$$\sigma_{ij} = \frac{F_j}{A_i}, \tag{2.5}$$

where the indices i, j correspond to one of the three principle directions x, y, z (e.g. of an ideal cube). In the case of the membrane the stress would be a force acting on the surfaces and pulling perpendicular to the surfaces. This is called normal stress. In the other case of the force acting in-plane to the surface, it is called shear or transverse stress.
In Fig. 2.3 a typical stress-strain-curve is plotted. A small stress will deform a body linearly while the additional emerging internal restoring forces of a larger stress will deform a body non-linearly. When the stress is reduced, the system will relax to equilibrium. But after a certain stress or strain threshold the elastic regime will be left and irreversible plastic deformations will occur. The elastic linear relation in the beginning is described by the generalized Hooke's law: $\sigma = \mathbf{C}\varepsilon$, with $\mathbf{C}$ the stiffness tensor of fourth order. The tensor can be reduced to a tensor of second order with six components using symmetry relations. This leads to the notation which is used in the rest of this work:

$$\vec{\sigma} = \mathbf{C}\vec{\varepsilon}, \tag{2.6}$$

where the stress and strain vectors have six components each and the stiffness tensor is the elastic modulus.
With the now established formalism it is possible to find the time and space dependencies for the deformation. To simplify the calculation, the behavior for the one dimensional case in the x direction is discussed. One can discretize the equation of motion given by Newton's law: $d\vec{F} = dm\partial_t^2 \vec{u}$, with $dm = \rho A_x dx$ for normal stress and $dm = \rho A_x dy$ for shear stress, where

dm is the differential mass and ρ is the density. This gives for the differential stress (from Eq. (2.5)):

$$\frac{d\sigma_x}{dx} = \rho\partial_t^2 u \qquad \frac{d\sigma_y}{dx} = \rho\partial_t^2 u, \tag{2.7}$$

where $\sigma_{x,y}$ stand for the normal and shear stress, respectively.

By assuming an isotropic and homogeneous medium one can simplify the bulk modulus to the two components C_{11} and C_{44}. Then one obtains with Hooke's law (Eq. (2.6)) and Eq. (2.4) the wave equations for the displacements of a longitudinal and transverse wave, respectively:

$$C_{11}\frac{d^2u_x}{dx^2} = \rho\partial_t^2 u_x \qquad C_{44}\frac{d^2u_y}{dx^2} = \rho\partial_t^2 u_y. \tag{2.8}$$

To solve the wave equation a plane wave is assumed: $u_i = \tilde{u}_i e^{i(kx-\omega t)}$, where $\tilde{u}_i$ is the amplitude of the wave in x-, y- or z-direction, ω is the frequency of the wave, and k is the wave vector. In the linear approximation phase and group velocity are identical. This yields for the longitudinal (v_L) and transverse (v_T) speeds of sound:

$$v_\mathrm{L} = \frac{\omega}{k_\mathrm{L}} = \sqrt{\frac{C_{11}}{\rho}} \qquad v_\mathrm{T} = \frac{\omega}{k_\mathrm{T}} = \sqrt{\frac{C_{44}}{\rho}} \tag{2.9}$$

The displacement of longitudinal/transverse waves is parallel/perpendicular to the propagation direction. In general in a solid medium the transverse speed of sound is smaller than the longitudinal speed of sound due to the different bulk moduli ($C_{44} < C_{11}$).

If stress is applied from outside the system, the corresponding excitation leads to an additional source term for the stress relations: $\sigma_\mathrm{source}(x,t)$. To simplify the relation and nomenclature the scalar C for the bulk modulus and the scalar u for the displacement are used. It can be either longitudinal or transverse. This changes the wave equation to

$$\rho\partial_t^2 u - C\frac{d^2u}{dx^2} = \partial_x\sigma_\mathrm{source}(x,t). \tag{2.10}$$

The solution of this wave equation is discussed in Section 3.4, where the boundary conditions (see Section 2.3) have to be taken into account. The physical origin of the source term will be discussed in Section 3.3.

2.3. Boundary and continuity conditions

Solving the equation of motion in semi-infinite spaces or layered structures with interfaces is more complex and the respective boundary conditions have to be included. The boundary conditions apply to the stress, the velocity of the particles and to the deformation of the system. Next, the cases of the following spatial regimes will be discussed: at surfaces, at perfect interfaces and at imperfect interfaces. As depicted in Figure 2.4 the air layer will be denoted with the index *air* and two other solid layers with the indices 1 and 2.

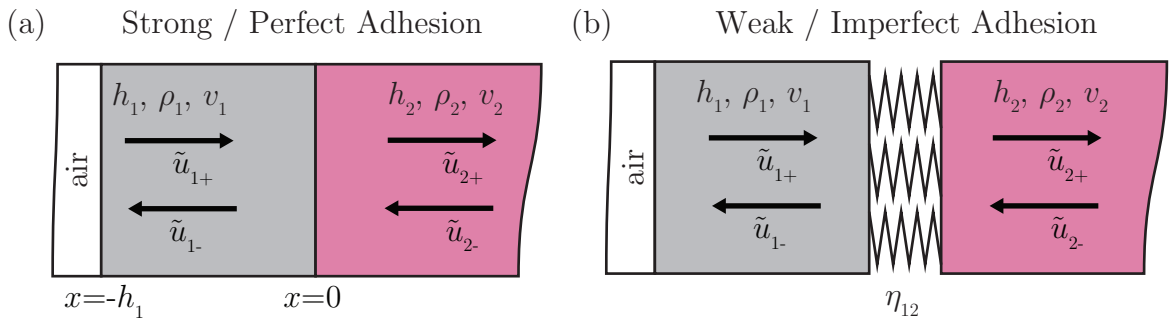

Figure 2.4.: Schematic of the structure used in the theory, including 3 layers (air, material 1 and half-infinite material 2) with the corresponding acoustic waves. (a) Two layers perfectly adhered to each other. (b) Two layers weakly adhered to each other by a massless spring.

2.3.1. Surface continuity

At a surface between air and solid 1 the mechanical wave inside the solid cannot couple to the air or vacuum. As there is no resistance from the air-layer, the surface has to be stress free:

$$\sigma_1(x_{\text{surface}}) = 0. \tag{2.11}$$

2.3.2. Perfect interfaces

At perfect interfaces the coupling between the particles is considered to be perfect. This leads to the condition that the velocity at the interface has to be continuous. This, however, implies that the deformation at the interface has to be continuous:

$$u_1(x_{\text{interface}}) = u_2(x_{\text{interface}}). \tag{2.12}$$

Additionally, for the deformation on both sides to be equal, the stress has to be equal:

$$\sigma_1(x_{\text{interface}}) = \sigma_2(x_{\text{interface}}). \tag{2.13}$$

2.3.3. Imperfect interfaces

At imperfect interfaces each surface is able to move individually only dependent on the coupling. This removes the boundary condition Eq. (2.12). Instead, adhesion is described by a massless spring model. From Hooke's law for a spring ($F = -kx$, where k is the spring constant between two particles), this yields for the stress in the spring:

$$\sigma_{\text{spring}} = -\frac{k}{A}\Delta u = -\eta_{12}\Delta u, \tag{2.14}$$

with η_{12} the spring constant per unit area at the interface between the adhered materials with the spatial separation Δu. The pressure induced by the spring is equal to the stress at each side of the interface: $\sigma_{\text{spring}} = \sigma_{1,2}(x_{\text{interface}})$.

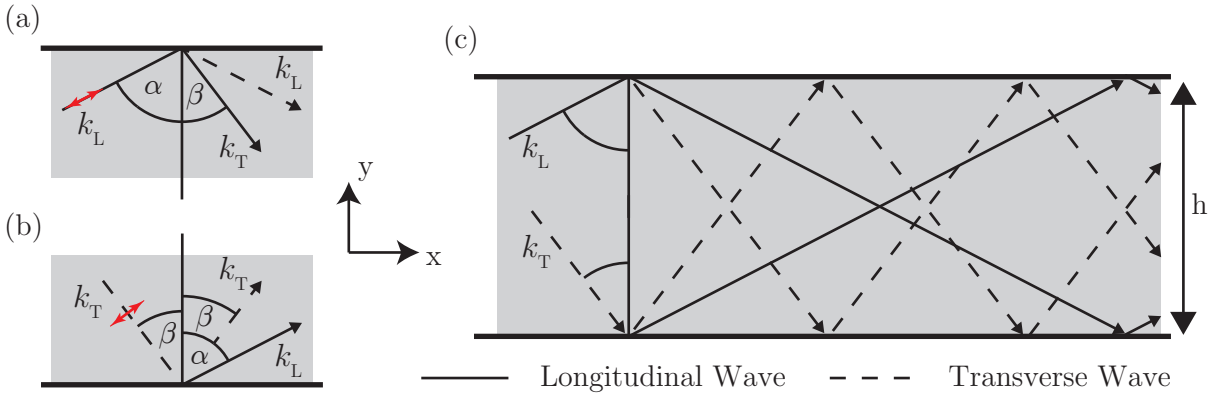

Figure 2.5.: Illustration of reflection at oblique incidence at (a,b) one surface and (c) a thin plate. (a) denotes the reflection of a longitudinal wave and (b) the reflection of a shear wave. (c) Superposition of both processes.

2.4. Lamb waves

So far only acoustic waves in an infinite or half-infinite medium with no boundaries were reviewed. Here, the case of propagation in a two dimensional structure is discussed, which is confined in one direction by two surfaces (see Fig. 2.5). This topic is extensively discussed in the literature [Vik67, Aul73a, Aul73b, Her74, Gra75, Ros00, Cle03]. In Fig. 2.5(a) a longitudinal wave is incident under an angle α onto the air-surface boundary. Due to momentum conservation the wave will be reflected at the same angle α. But a part will also be converted to a shear wave. This can be seen from the boundary condition since the surface has to be stress free. The surface continuity Eq. (2.11) means that the component of the wave vector parallel to the surface is continuous. Without loss of generality this component is chosen to be the $k_x = k_\mathrm{L} \sin\alpha$-component. But in an acoustic medium it is also possible to find an angle β at which for the same partial wave vector k_x a transverse wave can be found $k_x = k_\mathrm{T} \sin\beta$. For the relation between both angles the acoustic Snell's law yields:

$$v_\mathrm{L} \sin\alpha = v_\mathrm{T} \sin\beta \tag{2.15}$$

Due to the different sound velocities for longitudinal and transverse waves, a longitudinal wave will excite a transverse wave component upon reflection at a boundary at oblique incidence. Also a transverse wave will excite a longitudinal wave component at such reflection (see Fig. 2.5(b)). Both above discussed processes are overlapped in Fig 2.5(c). By introducing a second parallel boundary the acoustic waves will be reflected inside the thin plate with the presumption of mode conversion. Propagating waves in a membrane have to consist of longitudinal waves and shear waves polarized in the plane perpendicular to the plate and parallel to the propagation direction (SV waves). Shear waves perpendicular to that plane (SH waves) are not of interest here, as they do not influence the surfaces.
The evolving waves are called Lamb waves. The dispersion relation is described by a coupled system of a wave propagating with the wave vector k_x in x-direction and a standing wave in y-direction. Due to momentum conservation and the different speeds of sound for the longitudinal and transverse waves, the wave vectors in the y-direction are also different. The decomposition

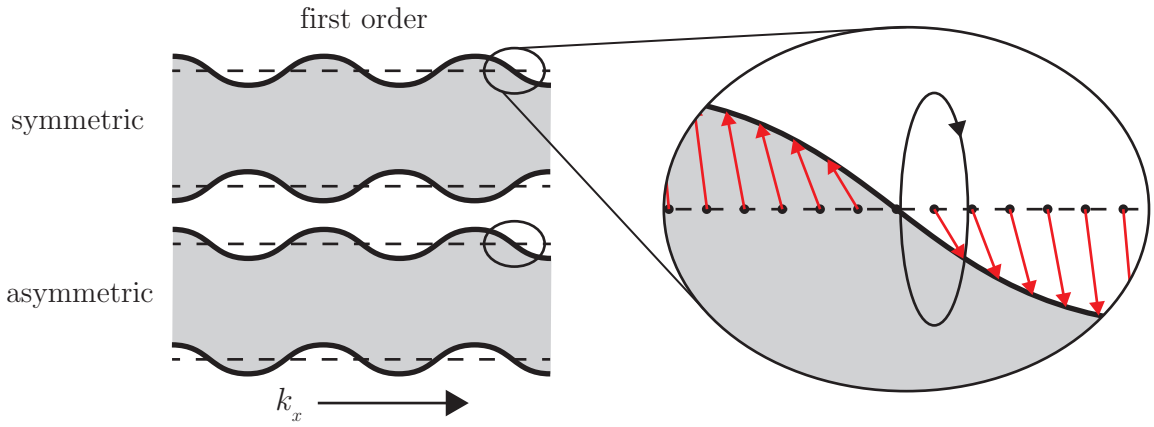

Figure 2.6.: First order Lamb wave in a thin plate. The arrows indicate the displacement. Each surface point moves in an elliptical manner (right part).

leads to:

$$k_{\mathrm{L}x}^2 + k_{\mathrm{L}y}^2 = k_{\mathrm{L}}^2 = \left(\frac{\omega}{v_{\mathrm{L}}}\right)^2 \qquad k_x^2 + k_{\mathrm{T}y}^2 = k_{\mathrm{T}}^2 = \left(\frac{\omega}{v_{\mathrm{T}}}\right)^2 \tag{2.16}$$

The number of standing waves in the y-direction gives the mode number N. The relative position of both surfaces in comparison to the median plane gives the symmetry. If both surfaces move in the same direction the mode is symmetric and if both surfaces move opposite to each other the mode is asymmetric. This is depicted in Figure 2.6. Additionally, the movement of individual points on the surface is shown. Each point moves in an elliptical manner. This is a direct consequence of the superposition of longitudinal and transverse waves.

One can now express the frequency equation, which is dependent on the thickness of the plate, the individual longitudinal and transverse wave vectors in y-direction, and the uniform wave vector k_x in x-direction [Gra75]. For symmetric waves one obtains:

$$\frac{\tan(\frac{1}{2}k_{\mathrm{T}y}h)}{\tan(\frac{1}{2}k_{\mathrm{L}y}h)} = -\frac{4k_x^2 k_{\mathrm{L}y}k_{\mathrm{T}y}}{(k_{\mathrm{T}y}^2 - k_x^2)^2} \tag{2.17}$$

and for asymmetric waves:

$$\frac{\tan(\frac{1}{2}k_{\mathrm{T}y}h)}{\tan(\frac{1}{2}k_{\mathrm{L}y}h)} = -\frac{(k_{\mathrm{T}y}^2 - k_x^2)^2}{4k_x^2 k_{\mathrm{L}y}k_{\mathrm{T}y}} \tag{2.18}$$

These relations are called the Rayleigh-Lamb frequency equations.

Despite the simple appearance, they are not analytically solvable. Numerically, however, it is possible to find the roots for a given frequency. The results for Si in the [110]-direction are shown in Fig. 2.7. The direction perpendicular to the plate is chosen along the [100]-direction. A dense mode spectrum is visible.

In the following, three different regimes are discussed: i) no propagating waves ($k_x = 0$), ii) propagating waves ($k_x \neq 0$), and iii) the half infinite space ($k_x h >> 0$):

i) $k_x = 0$: In the case of no propagation of the acoustic wave parallel to the plane, the frequency equations turn into:

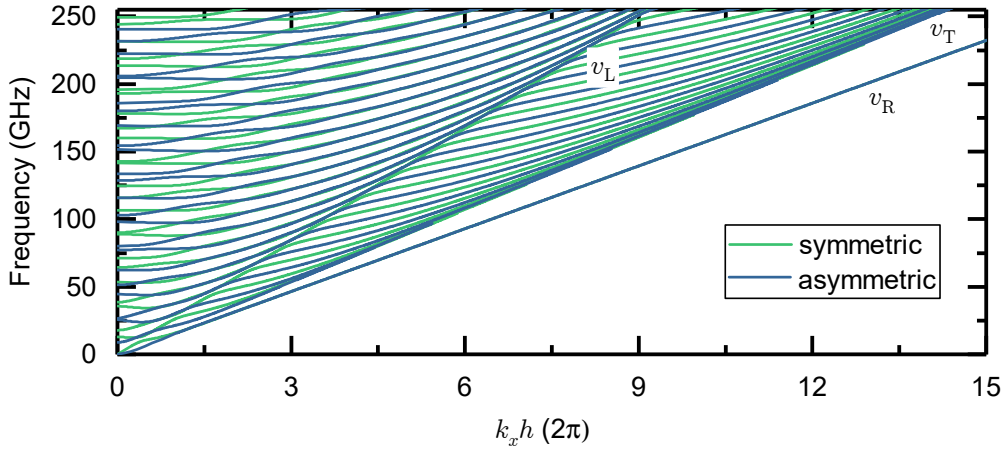

Figure 2.7.: The dispersion relation of Lamb modes in Si along the [110]-direction. The x-axis is scaled with the thickness $h/2\pi$. The developing slopes are labeled with their corresponding terminal velocity: longitudinal speed of sound v_L, transverse speed of sound v_T, and Rayleigh (surface acoustic wave) speed of sound v_R. The black lines mark symmetric and the red lines mark asymmetric modes.

$$\text{symmetric: } \frac{\tan(\frac{1}{2}k_\mathrm{T}h)}{\tan(\frac{1}{2}k_\mathrm{L}h)} = 0 \qquad \text{and} \qquad \text{asymmetric: } \frac{\tan(\frac{1}{2}k_\mathrm{L}h)}{\tan(\frac{1}{2}k_\mathrm{T}h)} = 0. \tag{2.19}$$

The solutions can now be found analytically. For the symmetric displacements:

$$k_\mathrm{T}h = N\pi \qquad (N = 0, 2, 4, ...) \qquad\qquad k_\mathrm{L}h = N\pi \qquad (N = 1, 3, 5, ...)$$

For the asymmetric displacements:

$$k_\mathrm{L}h = N\pi \qquad (N = 0, 2, 4, ...) \qquad\qquad k_\mathrm{T}h = N\pi \qquad (N = 1, 3, 5, ...)$$

In the y-direction either purely longitudinal or purely transverse acoustic modes exist. This is in correspondence with Snell's law, as there occurs no mode conversion upon normal reflection at a surface. It is noteworthy that for both longitudinal and transverse waves the symmetry changes with mode number and symmetric and asymmetric displacements occur alternating. This is shown in Fig. 2.8. The mode number N depicts the number of changes of the displacement directions. Contrary to the complex behavior of the dispersion relation, the mode spacing is equidistant. For the longitudinal wave the ground mode is a translation of the whole plate, while the first harmonic leads to a thickness change of the plate.

ii) $k_x \neq 0$: The propagating waves are guided waves between two surfaces and exhibit a complex dispersion relation with group velocity and phase velocity independent of each other. In principle, an increase in frequency is correlated with an increasing wave vector. Also for smaller wave vectors symmetrical and asymmetrical modes cross, while for larger wave vectors they overlap. An accumulation at the linear dispersion relation of longitudinal waves is visible. After that regime a splitting at regular intervals happens until the modes accumulate again at the linear dispersion of transverse waves.

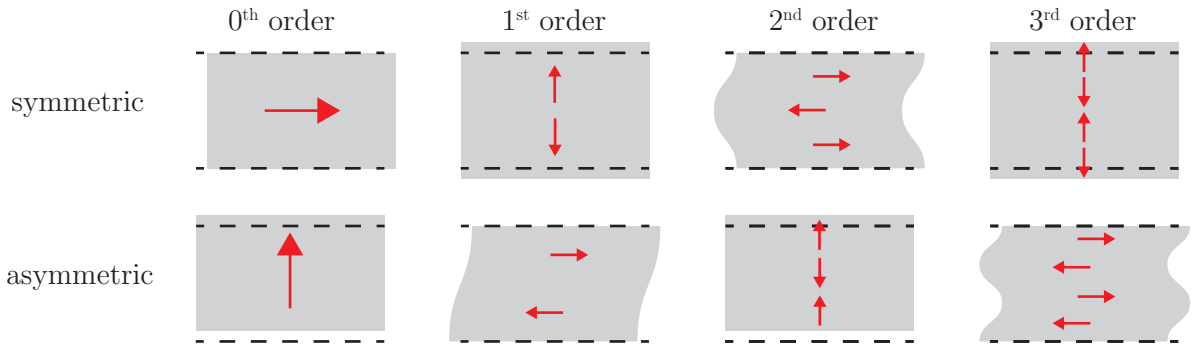

Figure 2.8.: The first 4 occurring modes in a thin plate with the wave vector perpendicular to the plate. The dashed lines show the equilibrium position, while the grey area depicts the distorted plate segment. The arrows indicate the individual displacement.

iii) $k_x h >> 0$: The thickness is much larger than the wavelength and the surfaces are decoupled. This situation can be described with surface waves on a half infinite plate. Those were first described by Lord Rayleigh and correspond to the first asymmetric and symmetric modes, which have the speed of sound v_R. v_R is smaller than the longitudinal and transverse speeds of sound. This leads to an imaginary part of the y-component of the wave vector. Hence, an exponential decay away from the surface occurs, which stems not from dissipation processes, but, intrinsically from the boundary conditions.

2.5. Reflection and transmission at interfaces

To calculate the reflection and transmission coefficients at a distinct interface the evaluated formalism and the boundary conditions introduced above will be used. First the case of perfect adhesion is discussed, then imperfect adhesion, modeled by a spring bonding, and, finally, the spectral transfer function of a thin layer on an incident acoustic pulse is described.

2.5.1. Reflection and transmission coefficients with perfect adhesion

The schematic of two layers perfectly bonded to each other is shown in Fig. 2.9(a). Only the waves u_{1+}, the reflected wave u_{1-}, and the transmitted wave u_{2+} are considered. The layers are perfectly adhered. The wave incident on the interface from layer 1 can be written in the form of:

$$u_{1+} = \tilde{u}_{1+} e^{i(k_1 x - \omega t)},$$

with the mechanical displacement $\tilde{u}_{1+}$, the frequency ω, the time t and the wave number k_1. The minus in front of the wave number denotes the propagation in positive x-direction. The reflected wave u_{1-} has the reversed sign and a different amplitude, to consider the reversed propagation direction:

$$u_{1-} = \tilde{u}_{1-} e^{-i(k_1 x + \omega t)}.$$

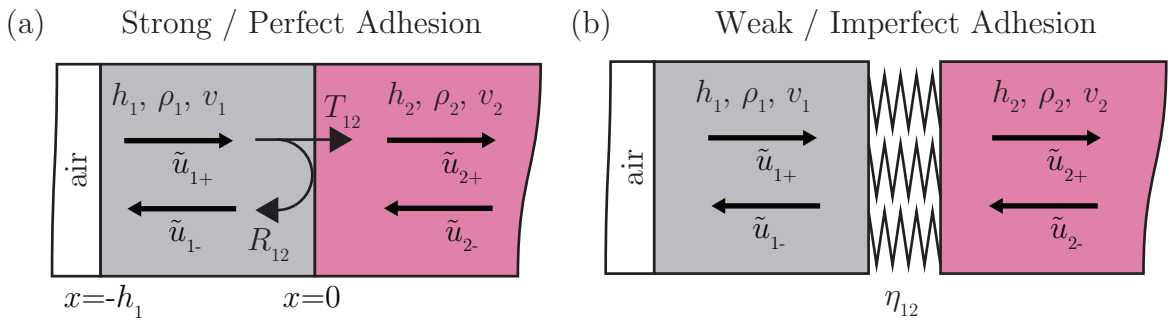

Figure 2.9.: Schematic of the structure used in the theory, including 3 layers (air, material 1 and half-infinite material 2) with the corresponding acoustic waves. Explicitly, the reflection and transmission at the interface between material 1 to material 2 is shown. (a) Two layers perfectly adhered to each other. (b) Two layers weakly adhered to each other by a massless spring.

The transmitted wave u_{2+} is dependent on the properties of the second layer:

$$u_{2+} = \tilde{u}_{2+} e^{i(k_2 x - \omega t)},$$

with k_2 the wave number in layer 2 and $\tilde{u}_{2+}$ the amplitude. Now, one can define the reflectivity and transmission coefficients at the interface, R_{12} and T_{12}:

$$u_{1-} = R_{12} u_{1+} \qquad\qquad u_{2+} = T_{12} u_{1+} \tag{2.20}$$

Together with the Eqs. (2.12) and (2.13) this yields the two equations:

$$u_{1+}(x=0) + u_{1-}(x=0) = u_{2+}(x=0) \tag{2.21}$$
$$\sigma_{1+}(x=0) + \sigma_{1-}(x=0) = \sigma_{2+}(x=0), \tag{2.22}$$

where Eq. (2.21) gives the simple relation: $1+R_{12} = T_{12}$. And Eq. (2.22) gives (with $\sigma = \rho v^2 \partial_x u$):

$$i\rho_1 v_1^2 k_1 (\tilde{u}_{1+} - \tilde{u}_{1-}) = i\rho_2 v_2^2 k_2 \tilde{u}_{2+} \tag{2.23}$$

Please note that the derivative of the displacement gives: $\partial_x u = ik_1 u$. Eq. (2.23) and Eq. (2.20), the definition of the impedance ($Z = \rho v$) and the linear acoustic dispersion $\omega = vk$ relation, result in:

$$Z_1(1 - R_{12}) = Z_2 T_{12}. \tag{2.24}$$

and solving for R_{12} by inserting T_{12} leads to the reflection coefficient:

$$R_{12} = \frac{Z_1 - Z_2}{Z_1 + Z_2}. \tag{2.25}$$

This reflection coefficient is derived for displacement waves. It looks slightly different for strain waves, which can be easily shown using Hooke's law and the linear dispersion relation. The

strain waves are

$$\sigma_{1+} = \rho_1 v_1^2 \partial_x u_{1+} = iZ_1 v_1 k_1 u_{1+} = iZ_1 \omega u_{1+}, \qquad \sigma_{1-} = .. = -iZ_1 \omega u_{1-}. \quad (2.26)$$

By inserting Eq. (2.20) one gets:

$$\sigma_{1-} = -R_{12}\sigma_{1+} \quad (2.27)$$

and, thus, for the reflection coefficient between the incoming and reflected strain waves the negative reflection coefficient of the displacement. The displacement will undergo a phase jump at reflection at a higher-impedance material. In contrast, the strain wave will undergo a phase jump at a lower-impedance material (for example at an air surface).
At last, the transmission coefficient can be derived by inserting (2.25) in (2.24):

$$T_{12} = \frac{2Z_1}{Z_2 + Z_1}. \quad (2.28)$$

2.5.2. Reflection and transmission coefficients at imperfect interfaces

For imperfect interfaces the boundary condition Eq. (2.12) does not hold anymore. Different models exist to describe and simulate adhesion, weak coupling and imperfect interfaces. Here, the displacement of both surfaces at the imperfect interface is assumed to be independent and only to be coupled by a spring. A sketch of a weakly adhered interface is shown in Fig. 2.9(b). Thus Eq. (2.14) replaces Eq. (2.12). One can use the same formalism and nomenclature for the acoustic waves: u_{1+}, u_{1-}, and u_{2+}. Also the reflection and transmission coefficients will be defined the same way. The boundary conditions lead to the set of equations:

$$\sigma_{1+}(x=0) + \sigma_{1-}(x=0) = \sigma_{2+}(x=0) = -\eta_{12}[u_{2+}(x=0) - [u_{1+}(x=0) + u_{1-}(x=0)]], \quad (2.29)$$

with the spring constant per unit area η_{12}. The left hand part yields the same result as above: $Z_1(1 - R_{12}) = Z_2 T_{12}$, while the right hand side gives:

$$i\omega Z_2 T_{12} = -\eta_{12}[T_{12} - 1 - R_{12}]. \quad (2.30)$$

Combining both equations yields:

$$i\omega Z_1(1 - R_{12}) = -\eta_{12}\left[\frac{Z_1}{Z_2}(1 - R_{12}) - 1 - R_{12}\right]. \quad (2.31)$$

Thus the reflection coefficient at imperfect interfaces is given by:

$$R_{12} = \frac{Z_1 - Z_2 + i\omega Z_1 Z_2/\eta_{12}}{Z_1 + Z_2 + i\omega Z_1 Z_2/\eta_{12}}. \quad (2.32)$$

An example of the reflection coefficient for displacement waves at the interface from Al to Si for different spring constants is shown in Fig. 2.10. For a simplifying of the units, the spring constant is scaled with the impedance of Si. A frequency dependent change of the reflection coefficient is seen. This is different from the reflection with perfect adhesion, where for every frequency the same reflection coefficient is present. For large spring constants, or more specifically good adhesion, the reflection coefficient becomes constant.

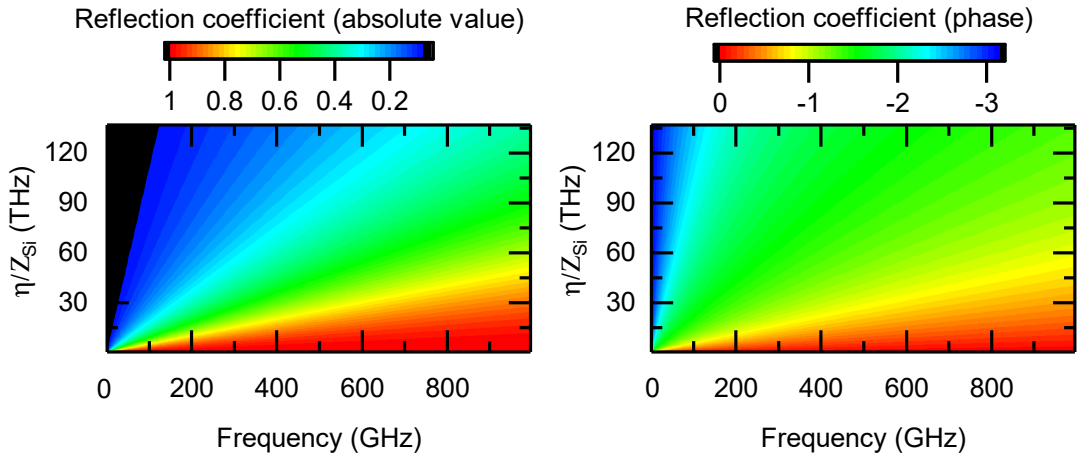

Figure 2.10.: (a) Absolute value and (b) phase of the reflection coefficient $R_{\mathrm{Al,Si}}$ at the interface between Al and Si in dependence of the spring constant η - scaled with the impedance of Si Z_{Si}. Black color indicates the values of perfect adhesion.

And for the transmission coefficient:

$$T_{12} = \frac{2Z_1}{Z_1 + Z_2 + i\omega Z_1 Z_2/\eta_{12}}. \tag{2.33}$$

2.5.3. Spectral transfer function

So far the cases of reflection and transmission of acoustic waves at individual perfect and imperfect interfaces were discussed. In the experiments conducted in this thesis, few nanometer thin films are used for advanced acoustic spectroscopy of the examined material. The wave propagation aspects of the interface and in the thin film cannot be distinguished easily. Therefore, the spectral transfer function is introduced which takes both contributions into account. For modeling this acoustic behavior the structure in Fig. 2.11 is considered. An acoustic wave incident from layer 2 on the thin film is assumed, where one part will be reflected at the interface and another part will be transmitted into the thin film. In the thin film the acoustic wave reverberates, leading to a different shape of the outgoing acoustic wave.
The incident mechanical displacement wave is u_{2-} and the outgoing wave is u_{2+}:

$$u_{2-} = \tilde{u}_{2-}e^{-ik_2x} \qquad u_{2+} = \tilde{u}_{2+}e^{ik_2x} \qquad u_{2+} = \Gamma u_{2-}, \tag{2.34}$$

where the ratio between both waves Γ is called the spectral transfer function. In layer 1 are the two counter-propagating waves:

$$u_{1\pm} = \tilde{u}_{1\pm}e^{\pm ik_1x}. \tag{2.35}$$

The air surface has to be stress free (see Eq. (2.11)), which gives the relation between the amplitudes of $\tilde{u}_{1+}$ and $\tilde{u}_{1-}$ and the surface:

$$\tilde{u}_{1-} = \tilde{u}_{1+}\exp(-2ik_1h_1) \tag{2.36}$$

Following Eqs. (2.13) and (2.14) the individual surface stresses have to be equal and have to be

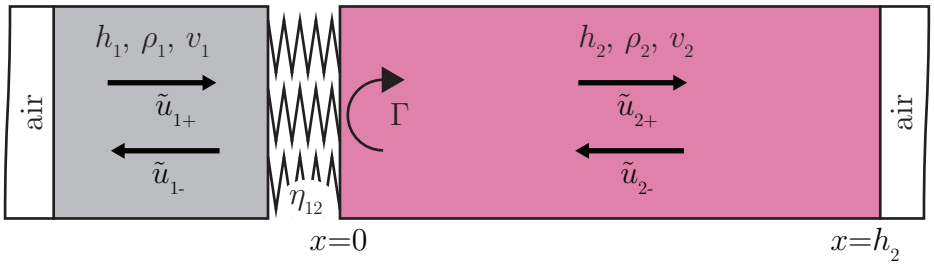

Figure 2.11.: Example of the theoretical structure, including 3 layers (air, material 1 and material 2) with the corresponding acoustic waves and a reflection at the interface from material 1 to material 2. The two layers are weakly adhered to each other by a massless spring.

equal to the stress of the spring ($[\sigma_1 = \sigma_2 = \sigma_{\text{spring}}]_{x=0}$):

$$\sigma_{1+} + \sigma_{1-} = \sigma_{2+} + \sigma_{2-} = -\eta_{12}[(u_{2+} + u_{2-}) - (u_{1+} + u_{1-})] \qquad \text{at position: } x = 0 \tag{2.37}$$

With the relation (2.36) and the definition of the spectral transfer function Γ this can be reduced to the following set of equations:

$$\sigma_1|_{x=0} = \quad i\omega Z_1(\tilde{u}_{1+} - \tilde{u}_{1-}) = i\omega Z_1 \tilde{u}_{1+}(1 - e^{-2ik_1h_1}) \tag{2.38}$$

$$\sigma_2|_{x=0} = \quad i\omega Z_2(\tilde{u}_{2+} - \tilde{u}_{2-}) = i\omega Z_2 \tilde{u}_{2-}(\Gamma - 1) \tag{2.39}$$

$$\sigma_{\text{spring}} = \quad -\eta_{12}[(\tilde{u}_{2+} + \tilde{u}_{2-}) - (\tilde{u}_{1+} + \tilde{u}_{1-})] = -\eta_{12}[\tilde{u}_i(\Gamma + 1) - \tilde{u}_{1+}(1 + e^{-2ik_1h_1})] \tag{2.40}$$

The combination of Eqs. (2.38) to (2.40) results in the spectral transfer function:

$$\Gamma = 1 - 2\left[1 + i\omega Z_2/\eta_{12} + \frac{Z_2}{Z_1}\frac{1 + e^{2ik_1h_1}}{1 - e^{2ik_1h_1}}\right]^{-1} \tag{2.41}$$

In Fig. 2.12 the phase of the spectral transfer function is plotted for a broad range of frequencies and different spring constants. One sees that for weak adhesion no phase shift occurs while for strong adhesion a periodic pattern emerges. For the case of weak adhesion, the first layer is nearly decoupled, which leads to a negligible phase shift. It should be noted, that the transition zone between full phase shift (perfect adhesion) and zero phase shift (decoupled layers) is limited only to values of the spring constant between two orders of magnitude. Additionally, with no attenuation in layer 1, the absolute value of the spectral transfer function is not spring-dependent and constant. By introducing attenuation this becomes more complicated (see Section 6.3).

By calculating the spectral transfer function with the use of the reflection and transmission coefficient (including all the reverberations via the geometrical series and assuming perfect reflection at the surface ($R_{air} = 1$)):

$$\Gamma = R_{21} + T_{21}e^{ik_1h_1}R_{air}e^{ik_1h_1}T_{12}\sum_{n=0}^{\infty}\left(R_{12}e^{ik_1h_1}R_{air}e^{ik_1h_1}\right)^n = R_{21} + \frac{T_{21}T_{12}}{\exp(-2ik_1h_1) - R_{12}} \tag{2.42}$$

the same result as in Eq. (2.41) is obtained.

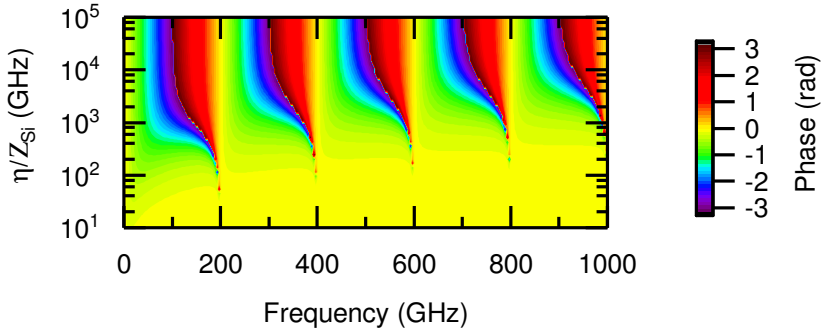

Figure 2.12.: Phase of the spectral transfer function Γ at the interface between Si and Al.

2.6. Resonance-induced mode quantization in bilayers

Here, the evolving and allowed modes in a separated two-layer system are discussed. The bilayer structure is shown in Fig. 2.11. At the air-surfaces perfect reflection is assumed and the reflection at the interface between layer 2 and 1 is given by the spectral transfer function Γ (defined in Eq. (2.41)). It describes the ratio between the acoustic wave $\tilde{u}_{2-}$ incident on the interface and the reflected acoustic wave $\tilde{u}_{2+}$ leaving the interface. It includes all reverberations in layer 1. The acoustic waves are defined as in Eq. (2.35). The definition of the spectral transfer function and the condition of the stress free surface at $x = h_2$ (2.36) lead to the two relations:

$$\tilde{u}_{2+} = \Gamma \tilde{u}_{2-}|_{x=0} \qquad \tilde{u}_{2+} = \exp(-2ik_2h_2)\tilde{u}_{2-}|_{x=h_2} \tag{2.43}$$

The combination of both gives the resonance condition of the two layer system:

$$\exp(-2ik_2h_2) = \Gamma = 1 - 2\left[1 + i\omega Z_2/\eta_{12} + \frac{Z_2}{Z_1}\frac{1+e^{2ik_1h_1}}{1-e^{2ik_1h_1}}\right]^{-1} \tag{2.44}$$

This can be rewritten with the propagation time for each layer $t_1 = h_1/v_1$ and $t_2 = h_2/v_2$:

$$\sin[\omega(t_1+t_2)] = \left[\left(1-\frac{Z_2}{Z_1}\right) + \frac{\frac{\omega Z_2}{\eta_{12}}\tan(\omega t_2)}{\frac{\omega Z_2}{\eta_{12}}\tan(\omega t_2) - 1}\right]\sin(\omega t_2)\cos(\omega t_1) \tag{2.45}$$

By solving for the frequency ω it is possible to extract the eigenmodes. One can approximate this equation to find an analytical solution. In first approximation both layers are assumed to be nearly identical concerning their impedances, i.e. $Z_1 \approx Z_2$, and the adhesion to be perfect ($\eta \to \infty$). This results in the vanishing of the terms in the brackets in the right hands side and, thus, the vanishing of the right hand side. This yields for the eigenmodes ω_n of a bilayer with perfect adhesion and identical impedances:

$$\sin[\omega(t_1+t_2)] = 0 \qquad \omega_n = \frac{n\pi}{(t_1+t_2)} = n\omega_0 \qquad (n = 1, 2, ...) \tag{2.46}$$

This result is straightforward as the assumption is the solution of a single layer with the combined thicknesses of both layers and the fundamental 1 layer mode ω_0. Furthermore, this result was

already obtained in the derivation of the standing Lamb waves (see Eq. (2.19)). However, Eq. 2.45 is not solved with the assumption of a linear frequency distribution of the eigenmodes in general.

One can assume, that for small acoustic mismatches between both layers, the solutions will not change too much. Therefore, to find the eigenmodes in the next step small perturbations $\Delta\omega << \omega_0$ are considered. This gives for the eigenmodes of the bilayer system: $\omega = \omega_n + \Delta\omega$. By inserting this ansatz in the eigenmode equation (2.45) the solution for $\Delta\omega$ can be found. The left hand side of the eigenmode equation (2.45) takes the form:

$$\sin[(\omega_n + \Delta\omega)(t_1 + t_2)] = \cos(\pi n)\sin(\pi\frac{\Delta\omega}{\omega_0}) \approx \pi\cos(\pi n)\frac{\Delta\omega}{\omega_0} \tag{2.47}$$

In the above derivation of the eigenmodes of the monolayer system, the right hand side was assumed to be zero. Now it is assumed to be small compared to the left hand side, hinting at a small influence of $\Delta\omega$ on the value of the right hand side. This allows for the Ansatz $\omega \approx \omega_n$, which simplifies the arguments of the trigonometric functions: $\omega t_2 \approx n\omega_0 t_2$ and $\omega t_1 \approx \pi n - n\omega_0 t_2$. Therefore $\cos(\omega t_1) \approx \cos(n\pi)\cos(n\omega_0 t_2)$. Substituting this relation and Eq. (2.47) in Eq. (2.45) yields for the frequency variation of the eigenmodes around the linear relationship ω_n:

$$\frac{\Delta\omega}{\omega_0} \approx \frac{\Delta f}{f_0} \approx \frac{1}{2\pi}\left[\left(1 - \frac{Z_2}{Z_1}\right) + \frac{\frac{n\omega_0 Z_2}{\eta_{12}}\tan(\frac{\pi}{1+t_2/t_1}n)}{\frac{n\omega_0 Z_2}{\eta_{12}}\tan(\frac{\pi}{1+t_2/t_1}n) - 1}\right] \times \sin\left(\frac{2\pi}{1+t_2/t_1}n\right) \tag{2.48}$$

For strong adhesion the frequency will be modulated sine-like, where the modulation period is given only by the ratio of each layers total propagation times. The amplitude of this oscillation is governed only by the ratio between the two impedances. To judge the quality of the approximation the numerical solutions of Eq. (2.45) are shown for different impedance ratios in Fig. 2.13(a) as well as the analytical approximation. Here, the second term on the right hand side was neglected, meaning perfect adhesion is assumed. For small modulations – impedance ratios equal to 1 ± 0.1 – the approximation yields the same results as the exact solution. For larger mismatches the sine-like modulation gets distorted until it resembles a saw-tooth like shape. But the period of the x-axis crossings stays the same. Also the amplitude of frequency modulations grows with growing impedance mismatch.

In Fig. 2.13(b) identical impedances between both layers are assumed while the adhesion is varied. The approximation and the exact solution are plotted for comparison. For good adhesion (large spring constant η) both solutions yield the same result, but for weak adhesion the agreement is worse than in the case of increased impedance mismatch. The exact modulation can be described by a $\propto -n\sin^2 ...n$ behavior with the doubled period of the sine argument, exactly the frequency with which the argument of the tangents oscillate. Please note, that the missing lines in the modulation for the weakest plotted adhesion are due to diverging solutions of the approximation.

One has to keep in mind that the visible deviations between exact and approximated solutions are expected due to the small angle approximation in Eq. 2.47: $\sin(\Delta\omega/\omega) \approx \Delta\omega/\omega$, which can not be valid anymore when the relative change is larger than 10 %. Furthermore, it is noteworthy that the crude representation, of the numerical solutions stems from the limited amount of data points because only at every full mode number a solution is derivable.

To conclude, a closed two layer system exhibits a modulation of the eigenmodes frequency

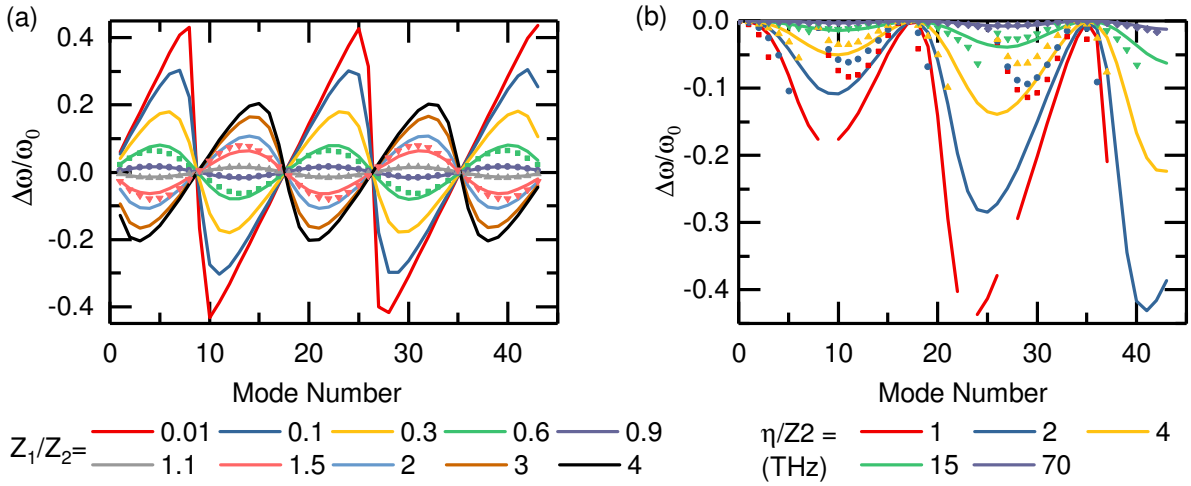

Figure 2.13.: The deviation of the eigenmodes of a two-layer structure from the eigenmodes of a single-layer structure with the identical acoustic length. (a) Eigenmode modulation due to an impedance mismatch. (b) Eigenmode modulation due to different adhesion between the two layers with identical impedance. The lines depict the numerical solutions of the exact eigenmode equation, while the symbols depict the analytical approximation. The lines are interrupted where no solution could be found. The propagation times $t_1 = 2.5\,\mathrm{ps}$ and $t_2 = 41.5\,\mathrm{ps}$ were chosen to resemble a two-layer system consisting of 15 nm Al on 350 nm Si.

compared to the equidistant mode spacing in a one layer system. This is true in general if reflection occurs at the interface between both layers, i.e. the reflection stems from an impedance mismatch or from a weakened adhesion between both layers. However, both processes exhibit a different change of the frequency modulation and are thus separable. The impedance mismatch leads to a modulation around the one layer eigenmode frequencies, while the adhesion induced modulation leads to comparably smaller frequencies than the one layer eigenmode frequencies.

2.7. Phonon dissipation mechanisms

2.7.1. Introduction

The temperature of a system can be defined by the internal kinetic energy. In a solid this does not mean particles moving from one position to another one, but the particles are fixed at their position. The positions are defined by the restoring forces given by the charges of the atomic lattice and the electron distribution. If one atom is moved out of its equilibrium position it will return back to that position with a non-zero velocity, leading to an oscillation around that point. The anharmonic interaction induced by that oscillation will act on the surrounding solid and the vibration will translate into a wave in the solid. This will weaken the original vibration. The internal vibrations of the atoms are a measure of the temperature in the solid. This can be described by the phonon picture, where the solids temperature corresponds to an incoherent phonon distribution, i.e. the Bose-Einstein distribution.
Dissipation means the transformation of a coherent phonons into incoherent phonons, i.e. into

the thermal equilibrium [Pei29, Mar71, Rei73, Imb14, Cep16]. In this section different possible dissipation mechanisms of phonons with the angular frequency ω will be explained. It is split in two parts, sorted by intrinsic and extrinsic processes. Intrinsic processes are present in a perfectly crystalline solid without any boundaries. Extrinsic processes include the residual effects given by the sample structure and quality. Finally, all processes are compared.

2.7.2. Intrinsic damping

Intrinsic damping means the absolute momentum change of a phonon due to scattering with present phonons or electrons. To undergo a change in momentum the process has to involve at least three scattering phonons. The phonons in the thermal bath are assumed to have the average lifetime τ_{th}. Then one can define the two regimes: the Akhieser regime $\omega\tau_{th} < 1$, where the damping stems from the viscosity of the thermal phonons gas, and the three-phonon-decay at $\omega\tau_{th} > 1$, where the phonon scatters with comparably high frequency phonons of the thermal system. Additionally, electron-phonon scattering will be discussed.

Akhieser-regime ($\omega\tau_{th} < 1$)

In the theory proposed by Akhieser [Akh39] the attenuation process is treated macroscopically [Mar71, Duq03]. The incident sound wave, more specifically the strain, will disturb the thermal phonons from equilibrium, as their frequencies depend upon the strain. Due to scattering among each other the thermal phonons tend to equilibrate, thereby irreversibly increasing the entropy in the system and attenuating the sound wave. The calculation is done using the Boltzmann equation method. A simplified expression of the Akhieser damping mechanism gives for the inverse damping time [Dal09]:

$$\tau_{Akhieser}^{-1} = \frac{C_V T}{\rho v_L^2} \frac{\omega^2 \tau_{th}}{1 + \omega^2 \tau_{th}^2} (\left\langle \gamma^2 \right\rangle - \langle \gamma \rangle^2), \tag{2.49}$$

with C_V the specific heat capacity at constant volume, T the temperature of the phonon bath, ρ the density, v_L the longitudinal speed of sound, τ_{th} the average thermal phonon relaxation time, γ the Grüneisen parameter of the thermal phonons, $\langle ... \rangle$ averages over the entire spectrum of the phonon bath (a value of 1 is assumed), and ω is the angular frequency of the considered phonon. This equation should hold, when thermoelastic damping is negligible.
The mechanism of thermoelastic damping was first developed by Zener. A spatial variation of strain is accompanied by a spatial variation of the temperature [De16]. This can be seen by looking at the thermal expansion coefficient, which can be expressed as variation of the strain with temperature: $\beta = \partial\varepsilon/\partial T$. Naturally heat will flow and try to equilibrate the thermal gradient. This leads to an increase in entropy and thus to dissipation. The lifetime τ_{TED} is given by [Zen38, Tru69]

$$\tau_{TED}^{-1} = \frac{\beta^2 E T}{C_V} \frac{\omega^2 \tau_d}{1 + \omega^2 \tau_d^2} \tag{2.50}$$

with E the Young's modulus, T the mean temperature of the phonon bath, C_V the specific heat capacity at constant volume, and τ_d the thermal diffusion time. The thermal diffusion time across a gradient of the temperature with the length d is $\tau_d = d^2 C_V/\kappa$, with the thermal conductivity κ. Thermoelastic damping occurs, if the strain field is spatially inhomogeneous and the wavelength

of the respective phonon is large enough to allow for heat flow between the different strains. While the formulas of thermoelastic damping and Akhieser damping look similar, the time scale is different and the prefactor has different magnitudes. Daly et al. assumed the thermoelastic damping contribution compared to the Akhieser damping to be 10 % at 50 GHz and 30 % at 100 GHz [Dal09]. However, in Si membranes the strain field is very inhomogeneous during the strain front's propagation, switching between the maximum value and zero. Therefore, a distinct influence will be present with a thermal diffusion length of the magnitude of the membrane size, leading to an important contribution of the thermoelastic damping.
For the damping processes the following values are assumed for Si: $\tau_{th} \approx 17\,\mathrm{ps}$, $\beta = 23{\cdot}10^{-6}\,\mathrm{K}^{-1}$, $E = 179\,\mathrm{GPa}$, $T = 300\,\mathrm{K}$, $C_V = 1.6\,\mathrm{J\,cm^{-3}K^{-1}}$, $d = 80\,\mathrm{nm}$ (given by roughly a quarter of the assumed membrane's thickness), and $\kappa = 140\,\mathrm{W\,K^{-1}m^{-1}}$.

Three-phonon-scattering ($\omega\tau_{th} > 1$)

In the theory proposed by Landau and Rumer [Lan37] the attenuation is derived microscopically from scattering of the phonons of the sound wave with thermal phonons. Due to energy conservation this is at least a three phonon process. The thermal phonons have high frequencies, compared to the incoming sound wave. Therefore, one can assume that a sound wave phonon will scatter together with a thermal phonon to generate a new thermal phonon with a slightly different frequency. Both, Normal- and Umklapp-processes can happen. The theory was advanced by Herring [Her54], who found that the scattering of a longitudinal acoustic phonon with a transverse thermal phonon to generate a new thermal phonon with higher energy is most important. Simons found for the behavior of the lifetime in dependence of the crystal symmetry [Sim57]:

$$\tau_H^{-1} = E_H(T)\omega^a(k_BT/\hbar)^{(5-a)} = B_H(T)\left(\frac{\omega}{v}\right)^2, \tag{2.51}$$

where k_B is the Boltzmann constant, T the temperature, $\hbar$ the Planck constant, v the speed of sound, and $a = 2$ for cubic crystals, especially Si. This formula is derived under the approximation that during the scattering of the phonons the thermal phonon bath does not change. The coefficient $E_H(T)$ can be calculated analytically for temperatures far below the Debye temperature and is proportional to T^{-3} [Mar11]. The calculation for room temperature is more complicated as a microscopic model is necessary. Ward and Broido found $B_H(T = 300\,\mathrm{K}) = 6.3 \times 10^{-6}\,\mathrm{cm^2\,s^{-1}}$ for Si averaged over all directions [War10].
To account for higher temperatures and assuming additional scattering processes for pure longitudinal modes with a small wave vector compared to the thermal phonon bath, Cuffe et al. evaluated only Normal three-phonon-processes ($L + L_1 \to L_2, L + T_1 \to L_2, L \to L_1 + L_2, L \to T_1 + T_2, L \to L_1 + T_2, L \to T_1 + L_2$): [Sri76]:

$$\tau_{3-ph}^{-1} = \frac{\hbar v_\mathrm{L}}{4\pi\rho v_\mathrm{G}^2}\gamma^2 \sum_{P1,P2} \frac{1}{v_{P1}^2 v_{P2}^2} \int \omega_{P1}(\omega + \omega_{P1})^2 \frac{n(\omega_{P1})[n(\omega_{P2}) + 1]}{n(\omega) + 1} d\omega', \tag{2.52}$$

where $P = L, T$ is the polarization, n is the Bose-Einstein-distribution function, v_G the phonon average group velocity and γ is the mode-averaged Grüneisen parameter. Omar et al. found the value of $\gamma = 1.08$ to give the best fit to the thermal conductivity data of Si nanowires [Oma10]. Cuffe et al. found for this formula a dependence $\propto \omega^{-1}$ above 20 GHz and concluded that the

highest contribution to the intrinsic lifetimes stems from the $L \to L_1 + L_2$ process [Cuf13].

Electron-phonon scattering

While the above considerations hold for all crystals, especially in metals there will be an additional contribution due to free electrons. Pippard assumed an acoustic plane wave incident on a block of metal, where the acoustic wave introduces a charged electron density in the metal [Pip55]. As the electrons follow the strain motion very fast, this leads to small electric fields. The electric field is acting on the atoms and the inertia of masses lead to incoherent collisions. The lifetime of the energy dissipation is calculated to be:

$$\tau_{e-ph}^{-1} = \frac{N m v_\mathrm{F}}{3\rho v_\mathrm{L} d} \left(\frac{(\omega d/v_L)^2 \arctan(\omega d/v_L)}{\omega d/v_L - \arctan(\omega d/v_L)} - 3 \right), \tag{2.53}$$

with N the free electrons per unit volume, ρ the density, m the effective electron mass, d the electronic mean free path and v_F the Fermi velocity. The electron mean free path in Al can be calculated by the free electron model of a Fermi-sphere to be $d = 18.9\,\mathrm{nm}$. For large frequencies the lifetime becomes proportional to ω^{-1}. The other parameters are: $v_\mathrm{F} = 2.03 \cdot 10^6\,\mathrm{m/s}$, $N = 5 \cdot 10^{28}\,\mathrm{m}^{-3}$, $\rho = 2700\,\mathrm{Kg\,m}^{-3}$, $m = 9.1 \cdot 10^{-31}\,\mathrm{Kg}$.

2.7.3. Extrinsic damping

In this section dissipation beyond intrinsic damping will be discussed. This occurs if the investigated material is not perfectly crystalline, the surfaces are not smooth or the material is not isotopically clean.

Surface scattering

Two types of waves which are influenced by a rough surface are discussed: Perpendicular and parallel incidence. The root-mean-square roughness of the surface is denoted with δ having typical values around 1 nm.

Perpendicular incidence

A phonon incident on a roughened surface is assumed to be reflected perpendicular. Depending on the lateral position, microscopically, the phonon will gain or loose phase compared to a phonon reflected at a smooth surface. This phase change depends on the wavelength of the phonon and is given by: $\phi(\lambda, x, y) = 4\pi\hat{\delta}(x, y)/\lambda$, where $\hat{\delta}(x, y)$ is the spatial variation of the surface height. The superposition of all distinct phonon paths will give the amplitude decay of the acoustic wave. The now discussed theoretical model introduces the phenomenological parameter p – the specularity, which is 1 for a perfectly smooth surface and 0 for a perfectly rough surface. The auto-correlation of the phase gives the specularity parameter $p = \exp(-16\pi^3\delta^2/\lambda^2)$ [Zim60, Cuf13]. By introducing a second surface at the distance d, in between which the phonons can be reflected multiple times, one can define a phonon mean free path:

$$\Lambda = v_\mathrm{L}\tau = \frac{1+p}{1-p} d \tag{2.54}$$

This gives for the lifetime of a longitudinal acoustic phonon with the frequency ω:

$$\tau_\delta(\omega) = \frac{d}{v_\mathrm{L}} \coth\left(\frac{2\pi\delta^2}{v_\mathrm{L}^2}\omega^2\right) \approx \frac{d v_\mathrm{L}}{2\pi\delta^2\omega^2} \tag{2.55}$$

The effective lifetime should be smaller, as this approach only takes into account the phase change from reflection but neglects momentum/angle scattering. A typical membrane thickness is 300 nm.

Propagation parallel to the surface

If a surface wave, especially a Rayleigh wave, propagates along the rough surface it will undergo scattering into the bulk. Maradudin et al. calculated the scattering rate. For small frequencies the surface scattering resembles the scattering from a point mass defect. Here, the main contribution to the scattering is the scattering into other Rayleigh waves. [Ste70, Mar76, Gel16]:

$$\tau_{saw}^{-1} \approx \begin{cases} \frac{\delta^2 a^2}{v_\mathrm{R}^4 \pi}\omega^5 & a\omega << v_\mathrm{R} \\ \frac{\delta^2 a}{v_\mathrm{R}^3 \pi}\omega^4 & a\omega >> v_\mathrm{R} \end{cases}, \tag{2.56}$$

where a is the roughness correlation length and v_R the Rayleigh velocity. The Rayleigh velocity in Si is $v_\mathrm{R} \approx 5000\,\mathrm{m/s}$. This yields for the roughness correlation length with a frequency of 100 GHz, $a \approx v_\mathrm{R}/\omega \approx 8\,\mathrm{nm}$.

Isotope scattering

Discontinuities in a crystal will lead to scattering of phonons at those discontinuities. That can be defects, or even isotopes. The lifetime can be described by a simple formula, if the phonon wavelength is large compared to the lattice parameter [Mar11]:

$$\tau_{iso}^{-1} = \frac{V}{8\pi v_L^3}\left(\sum_i f_i \frac{(m_i - m)^2}{m^2}\right)\omega^4 = B_{iso}\omega^4, \tag{2.57}$$

with V the volume per atom, the average mass m, the mass m_i of the isotope i, and the fraction f_i of that isotope. For Si in [100]-direction the coefficient is found to be $B_{iso} = 8.1 \times 10^{-19}\,\mathrm{ns}^3$ [Tam83].

Mass-loading induced radiation of SAWs

As is calculated in Section 2.4 for Lamb Waves, the propagation is assumed to be loss free. As the boundary conditions are continuous, the surfaces are stress free, and only perfect reflection occurs at the surfaces with transverse modes generating longitudinal modes and vice versa. If the surface is disturbed by something on top like a metal grating, the boundary condition of a stress free surface is not given anymore. The rate of radiation per unit area for a comparably thin grating (meaning the displacement in the grating is constant) is calculated to be [Lin93, Sad10, Gel16]:

$$\frac{dE}{dt} = \frac{\rho_g^2 d^2 \omega_0^4 U_0 (1 - cos(2\pi\gamma))^2}{8\pi^2 v_\mathrm{L}\rho_s}, \tag{2.58}$$

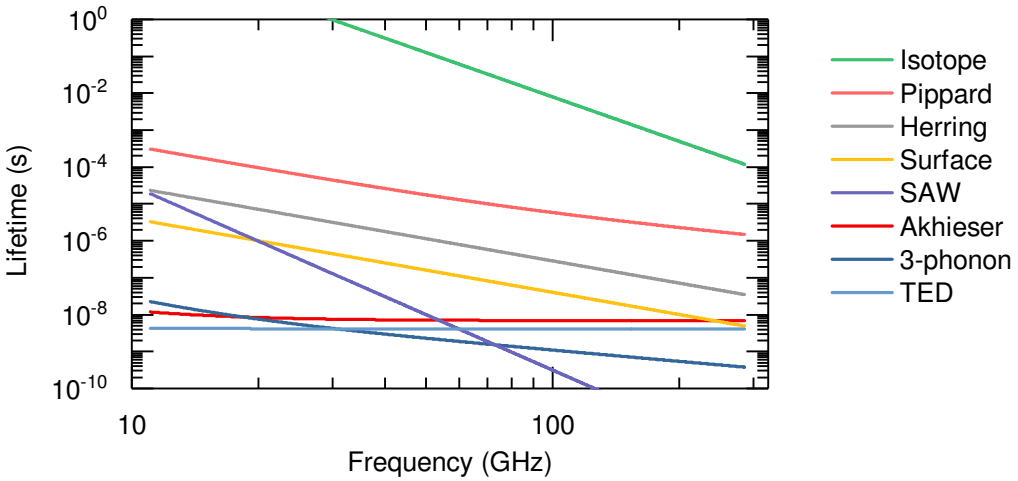

Figure 2.14.: Theoretical lifetimes of the individual dissipation processes discussed in the text. The parameters are taken for typical values of 300 nm Si membranes and Al at room temperature.

with the densities of the grating ρ_g and the substrate ρ_s the thickness of the grating d, the frequency ω_0 of the ground mode, the maximum displacement of the ground mode in z-direction U_0, and the filling fraction γ. The maximum damping is achieved if the ratio of covered to uncovered substrate is 50 %.

2.7.4. Comparison of the different regimes

The frequency dependent lifetimes for all above processes are shown in Fig. 2.14. For all attenuation processes the material Si was assumed, whereas for the metallic damping (electron-phonon scattering = Pippard) Al was assumed. The weakest influence on the lifetime has the isotope scattering process. However, the strongest influence on the lifetimes in the lower GHz frequency regime is given by the Akhieser process, thermoelastic damping, and 3-phonon decay. Here, it should be noted, that only crude values were taken for the calculation and quantitative shifts are easily obtained by assuming a different thermal relaxation time, or thermal diffusion lengths. Therefore, measurements are needed to quantify the different contributions and intensities. In the Appendix literature values of, theoretical predictions for, and selected data obtained in this thesis of acoustic lifetimes in Si are compared.

2.7.5. Implementation of dissipation

In the above section, it is shown that the spectral transfer function leads to a phase shift in the spectrum. But it will become clear later that – due to the spring model – there is also the possibility that distinct frequencies disappear in the spectrum. However, this is only possible by including attenuation processes. This can either be done by introducing a complex elastic modulus or a complex spring. To include intrinsic damping the elastic modulus C becomes complex. Using Eq. (2.9) leads to a complex speed of sound $v = \sqrt{C/\rho}$ and, therefore, also to a complex impedance. Utilizing the dispersion relation $\omega = vk (= k' + ik'')$ this leads to a complex

wavevector. From the theory one can calculate the frequency dependent lifetime τ. This can be included in the imaginary part of the wave vector. The imaginary part of the wave vector leads to the exponential decay factor of the acoustic wave with the thickness: $e^{-k''h}$. If one assumes $h = v'\tau$ to be the value where the wave is dampened about $1/e$, then $k''v'\tau = 1$ and the imaginary part of the wave vector is

$$k''(\tau) = 1/(v'\tau). \tag{2.59}$$

2.8. Numerical solution of the wave equation – FDTD

Not all problems can be solved analytically. To obtain a deeper understanding of some systems and measurements, a finite difference time domain algorithm is implemented to solve the acoustic wave equation.

It is useful to introduce the velocity of the displacement $v = du/dt$. Together with the definition of the differential stress in Eq. (2.7), this gives the continuum mechanics formulation of Newton's law:

$$\rho\frac{\partial v}{\partial t} = \frac{\partial \sigma}{\partial x} \tag{2.60}$$

and Hooke's law Eq. (2.6)

$$\frac{\partial \sigma}{\partial t} = C\frac{\partial v}{\partial x} + \frac{\partial \sigma_{\text{source}}}{\partial t} \tag{2.61}$$

For the numerical implementation the derivatives have to be discretized and the dependencies have to be separated. Here, the splitting of the inhomogeneous wave equation into one equation for the velocity and one for the stress is useful. The derivation will be implemented in the following way:

$$\frac{d\sigma, v}{dx}|_{x=x_0} \approx \frac{\sigma, v(x_0 + \Delta x) - \sigma, v(x_0 - \Delta x)}{2\Delta x} \tag{2.62}$$

One grid is implemented for the velocity and one for the stress. The velocity of the defined grid particles is assumed to be in between the defined particles as depicted in Fig. 2.15. For the numerical calculation the time steps are shifted between the stress and velocity grids. This allows to implement the boundary conditions in a very convenient way, which will become clearer below. In the following notation one time step will be $2\Delta t$ and one spatial step will be $2\Delta x$.

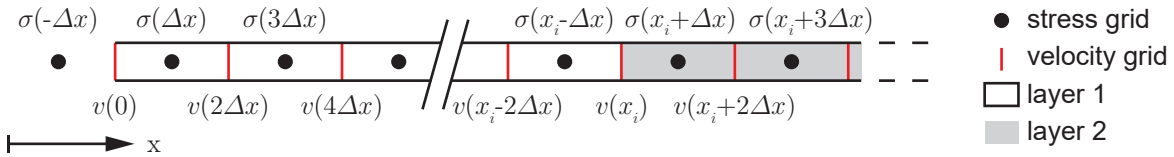

Figure 2.15.: Schematic for the numerical implementation of the spatial discretization of the velocity and stress. The velocity grid points are marked with a red bar and the stress grid with filled circles. The boundary condition at the surface is realized by introducing a mirror stress point outside. Correspondingly, an interface between two layers is assumed to be at a velocity grid point between two stress grid points.

This leads to the discretized inhomogeneous wave equation split up in the velocity:

$$v(t+2\Delta t,x) = v(t,x) + \frac{\Delta t}{\rho \Delta x}[\sigma(x+\Delta x) - \sigma(x-\Delta x)]_{t+\Delta t} \tag{2.63}$$

and the stress:

$$\sigma(t+\Delta t, x-\Delta x) = \sigma(t-\Delta t, x-\Delta x) + C\frac{\Delta t}{\Delta x}[v(x) - v(x-2\Delta x)]_t + [\sigma_\mathrm{s}(t+\Delta t) - \sigma_\mathrm{s}(t-\Delta t)]_{x-\Delta x} \tag{2.64}$$

In addition to discretizing the wave equation it is also necessary to adjust the boundary conditions (see Section 2.3). The stress free surface is realized by assuming the surface at the first point of the velocity grid. This include a virtual stress mirror point outside the system with the identical negative stress, which leads to the condition: $\sigma(t,\Delta x) = -\sigma(t,-\Delta x)$. Thus, at the surface the stress is zero.
At an interface the procedure is similar: the interface is placed at the spatial point i of the velocity grid. The velocities in both layers will be different, which leads to a different spatial grid at the different layers. Therefore one has to adjust Eq. (2.63) with the arithmetic average of the density and the differentiation as $\partial_x \sigma \approx 2\partial\sigma/(\Delta x_1 + \Delta x_2)$. This changes Eq. (2.63) to:

$$v(t+2\Delta t, x_i) = v(t,x_i) + \frac{2}{Z_1+Z_2}[\sigma(x_i+\Delta x) - \sigma(x_i-\Delta x)]_{t+\Delta t}, \tag{2.65}$$

where Z_1 and Z_2 are the impedances of the two adjacent layers. This approach gives good results for rigid interfaces.
If the interface is not rigid and both layers are weakly adhered one can describe the boundary by a spring (see Sec. 2.3). One can discretize Eq. (2.14) to:

$$v(t+2\Delta t, x_i) = v(t,x_i) + \frac{1}{\eta_{12}\Delta t}[\sigma(x_i+\Delta x) - \sigma(x_i-\Delta x)]_{t+\Delta t}, \tag{2.66}$$

with η_{12} being the spring constant between layer 1 and 2.
To compute the temporal solution of the numerical solution at least two time steps of the external stress field have to be introduced and the whole spatial grid has to be predefined. For one layer, one should use the "magic" time step and define $\Delta t = \Delta x / v_\mathrm{L}$. This gives the exact same result for the finite-difference-time-domain solution as the analytical solution. It also prevents numerical artifacts and dispersion. The step size for Δx has to be smaller than $v_\mathrm{L}/10 f_\mathrm{max}$, where f_max is the highest calculated phonon frequency. For two layers with a different speed of sound and, thus, a different spatial grid this perfect behavior vanishes. The choice of the time step is, therefore, crucial for a good numerical simulation.

2.9. Conclusion

In this chapter the continuum's theory for mechanics in solids was introduced. This includes the propagation properties of longitudinal and transverse waves in isotropic media. The effect of interfaces is introduced on the examples of a half-infinite medium, thin plates, and the bonding of two layers. Guided modes in a thin plated are discussed in detail for the case of Lamb waves. The eigenmodes of a two-layer system with different acoustic impedances were calculated and a modulation around a linear relation is predicted. Depending on the physical mechanism of the transmission and reflection at the interface, which can be induced by impedance-mismatch or a weak adhesion between both layers simulated by a spring model, the eigenmodes modulation exhibit a different shape. Assuming one of those layers to by quite thin compared to the other, the spectral transfer function at reflection at this thin layer including reverberations in the thin layer is calculated. For different acoustic pulses the spectrum's change is described in the next chapter. Following the frequency dependent description of interface propagation, frequency dependent dissipation mechanisms were introduced and discussed. Both intrinsic and extrinsic processes play in important role in phonon attenuation. At last, a numerical method for solving the wave equation is described, which yields good results for simple systems. But to forecast the measured data a detailed analysis of the generation and detection mechanisms is necessary, which is given in the next chapter.

Chapter 3

Light matter interaction

3.1. Introduction

The experimental work in this thesis is mostly carried out by optically exciting a sample with a laser pulse. This excitation leads to an impulsive stress in the system. The subsequent measurement of the temporal evolution of the propagating stress is dependent on the opto-elastic properties.
In this chapter the basic mechanisms of generation, propagation, and detection of coherent acoustic phonons (CAP) are introduced. First, the optical excitation processes in metals and semiconductors and the main mechanisms of stress generation will be discussed. Thereafter, the distinct spectrum of the generated CAP is discussed, depending on the optical properties of the material, i.e. the absorption depth and interfaces. The propagation characteristics are discussed in the following. Different detection processes are introduced. In the end of the chapter the detected spectrum and the expected time resolved signal is derived.

3.2. Excitation processes in metals and semiconductors

In the simplest scheme one expects to generate heat in the sample by shining light on it. But heat is mostly incoherent as the excited states do not exhibit a distinct phase relation. This would allow to detect heat flow only, where the time scale is dependent on the diffusion of the heat. By employing ultrashort light pulses a new class of experiments has become feasible: One is able to examine certain distinct frequencies of the phonon spectrum due to the possibility of exciting coherent phonons, which have a well-defined phase relation to the optical pump pulse. After the introduction of the subsequent physical processes the generation processes of the dynamics of incoherent phonons are considered.
Excitation of metals: A thermally equilibrated metal exhibits the same temperature for the phononic system as for the electronic system (T_0). In the electronic system the states are filled up to the Fermi energy E_F, where the edge is broadened due to the temperature in the system with the width $k_\mathrm{B}T$, with k_B the Boltzmann constant and T the temperature, respectively. When an optical pump pulse with the frequency ν hits the metal within the optical absorption depth ξ, electrons below the Fermi level will be raised above the Fermi level [Tas94]. In Fig. 3.1(a) the subsequent strong nonequilibrium electron distribution is shown, where no temperature of the electronic system can be defined. The electrons have ballistic velocities around 10^6 m/s [Hoh00]. In the next 10-300 fs the electrons thermalize due to electron-electron scattering [Sun94, Ret02].

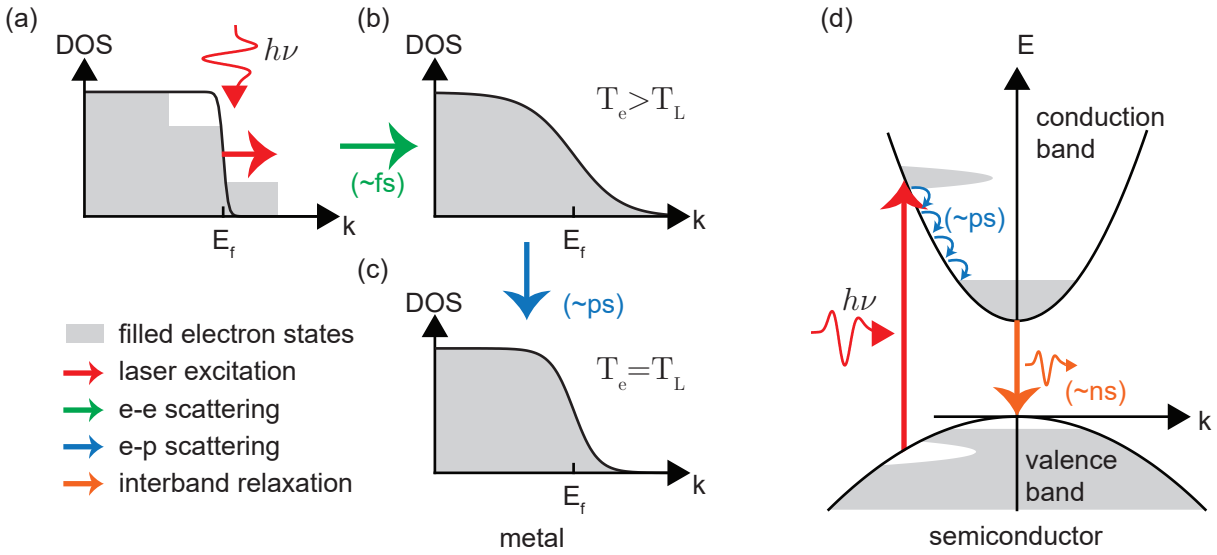

Figure 3.1.: Three different states of the electronic system in a metal due to intraband excitation and the electronic system in a semiconductor due to interband excitation. (a) The optical pump pulse creates a non-thermal distribution of the electrons, which spreads with ballistic velocities. (b) On a below-picoseconds time scale the hot electrons relax by collision with electrons to a diffusive energy transport regime. A Fermi distribution with the temperature T_e is established. (c) On the time scale of a few picoseconds the electronic system couples to the lattice via electron-phonon coupling and both systems balance to an increased temperature compared to the non perturbed system ($T_e = T_L$). (d) In a semiconductor the optical pump pulse excites electrons above the band gap into the conduction band and creates holes in the valence band. The charge carriers relax in picoseconds to the respective band edges while generating incoherent acoustic and optical phonons, where they recombine on a nanosecond scale. The figures are reproduced and adapted from [Hoh00] and [Rue15].

After thermalization of the electron system a temperature can be defined for the electron system $T_e >> T_L \geq T_0$, which is above the initial temperature and the lattice temperature T_L (see Fig. 3.1(b)). The electrons have diffusive velocities around 10^4 m/s. In the next few picoseconds the electrons thermalize with the lattice due to the excitation of incoherent phonons due to electron-phonon coupling (see Fig. 3.1(c)) [Val07]. The velocity of the electrons diminishes to 10^2 m/s. A new temperature distribution establishes with $T_e = T_L > T_0$. The electron-phonon coupling g is dependent on the metal. For gold (cobalt, aluminum) it yields: $g = 2(31, 93) \cdot 10^{16}\,\mathrm{W\,s^{-1}\,m^{-3}}$ [Hoh00, Ret02]. This is of similar magnitude as the values of Hostetler et al., who prepared thin Al films on different substrates by thermal evaporation and obtained for the substrates glass (Si, SiO_2, bulk): $g_{Al} = 22(20, 23, 24) \cdot 10^{16}\,\mathrm{W\,s^{-1}\,m^{-3}}$ [Hos99].

Excitation of semiconductors: An optical pump pulse excites electron-hole pairs in a semiconductor when its energy $h\nu$ is above the band gap energy E_g. The excited electron distribution is non-thermal and the electrons relax in the next 100-300 fs due to electron-electron scattering to a thermal distribution [Jeo99]. The electrons and holes relax on the timescale of a few picoseconds via electron-phonon coupling to the respective band edges [Dem11]. Due to the arbitrary

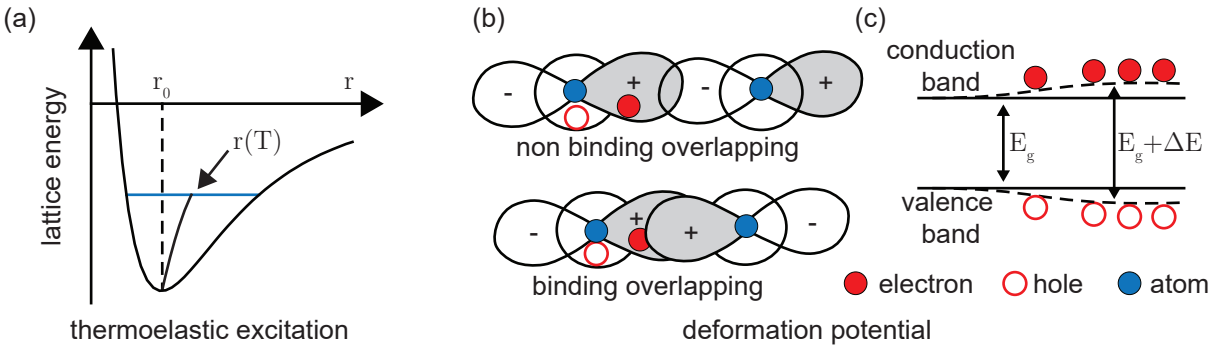

Figure 3.2.: Stress generation processes in a solid by thermoelasticity and deformation potential. (a) An increased lattice temperature leads in an anharmonic potential to an extension of the mean interatomic distance $r(T)$. (b) In the microscopic description the excited electron leads to a binding, or non-binding orbital (the sign of the electronic wave function is depicted in white or gray). This leads to either a compression or an expansion of the interatomic distances. (c) In the band structure description the excited electron-hole pairs lead to a change of the electronic distribution in the system. The band structure follows this modification (dashed lines) and forces the interatomic distances to change. The figures are reproduced and adapted from [Rue15].

scattering incidents there is no phase correlation between the generated optical and acoustic phonons. In comparison to the metal, in the semiconductor only negligible electron-electron scattering occurs as most of the possible scattering states are forbidden and the electron densities are much lower. Depending on the band structure and the doping level the recombination times of the electron-hole pairs can vary between a few ps (low-temperature grown GaAs with many defects) and hundreds of ns (very pure semiconductor crystals).

3.3. Stress generation processes

Following the explanation of the incoherent phonon generation processes, next the major stress generation processes will be discussed. The focus will be on thermoelasticity and deformation potential. These stress generation processes lead to coherent acoustic phonons, as they have a fixed relationship to the pump pulse. Additional stress generation processes, which will not be discussed here are for example: magnetostriction [Kor08], electrostriction [Rue15], and an inverse piezoelectric process [Rue15].

Thermoelasticity: The excitation due to the pump pulse increases the incoherent phonon population. In other words the lattice temperature is raised. In Fig. 3.2(a) a Lennard-Jones potential is shown as an approximation for an atomic potential with the distance r_0 between the atoms at $T = 0\,\mathrm{K}$. A temperature increase will lead to a higher state in the potential. Due to its anharmonicity the interatomic distance $r(T)$ will enlarge. This extension is a direct consequence of the temperature rise ΔT due to the incoherent phonons and is now in phase with the pump pulse. This leads to the stress [Tho86]:

$$\sigma_{\mathrm{TE}}(x,t) = -3C\beta\Delta T(x,t) \tag{3.1}$$

with C the bulk modulus and β the linear expansion coefficient. One can approximate the temperature change in a substrate due to excitation with a laser pulse to be [Tho86]:

$$\Delta T = \frac{(1-R)Q\alpha}{AC_V}\exp(-\alpha x) \tag{3.2}$$

with the optical reflection R, the energy per pulse Q, the absorption coefficient α, the spot area A, and the specific heat per unit volume C_V. Because the absorption coefficient in metals is in general larger than in semiconductors, it follows directly from this formula that in general the thermoelastic stress generation in metals will be larger than in semiconductors.

Deformation potential: For the deformation potential it is not necessary to generate heat, but to influence the electronic wave functions in the material. This can be understood in the microscopic (molecular binding) and the macroscopic (band structure) picture. In Fig. 3.2(b) two atoms with overlapping wave functions are shown. Due to the excitation an electron is lifted to a higher orbital, which is overlapping with an orbital of the neighboring atom. Depending on the sign of the wave function this can lead to a binding or a non-binding orbital between both atoms, whereas the binding overlap would lead to a compression and the non binding overlap would lead to an expansion. The induced stress is described by [Rue15]

$$\sigma_{\mathrm{DP}} = \sum_{\vec{k}} \delta n_e(\vec{k}) \frac{\partial E_{\vec{k}}}{\partial \eta} \tag{3.3}$$

with the change in the number of electrons $\delta n_e(\vec{k})$ with the wave vector $\vec{k}$ and the derivative of the band gap energy $E_{\vec{k}}$ with respect to changes in the strain η.

In Fig. 3.2(c) the band structure in one dimension and excited electron-hole pairs are shown. Due to the presence of the electron-hole pairs the band structure will be deformed, leading to a new electron configuration. The atoms follow the distribution of electrons, which forces the interatomic distances to change. The stress induced by the deformation potential in a semiconductor can therefore be described by the change of the band gap energy [Tho86, Yu10]:

$$\sigma_{\mathrm{DP}}(x,t) = N_e(x,t)\frac{\partial E_g}{\partial \eta} = -CN_e(x,t)\frac{\partial E_g}{\partial P} \tag{3.4}$$

with the total number of photoexcited electrons $N_e(x,t)$, the band gap energy E_g and the electron pressure P. The deformation potential can be negative or positive, depending on the material and the position in the band structure [Wri95, Sab02]. In Si $\frac{\partial E_g}{\partial P}$ is negative, which leads to a compressive stress upon illumination [Gau67].

For low plasma densities the number of photoexcited electrons is given by:

$$N_e(x) = \frac{(1-R)Q\alpha}{A(h\nu - E_g)}\exp(-\alpha x) \tag{3.5}$$

where the excitation light has the energy $h\nu$. With Eq. (3.2) and (3.5) one finds for the comparison of the contribution of the thermoelastic and deformation potential stress in Si:

$$\frac{\sigma_{\mathrm{DP}}}{\sigma_{\mathrm{TE}}} \approx \frac{\partial E_g}{\partial P}\frac{C_V}{3\beta(h\nu - E_g)} \approx -7. \tag{3.6}$$

In Si for light with the wavelength of 800 nm the compressive stress by deformation potential ($\frac{\partial E_g}{\partial P} = -2.3 \times 10^{-24}\,\mathrm{cm}^3$ [Wri95]) is seven times larger than the tensile thermoelastic stress. Upon excitation with 800 nm light therefore Si will contract.

3.4. Generation of coherent acoustic phonons

In the following the generated spectra for a purely longitudinal acoustic wave with i) a very short excitation length, compared to the layer thickness d, and ii) a homogeneous excitation of the layer are discussed. These are for example the case for i) a thick metal film with a short optical absorption length ξ and ii) a Si membrane with an absorption length at the used wavelength larger than the membrane thickness. For the metal purely thermoelastic excitation is assumed, while for the Si membrane stress is purely by deformation potential assumed. The lateral excitation will not be discussed in detail, as the area of the pump spot is much larger than the absorption length. Therefore, the description is restricted to a one dimensional approach with the distance x from the surface. By inserting one of the above discussed stress generation processes σ_{source} in Eq. (2.10) the wave equation can be solved.

i) $\xi << d$: This assumes an exponential absorption in the metal only and neglects electron diffusion and additional processes. Furthermore, the pump pulse shall be shorter than the elastic time scales of the system. The deposited energy by the pump pulse in a unit volume can be described as [Tho86]:

$$W(x) \approx (1-R)\frac{Q}{A\xi}e^{-x/\xi}, \tag{3.7}$$

with R the optical reflectivity of the film, Q the pulse energy, and A the pump spot size. In this

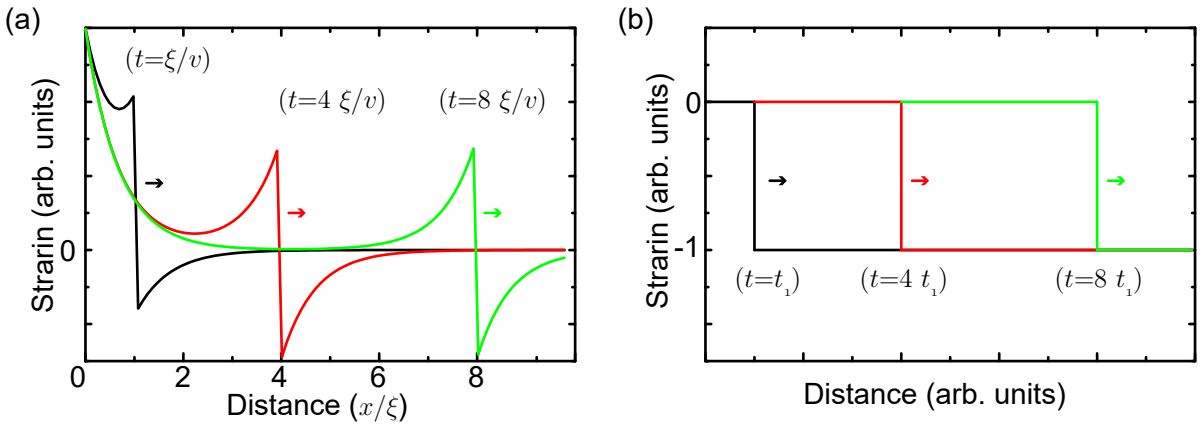

Figure 3.3.: (a) Strain in a metal layer after excitation and heating with a short laser pulse. The strain pulse propagates into the layer. The pulse width corresponds to the excitation depth ξ. No heat diffusion is assumed, which leads to the static stress at the surface. (b) Strain in a homogeneously excited layer. The strain pulse at the surface propagates into the layer.

simplified system an exponential temperature gradient is established:

$$\Delta T(x) = \frac{W(x)}{\rho C_{\mathrm{V}}} \propto e^{-x/\xi}, \tag{3.8}$$

with the density ρ and the specific heat capacity C_{P}. By assuming the thermoelastic stress generation process (Eq. (3.1)) $\sigma_{\mathrm{source}} \propto \Delta T(x) \propto e^{-x/\xi}$ as source term for the wave equation (2.10), one can solve the wave equation analytically. The solution is given in Ref. [Tho86] and is shown for three different times after excitation in Fig. 3.3(a). A strain pulse propagating into the layer with the longitudinal speed of sound can be seen. Additionally a static strain at the surface is present, which does not disappear due to the missing simulation of heat diffusion.
Besides the analytical result, it is easy to explain the pulse shape qualitatively. The acoustic pulse width is given by the excitation depth ξ. From the calculation of the simple reflection coefficient in Section 2.5 it is straightforward to see that the initially generated stress will be reflected at the surface with a sign change. As the generated stress propagates in both possible directions, the leading part corresponds directly to the excited stress, while the trailing sign-changed part of the pulse stems from the reflection. In bulk there is no dispersion, so the pulse shape won't change with time and the pulse propagates with the speed of sound.
ii) $\xi > d$: A very long excitation length compared to the thickness leads to a homogeneous excitation, for example an optical pump pulse excites a semiconductor Si membrane. Over the whole thickness d an equal density of electron-hole pairs N_e/d will be generated [1]. The thermoelastic contribution is neglected here, leading to an initial homogeneous stress by deformation potential only: $\sigma_{\mathrm{source}} = \sigma_{\mathrm{DP}} = N_e \partial E_g / \partial \eta$. A negative initial strain is generated, which is shown in Fig. 3.3(b), along with its temporal evolution at one of the surfaces. The edge of the surface seems to propagate in the layer, while changing the strain from its initial value to zero. This can be explained clearly by the understanding of the calculated reflection coefficient. The built-up initial stress propagates in both positive and negative x-direction, while the latter will be reflected at the surface with a sign-change, leading the mutual compensation with its trailing part propagating with the speed of sound.
Heat flow: In the above generated strain pulses an instant excitation was assumed, neglecting heat dissipation, or electron-hole pair recombination, leading to very steep features in the pulse shape. By including a time-varying stress source, the changing temperature distribution will generate stress components by itself. The superposition of these will soften the sharp features. The heat diffusion is expressed by the thermal diffusivity $D = K/C_{\mathrm{P}}$, with K being the thermal conductivity. For metals a diffusional behavior of $D/v_{\mathrm{L}}\xi = 0.2 - 2$ is common [Tho86]. The thermalized pulse shape, assuming a thermal diffusivity of $D = v_{\mathrm{L}}\xi$, is shown in the inset of Fig. 3.4(a). A smoothening of the sharp features in the pulse shape can be seen. The impact on the phononic spectrum will be discussed in the next section.

3.5. Spectrum of coherent acoustic phonons

So far the temporal evolution of strain in a heterogeneously or homogeneously excited layer were discussed. The corresponding lattice vibrations are the before mentioned coherent acoustic

[1] The excitation profile along x is also influenced by the Fabry-Pérot cavity formed by the two surfaces of the membrane. However, ultrafast diffusion leads to a rapid homogenization of the carrier density

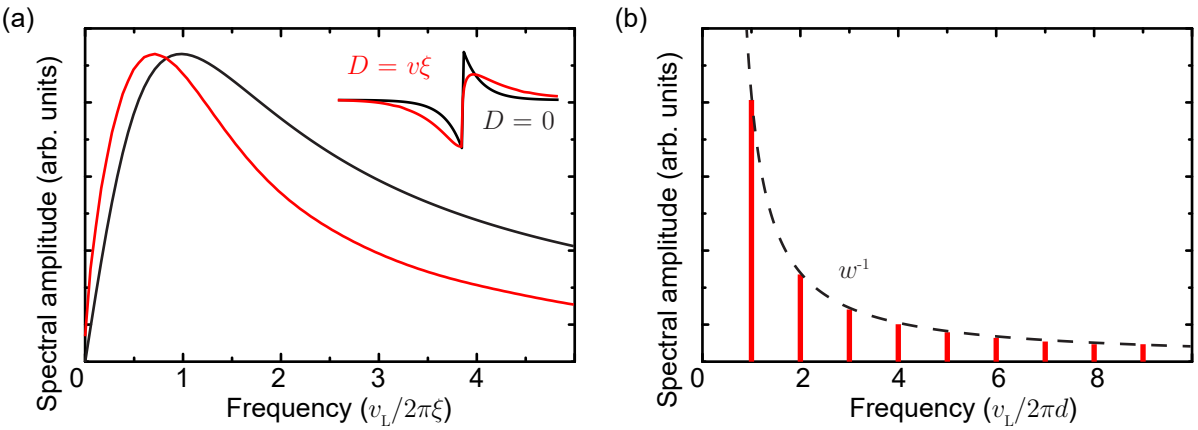

Figure 3.4.: (a) The spectral amplitude of the strain distribution of the two temporal pulses in the inset: (black) without heat diffusion and (red) with heat diffusion and the thermal diffusivity $D = v_L\xi$. The frequency has been rescaled with the factor $2\pi\xi/v_L$. (b) The spectral amplitude of the strain distribution of the homogeneously excited layer with the thickness d. Equally spaced modes at $f_n = nv_L/2d$ (with $n = 1, 3, 5...$) are visible, where the relative amplitude corresponds to a $1/n$-decay.

phonons. The corresponding frequency spectrum and changes to the spectrum – the dynamic evolution – can be calculated analytically. For the evaluation the pulse is described at its initial starting condition. With the help of the Fourier transformation and the convolution theorem the generated frequency spectrum can be derived.
First, the pulse shape is derived in the time domain, while setting the pulse origin at the surface ($x = 0$), corresponding to a non excited system with the pulse being injected at the surface.

3.5.1. Inhomogeneously excited layer

For the case of the heterogeneous excitation (with the excitation depth ξ), without loss of generality, the total asymmetric strain pulse has its symmetry center at $t = 0$. This means the leading part of the pulse has to be shifted to negative time delays and the trailing part will be shifted to positive times. And the generated strain pulse is formulated in the time domain:

$$G^{\varepsilon}_{\mathrm{het}}(t) \propto \begin{cases} -\exp(-v_L t/\xi) & t < 0 \\ \exp(v_L t/\xi) & t > 0 \\ 0 & t = 0 \end{cases} \tag{3.9}$$

The spectrum of the strain pulse can be derived by the Fourier transformation:

$$\tilde{G}^{\varepsilon}_{\mathrm{het}}(\omega) = \int_{-\infty}^{\infty} G^{\varepsilon}_{\mathrm{het}}(t) e^{-i\omega t} dt \propto \int_{-\infty}^{0} -e^{-t(v_L/\xi + i\omega)} dt + \int_{0}^{\infty} +e^{t(v_L/\xi - i\omega)} dt = \frac{-2i\omega}{v_L^2/\xi^2 + \omega^2} \tag{3.10}$$

The Fourier spectrum of the strain is plotted in Fig. 3.4(a). The spectrum consists in the beginning of a rising part proportional to ω upon which follows an amplitude decay proportional to ω^{-1}. The maximum is found at the frequency $f_{\max} = 2\pi\xi/v_L$. This spectrum shall be

compared to the case of an excited acoustic pulse in a material, where heat diffusion is not negligible (see red inset in Fig. 3.4(a)). The spectrum is shown in Fig. 3.4(a). Whereas the overall features are the same, the maximum shifts to a lower frequency and higher frequency components are less pronounced. This is in total agreement with the Fourier theorem, where sharp features correspond to high frequency components.

3.5.2. Homogeneously excited layer

The strain pulse of the homogeneously excited layer (over the whole thickness d) takes the form:

$$G^{\varepsilon}_{\mathrm{hom}}(t) \propto \begin{cases} 1 & -d/v_{\mathrm{L}} < t < 0 \\ -1 & d/v_{\mathrm{L}} > t \geq 0 \end{cases} \qquad \wedge \qquad G^{\varepsilon}_{\mathrm{hom}}(t + 2d/v_{\mathrm{L}}) = G^{\varepsilon}_{\mathrm{hom}}(t) \tag{3.11}$$

This corresponds to an infinite series of rectangular pulses. It is not possible to speak of a single pulse traveling in the system, but instead a pulse train is present. Therefore the next pulse has to be periodic with the thickness $2d$. To calculate the frequency spectrum first one has to express the strain pattern as a Fourier series:

$$G^{\varepsilon}_{\mathrm{hom}}(t) \propto \sum_{k=1}^{\infty} \frac{\sin((2k-1)\omega_1 t)}{2k-1} = \sum_{n=1}^{\infty} \frac{\sin(\omega_n t)}{n} \qquad (n = 1, 3, 5, ...) \tag{3.12}$$

where the frequency ω_1 is $2\pi/T$ with the period of the simple pulse $T = 2d/v_{\mathrm{L}}$. The frequency ω_n is an odd multiple of ω_1. Now it is straightforward to obtain the frequency spectrum which is shown in Fig. 3.4(b). It is characterized by regularly spaced peaks at the frequency of $f_n = nv_{\mathrm{L}}/2d$ $(n = 1, 3, 5, ...)$, where the individual modes have a relative amplitude relation proportional to $1/n$ (dashed line).

3.5.3. Asymmetrically excited bilayer

In the following two layers attached to each other are assumed, a system similar to the one described in 2.11. But contrary to the case discussed above, the thickness d_1 of the first layer is comparable to its absorption length ξ_1. Also a weak electron-phonon coupling is assumed which leads to a homogeneous excitation of layer 1. Additionally, the absorption length ξ_2 in layer 2 is larger than the thickness d_2. These assumptions are fulfilled by the bilayer system used in this thesis: 10-20 nm Al on 300 nm Si excited with pump light with the wavelength of 800 nm. Both excited strain pulses are able to propagate into the other layer. In the first approximation one neglects the reflection at the interface between the two layers. Additionally, just the evolution of the spectrum on a timescale smaller than the propagation time through layer 2 is discussed. The time for the strain to propagate from the surface to the interface of layer 1 is given by $t_1 = d_1/v_1$. The strain pulse excited in layer 1 is then given by:

$$G^{\varepsilon}_{1}(t) \propto \begin{cases} -1 & -t_1 < t < 0 \\ +1 & t_1 > t \geq 0 \\ 0 & \text{else} \end{cases} \tag{3.13}$$

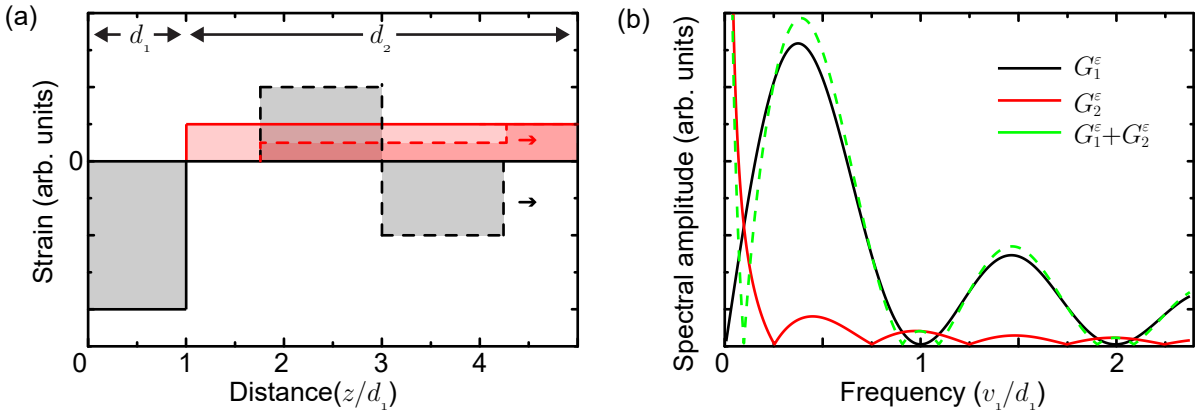

Figure 3.5.: (a) Strain in two perfectly adhered homogeneously excited layers assuming a different stress generation process with a different sign at initial conditions (solid line). The strain pulse of the surface propagates into the layer, while the strain pulse of layer 2 is propagating in both front and back direction (dashed line). (b) Spectral amplitudes of the two strain distributions of the homogeneously excited layers.

and it is possible to calculate the spectrum of the excited strain pulse to be:

$$\tilde{G}_1^\varepsilon(\omega) \propto \int_{-t_1}^{t_1} \mathrm{sign(t)} e^{-i\omega t} dt = \frac{1}{i\omega}(2 - e^{i\omega t_1} - e^{-i\omega t_1}) = -4i\omega^{-1} \sin^2(\omega t_1/2) \tag{3.14}$$

This strain distribution and its Fourier transformation are shown in gray in Fig. 3.5 for two different times: The initial starting condition (solid line) and a short time later (dashed line). Distinct minima at multiples of $\omega/2\pi = f = 1/t_1$ are visible.

In the next step the strain pulse from layer 2 in vicinity of the strain excited in layer 1 will be described, but the rear surface of layer 2 will be neglected. Due to the thickness of layer 2 being much larger than layer 1 ($d_2 >> d_1$), the strain discontinuity at the rear surface will not have a temporal overlap with the pulse from layer 1.

For the pulse generated at the second layer side of the interface the strain is assumed to have a different sign and the amplitude is modulated by a factor μ relative to the strain in layer 1. The strain distribution is homogeneous and half of the pulse will travel directly into layer 2, while half of it will pass again through layer 1 assembling one round trip:

$$G_2^\varepsilon(t) \propto \begin{cases} 1 & -\infty < t < t_1 \\ 0 & -t_1 < t < t_1 \\ +1 & t_1 < t < \infty \end{cases} \tag{3.15}$$

This leads to the spectrum of the strain:

$$\tilde{G}_2^\varepsilon(\omega) \propto \mu \int_{-\infty}^{-t_1} e^{-i\omega t} dt - \mu \int_{t_1}^{\infty} e^{-i\omega t} dt = \frac{-\mu}{i\omega}(e^{i\omega t_1} + e^{-i\omega t_1}) = 2\mu i\omega^{-1} \cos(\omega t_1) \tag{3.16}$$

This strain distribution and its Fourier transformation are shown in red in Fig. 3.5 for two different times: The initial starting condition (solid line) and a short time later (dashed line).

The factor μ was taken to be 0.2 compared to the strain derived in layer 1. Distinct minima at odd multiples of $\omega/2\pi = f = 1/4t_1$ are visible.
In the measurement only the spectra of both pulses together are detected, which is also displayed in Fig. 3.5(b). Due to the different signs a mutual compensation of the spectral components is appearing at $\omega = t_1^{-1}\arccos((1+\mu)^{-1})$.

3.6. Propagation and dynamics of phonons in bilayers

Above the initial spectrum directly after excitation was calculated. Here, the various changes to the acoustic pulse during its propagation are going to be discussed. The formalism will be introduced on the example of the before mentioned bilayer system. This will include reflection and transmission at interfaces and attenuation during the propagation. In particular the influence of a spring-loaded interface will be discussed.
In Section 2.5 the reflection and transmission coefficients for displacement waves at interfaces are derived. However, so far the spectrum was only discussed for strain waves. Therefore the strain spectrum has to be transferred to the displacement spectrum. The derivative of the mechanical displacement is the strain, and in the Fourier plane the derivative is the multiplication by ik, with $k = \omega/v$ the wave vector of the respective layer. For the integration from strain to displacement one multiplies the spectrum of the strain by $1/ik$. This yields for the spectrum of the displacement:

$$\tilde{G}^u(\omega) = \frac{v}{i\omega}\tilde{G}^\varepsilon(\omega) \tag{3.17}$$

With the help of these tools in the following the strain evolution in a bilayer system will be discussed.

3.6.1. Perfectly adhered interface

First, the strain generated homogeneously in layer 1 is discussed. Perfect adhesion is assumed and the reflection at the interface occurs only due to the impedance mismatch. The propagating pulse will be partially reflected at the interface, whereas the reflected part will have one round trip in layer 1 upon which a part will be transmitted, following the initial pulse, and another part will be reflected to undergo the same transition. With the reflection coefficient R_{12} and the transmission coefficient T_{12}, one can express the spectrum for the propagating displacement pulse including all reverberations:

$$\begin{aligned}\tilde{P}_1^u(\omega) &= (T_{12} + T_{12}R_{12}e^{-2i\omega t_1} + T_{12}(R_{12}e^{-2i\omega t_1})^2 + ...)\tilde{G}_1^u(\omega) &(3.18)\\ &= \tfrac{T_{12}}{1-R_{12}\exp(-2i\omega t_1)}\tilde{G}_1^u(\omega) &(3.19)\end{aligned}$$

The temporal shape of the propagating strain pulse is shown in Fig. 3.6(a) for an exemplary reflection coefficient of $R_{12} = 0.3$. Multiple reflections following the initial strain distribution can be seen. The spectra for different reflection coefficients ranging between 0 to 0.5 are shown in Fig. 3.6(b). For $R_{12} = 0$ no deviations between generated and propagating spectrum occur. But for larger reflection coefficients the widths of the maxima shrink. Additionally the peak position of the first maximum shifts to higher frequencies. But the minima do not change their position.

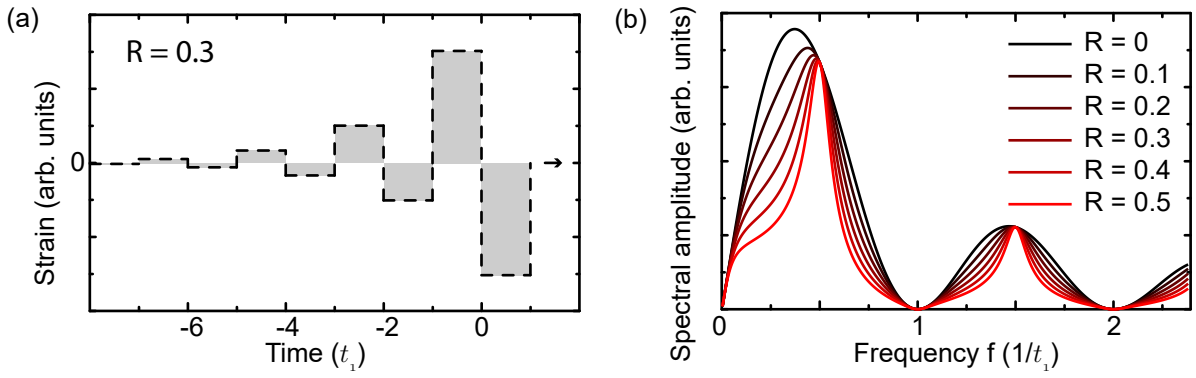

Figure 3.6.: (a) The homogeneously generated strain pulse in a thin layer propagating in a second layer including multiple reflections at the interface between both layers. (b) Different spectral distributions of the strain pulse distribution in dependence of the reflection coefficient at the interface. t_1 is the time the sound wave takes to propagate along the distance of layer 1.

Next, the change of the pulse spectrum and the temporal distribution of the strain pulse generated at the interface in layer 2 will be discussed. Layer 2 is homogeneously excited, which leads to the definition of the generated strain:

$$G_2^{\varepsilon}(t) \propto 1 \quad (-\infty < t < t_1), \qquad G_2^{\varepsilon}(t) \propto 0 \quad \text{(else)}.$$

And the spectrum becomes

$$\tilde{G}_2^{\varepsilon}(\omega) \propto \int_{-\infty}^{-t_1} e^{-i\omega t} dt = \frac{i}{\omega} e^{i\omega t_1}$$

This strain will have one part propagating directly into layer 2 and one part propagating into layer 1, getting directly reflected at layer 1, performing one round trip in layer 1, and getting reflected inside layer 1. The change in the spectrum is expressed by the spectral transfer function Γ derived earlier (see Eq. (2.41)):

$$\tilde{P}_2^u = (1 + \Gamma)\tilde{G}_2^u \tag{3.20}$$

The strain distribution propagating in layer 2 for a reflection coefficient of 0.3 is shown in Fig. 3.7(a). Multiple partial strain packets following the initial edge with the distance given by the round trip time $2t_1$ in layer 1 can be seen. The spectra for different reflection coefficients ranging from 0 to 0.5 are shown in Fig. 3.7(b). A higher reflection coefficient mostly smoothes the minima and has little effect on the maxima.

3.6.2. Spring-loaded interface

Here, the effect of a spring-loaded interface is discussed and its implications on the strain distribution in the bilayer system. Both layers are assumed to have the same impedances. The reflection and transmission are governed purely by the spring induced changes. The spectrum of the propagating pulse given by Eq. (3.19) has to be changed accordingly. The temporal distribution is shown in Fig. 3.8(a) for strong ($\eta t_1/Z = 21$) and weak ($\eta t_1/Z = 3$) adhesion. The shape of the pulse with strong adhesion looks similar to the shape with perfect adhesion, but

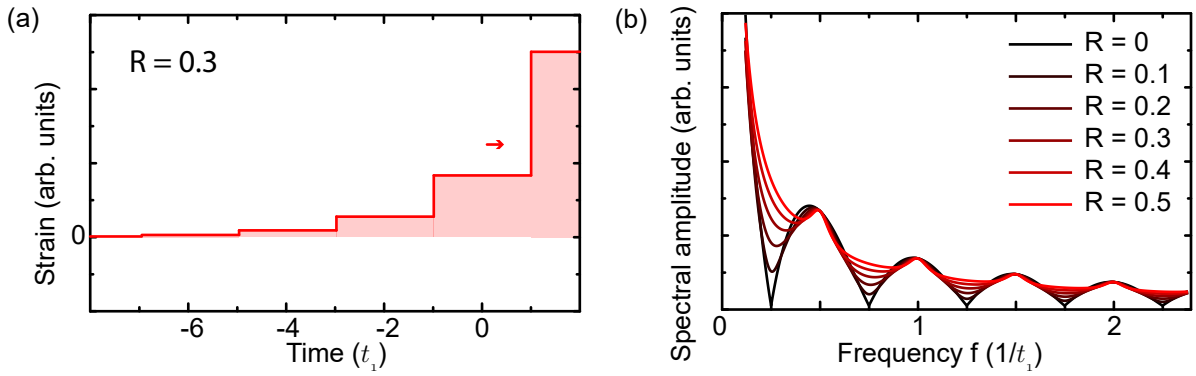

Figure 3.7.: (a) Simulation of a strain pulse generated homogeneously in a thick layer getting transmitted and reflected at the interface of a thin layer including multiple reflections at the interface between both layers. (b) Different spectral distributions of the strain pulse distribution in dependence of the reflection coefficient at the interface. $2t_1$ is the round trip time in layer 1.

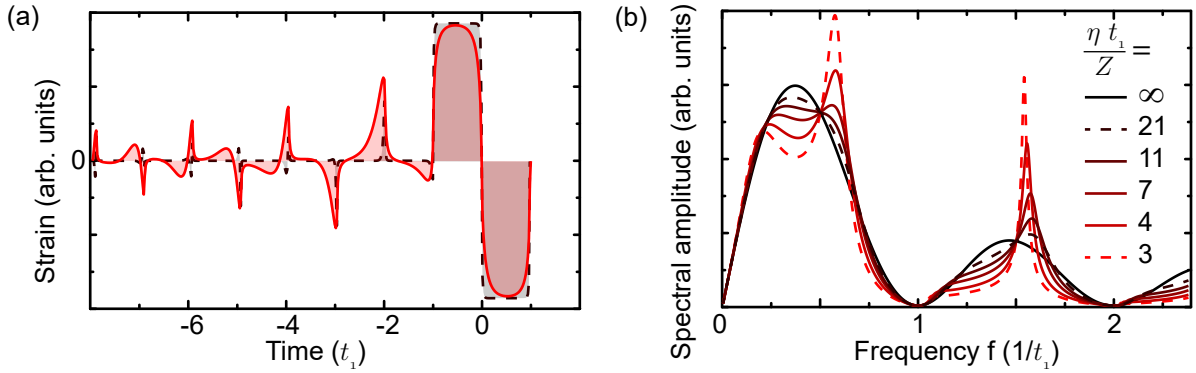

Figure 3.8.: (a) Simulation of two strain pulses generated homogeneously in a thin layer propagating in a thick layer including multiple reflections at the spring-only-dependent interface between both layers. The gray dashed line has a 7 times larger spring constant than the red line. (b) Spectral distributions of the 6 different strain pulses in the thick layer in dependence of the spring constant at the interface. $2t_1$ is the round trip time in layer 1.

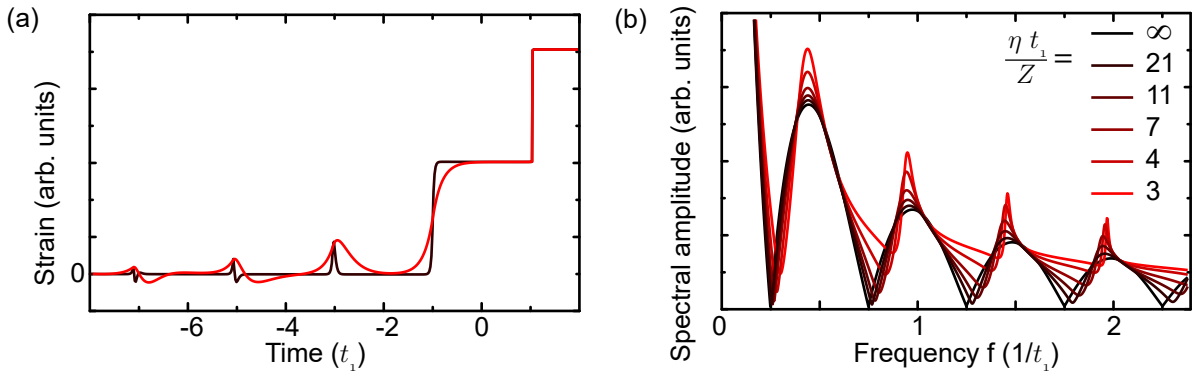

Figure 3.9.: (a) Simulation of two strain pulses generated homogeneously in a thick layer being transmitted and reflected at the interface of a weakly adhered thin layer including multiple reflections at the interface between both layers. The gray dashed line has a 7 times larger spring constant than the red line. (b) Spectral distributions of the 6 different strain pulses in the thick layer in dependence of the spring constant at the interface. $2t_1$ is the round trip time in layer 1.

intense delta-peak-like features appear every t_1. The peaks broaden and smear out for weaker adhesion. It is noteworthy that for weak adhesion also the initial strain distribution smears out at the edges.

These changes are also prominent in the spectra shown in Fig. 3.8(b) for 6 different spring constants. While for very large spring constants perfect adhesion is derived, for smaller spring constants a strong spectral change can be seen. The maxima develop local minima at their previous maximum position with two local accompanying maxima. The local maximum at higher frequencies grows and sharpens disproportional compared to the local maximum at lower frequencies.

Here, the change of the strain distribution in layer 2 due to a spring loaded interface is discussed. Eq. (3.20) is varied and the reflection and transmission coefficients are exchanged with their spring-loaded counterpart and identical impedances. The results for the same spring constants as before are shown in Fig. 3.9. For the temporal distribution, compared to the other pulse, weaker deviations from the perfectly adhered case are visible (see Fig. 3.9(a)). Following the weakening of the spring constant the edge sharpness is reduced. Additionally new peak features arise after each round trip time ($2t_1$). The peaks get broader with smaller spring constant. The weaker change is also visible in the frequency regime (see Fig. 3.9(b)). With smaller spring constants the maxima grow and the minima smear out while transitioning to higher frequencies.

Finally, the differences between reflection governed by impedance mismatch and reflection governed by a spring bonding are summarized. The reflection at an interface with different impedances is the same for all frequency components, which leads to linear reproduction of the initial strain shape upon reflection. In contrast, the reflection at a spring-loaded interface is frequency dependent, which leads to complex features upon reflection. In the reflection of the thin film, this manifests itself after each round trip time as a sharp peak-like structure.

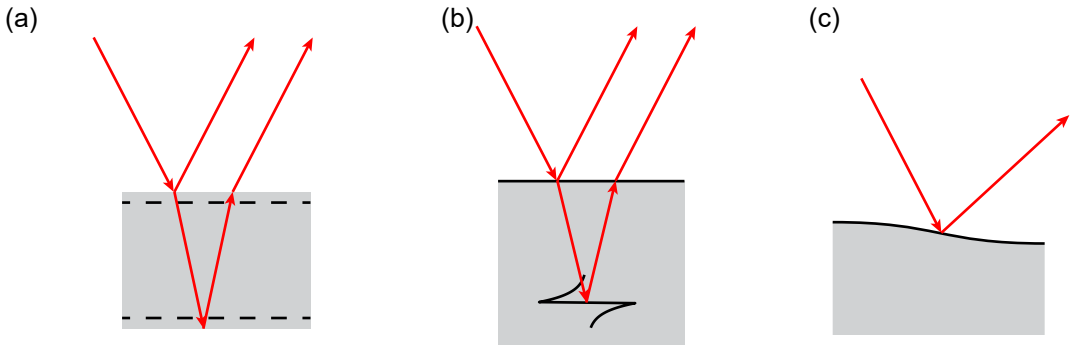

Figure 3.10.: (a) Schematic of the Fabry-Pérot effect due to light (red lines) reflection at two parallel interfaces. The interfaces are depicted as the surfaces of a dilated membrane (equilibrium as dashed lines). (b) Schematic of the dynamic Fabry-Pérot effect due to light (red lines) reflection at an interface and a propagating strain pulse. (c) Schematic of an obliquely deflected light beam by a distorted interface.

3.7. Strain detection

In this section the different detection mechanisms will be discussed. In this work the strain-related properties are measured by the change in optical reflection of a probe pulse. The strain of the coherent acoustic pulse leads to two distinct changes of the optical properties shown in Fig. 3.10: This is (a) a displacement of an interface and (b) a change of the refractive index. The light beams reflected at the different interfaces and/or strain discontinuities superpose after reflection and interfere on a detector. Given by the time-dependent optical path length differences between the locations of reflection and a strain-dependent variation of the optical reflection coefficient, a time-varying intensity will be incident on the detector.

It is necessary to assume an optical pulse with a coherence length larger than the sample length including multiple reflections (200 fs corresponds to 30 µm) and to assume also a small spectral width (10 nm), which allows to limit the necessary discussion to a single wavelength, given by the central wavelength of the pump and probe pulses respectively. Additionally, just the case of perpendicular incidence and longitudinal acoustic phonons are discussed.

3.7.1. Interferometric detection

For the interferometric detection two parallel surfaces are assumed as depicted in Fig 3.10(a). Due to a change in refractive index at the surface from n_1 to n_2 a part of an incident light beam will be reflected and a part will be transmitted. Absorption is neglected. The transmitted beam will be partially reflected at the back surface and both beams interfere after the second beam is transmitted parallel to the first beam. The second beam will also be reflected at the front surface and undergo the round trip again. Considering all reverberations this resembles a Fabry-Pérot cavity. This leads to a static reflectivity depending on the probe wavelength and the optical path length between the two surfaces. The optical intensity reflection R at each surface is derived from the Fresnel formulas and is similar to the reflection of a strain pulse at

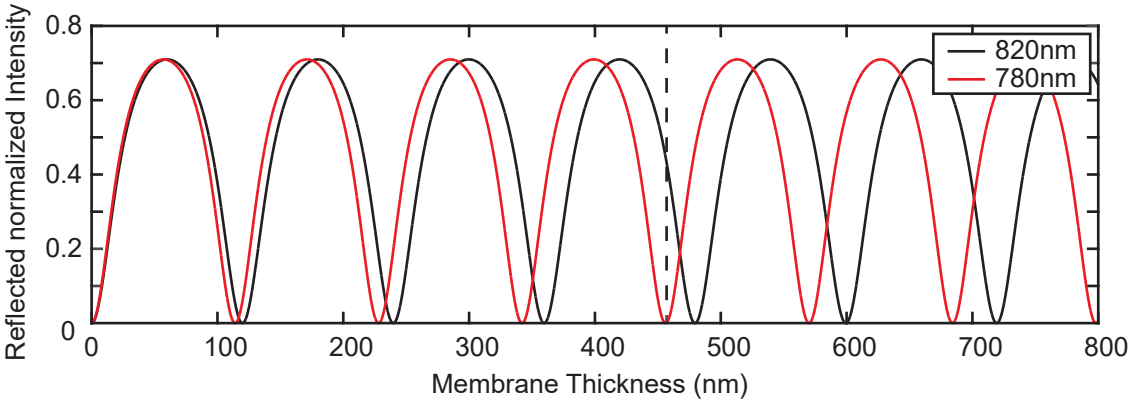

Figure 3.11.: Static reflectivtiy in dependence of the thickness of a Si membrane.

an interface (when exchanging the impedance with the refractive index):

$$R = \left| \frac{n_1 - n_2}{n_1 + n_2} \right|^2 . \tag{3.21}$$

Assuming an incident beam with the intensity I_0, the sum of all reflected parts at the two interfaces yields the total reflected intensity I_R, which includes interference due to all reverberations. The quotient between both gives with the surrounding layer air ($n_1 = 1$) the intensity modulation of a Fabry-Pérot cavity:

$$\frac{I_\mathrm{R}}{I_0} = \frac{F \sin^2(2\pi n_2 d/\lambda)}{1 + F \sin^2(2\pi n_2 d/\lambda)} \tag{3.22}$$

with the film thickness d and the wavelength λ. $2n_2 d$ is the optical path difference of each iteration of reflection between the interfering light beams. The finesse F describes the quality of the Fabry-Pérot cavity:

$$F = \frac{4R}{(1-R)^2} \tag{3.23}$$

The intensity modulation calculated for a Si membrane ($n_2 = 3.68$) for two different wavelengths in dependence of the thickness is shown in Fig. 3.11. The reflectivity for a single Si surface is 32 %, but has values between 0 to 76 % for the membrane. A continuous oscillating intensity distribution can be seen. Starting with zero reflectivity at zero thickness due to the optical phase jump of the first reflected light beam in respect to the transmitted ones, which leads to a total compensation, maxima every odd multiple of $d_\mathrm{max} = \lambda/4n$ and minima every $d_\mathrm{min} = \lambda/2n$ are visible.

By exciting the membrane, as discussed in Section 3.4, a strain induced elongation or compression leads to a change of total thickness. This will lead to a change in intensity of the reflected light. To increase the sensitivity of this method it is desirable that the relative intensity change has a maximum, i.e. that the slope in the static reflectivity is maximal.

The dashed line in Fig. 3.11 shows a thickness where the reflection for light with 780 nm is minimized, while for light with 820 nm wavelength the intensity modulation with thickness variation is maximized. Hence, the pump should have 780 nm and the probe 820 nm for a thickness of 450 nm.

When assuming the strain to induce a thickness change only, it is straightforward to extract the maximum strain from a measurement. The measured reflectivity changes are directly linked with the thickness changes given by the Fabry-Pérot modulation. For Si membranes with 350 nm thickness and a probe wavelength of $\lambda = 820\,\text{nm}$ the measured change in reflectivity is typically smaller than 10^{-4}. One can extract from Fig. 3.11 that this corresponds to a total change of the membranes thickness smaller than 5 pm. As the strain is the ratio between distortion and total length this yields for the strain $\varepsilon < 10^{-5}$. But one has to keep in mind that the strain not only changes the thickness in the system but also the refractive index might change. This will be discussed in the next section.

3.7.2. Photoelastic detection

For the explanation of photoelastic detection the discussion will be limited to the case of a half-infinite layer. In general the dielectric function is given by the electronic distribution in a material. Due to the strain the lattice will change from its equilibrium position and the electronic system will follow. The change of the real and complex refractive indices n and κ can be described in terms of the strain in first order as [Tho86]:

$$\Delta n(x,t) = \frac{\partial n}{\partial \varepsilon}\varepsilon(x,t) \qquad \Delta\kappa(x,t) = \frac{\partial \kappa}{\partial \varepsilon}\varepsilon(x,t). \tag{3.24}$$

A change of the refractive index will lead to a partial reflection of light. This means, as the strain changes the refractive index changes also.

This results in the reflectivity change

$$\Delta R(t) = \int_0^\infty f(x, \frac{\partial n}{\partial \varepsilon}, \frac{\partial \kappa}{\partial \varepsilon}, n, \lambda)\varepsilon(x,t)dx, \tag{3.25}$$

with the sensitivity function $f(x, \frac{\partial n}{\partial \varepsilon}, \frac{\partial \kappa}{\partial \varepsilon}, n, \lambda)$. It describes how the strain induced reflection at a given distance from the surface changes the total optical reflectivity. From this effect it is straight forward to explain the time-resolved Brillouin-scattering. This is depicted in Fig. 3.10(b). The incident light beam is (i) reflected at the surface and (ii) reflected at the refractive index discontinuity induced by the strain pulse. The strain pulse propagates into the substrate with the longitudinal speed of sound v_L. This leads to a modulation of the reflected light with the Brillouin frequency

$$f_\text{Brillouin} = \frac{2nv_\text{L}}{\lambda}. \tag{3.26}$$

From the measurement of this frequency one is either able to determine the refractive index of the material if the speed of sound is known, or the speed of sound if the refractive index is known.

3.7.3. Deflection detection

Contrary to the mechanisms discussed above, there is also a strictly geometric method. In principle a distortion of the surface diverts the direction of the reflected light beam (see Fig. 3.10(c)). The surface will only distort a small amount when using non-damaging pump energies. This change of the reflection angle and therefore a change in light intensity on a given point can not be resolved in the setup. Due to the large numerical aperture of the objective and the corresponding large entrance angle, the deflected light will still be gathered. Further details regarding a deflection setup are given in [Wri95].

3.7.4. Bilayer detection

Here, the detectable time signal for the case of the earlier discussed bilayer system will be explained (see Section 3.6). For the sake of clarity photoelastic detection and a constant sensitivity function in the first layer are assumed, while the sensitivity function is zero in the second layer. The detection of the strain is thus only in the first layer. Incident on the first layer will be the displacement pulse $\tilde{P}^u$. The emerging detectable displacement in the first layer $\tilde{D}^u$ is going to be calculated here. This consists of the transmission from the second into the first layer and the subsequent reflections at the interface multiplied by the incident displacement spectrum:

$$\tilde{D}^u(\omega) = T_{21}(1 + R_{12}e^{-2i\omega t_1} + (R_{12}e^{-2i\omega t_1})^2 + ...)\tilde{P}^u(\omega) = \frac{T_{21}}{1 - R_{12}\exp(-2i\omega t_1)}\tilde{P}^u(\omega) \quad (3.27)$$

Contrary to the Fabry-Pérot effect, where one would detect the displacement, here only strain will be detected photoelastically and thus the strain field has to be calculated. The displacement spectrum can be easily rewritten into the displacement field

$$\tilde{u}_{det}(\omega, x) \propto \tilde{D}^u(\omega)(e^{-ik_1 x} + e^{ik_1 x}) \quad (3.28)$$

And one can write with Eq. (2.4) for the strain field:

$$\tilde{\varepsilon}_{\mathrm{det}}(\omega, x) \propto -ik_1\tilde{D}^u(\omega)(e^{-ik_1 x} - e^{ik_1 x}) \quad (3.29)$$

The reflectivity change given by the photoelastic detection was introduced in Equation (3.25):

$$\Delta\tilde{R}(\omega) = \int_0^\infty f(x)\tilde{\varepsilon}_{\mathrm{det}}(\omega, x)dx \quad (3.30)$$

Thus one gets in a first approximation with a homogeneous sensitivity function in layer 1:

$$\Delta\tilde{R}(\omega) \propto -ik_1\tilde{D}^u(\omega)\int_0^{h_1}(e^{-ik_1 x} - e^{ik_1 x})dx \propto \tilde{D}^u(\omega)\sin^2(\omega t_1/2) \quad (3.31)$$

This leads in total to the detectable reflectivity change for the bilayer system, only excited in layer 1 and the vicinity of the interface in layer 2, and only detecting the first echo (inserting

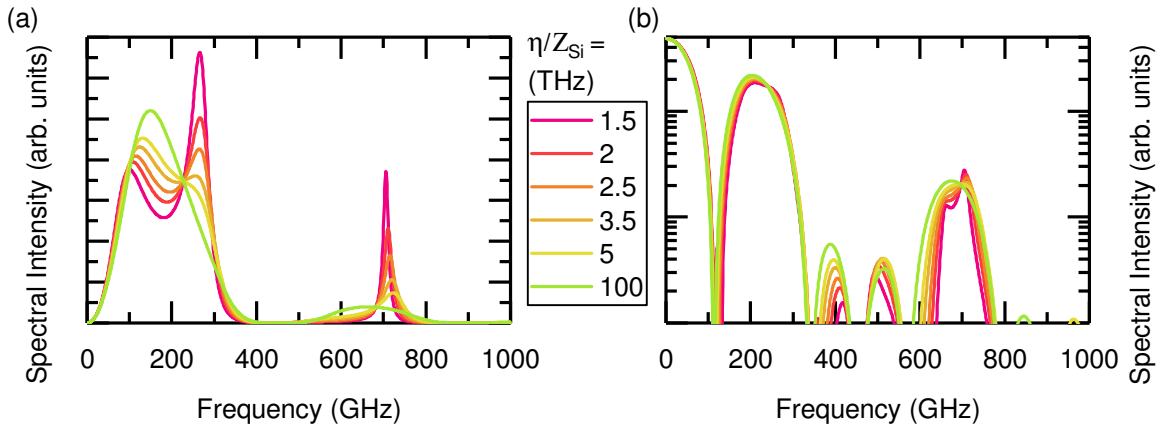

Figure 3.12.: Detected spectrum for an Al/Si-system. (a) Simulation of the spectral intensity of the strain generated homogeneously in a thin Al layer propagating in a thick Si layer including multiple reflections at the spring-only-dependent interface between both layers and the subsequent detection in the thin layer. (b) Spectral distributions of the detected strain generated homogeneously in the second layer (Si). Reflections stem from the impedance mismatch and the spring coupling.

Eqs. (3.14), (3.16), (3.17), (3.19), (3.20), (3.27)):

$$\Delta\tilde{R}(\omega) \propto \omega^{-2}\sin^2(\omega t_1/2)\frac{T_{21}}{1-R_{12}\exp(-2i\omega t_1)}\times \left[\frac{T_{12}}{R_{12}\exp(-2i\omega t_1)-1}\sin^2(\omega t_1/2)+\mu\frac{v_2}{2v_1}(1+\frac{T_{12}}{\exp(-2i\omega t_1)-R_{12}})T_{21}\cos(\omega t_1)\right] \quad (3.32)$$

where μ is a factor describing the relative intensities of the stress generation in layer 1 and 2. Subsequent echoes can be calculated by multiplying the spectrum of the first echo with the spectral transfer function Γ ((2.41)). The spectra of the expected pulses from layer 1 are plotted in Fig. 3.12(a), while the spectra of the pulses generated in layer 2 are plotted in Fig. 3.12(b). Depending on the relative sign of stress generation, these spectra have to be summed up or subtracted. The simulation values stem from the system of a 13 nm thick Al film (layer 1) on a Si substrate (layer 2). Dissipation effects are neglected. It shall be noted that it is straight forward to obtain the temporal data by a Fourier transformation of the spectrum.

3.8. Conclusion

In this chapter the generation and detection processes for coherent acoustic phonons were discussed. Regarding the excitation it was shown that metals and semiconductors may exhibit very different electronic properties, leading to a very different stress in the lattice. The following coherent stress (with a fixed phase relation to the pump pulse) leads to the build-up of coherent acoustic phonons. Depending on the material properties like thickness and absorption, the strain profile differs quite dramatically. Different strain profiles were discussed and the propagation in a bilayer was shown in the frequency space. The possible detection processes regarding an optical method were discussed. Finally the complete detected spectrum of a bilayer was calculated and explained.

Chapter 4

Experimental setup and sample fabrication

4.1. Hypersonic spectroscopy utilizing an optical pump-probe setup

The understanding of the processes discussed in this thesis necessitates the use of a measurement technique which is able to resolve those processes on sub-ps timescales. This requires to measure frequencies in the range of $1-10,000\,\mathrm{GHz}$. Additionally, it is favorable to facilitate a non-invasive and non-destructive technique. Hence, optical tools are the perfect choice to excite the sample and detect the coherent signal of acoustic and optical phonons (see Section 3.2). Ultrashort laser pulses allow to excite and detect ultrafast processes. The temporal dynamics are resolved with an optical pump-probe setup using the asynchronous optical sampling method.

4.1.1. Ultrafast pump-probe spectroscopy

Pump-probe spectroscopy is the name for a technique using a pump to excite a sample and a probe to detect the changes induced in the sample by the pump. By varying the time delay between pump and probe pulses one is able to detect the temporal changes in the sample. This assumes every pump incident to be indistinguishable one from another. While the signal-to-noise ratio for one transient might be very low, due to averaging of single measurements it is possible to reduce the noise. However, the averaging allows only to detect pump induced changes as any other intensity changes of the detected probe pulse are not correlated and are lost in the averaging process. The temporal distance between the individual time delays and the temporal length of pump and probe pulses limit the temporal resolution of the system.

In conventional optical pump-probe setups [Bre78, Nel82, Lyt85, Tho86, Sha99] the pulses of a single mode-locked laser are used. A beam splitter divides the pulse train into two beam paths, where one acts as the pump and one as the probe. The path length of the probe beam can be varied by a delay stage. To assemble a time delay of 1.25 ns (the time window of the setup used in this thesis) a delay of 18.5 cm is necessary. This method has some disadvantages. A translation stage may not move linear, which diminishes the accuracy of the time step, large distances will lead to a beam walk of the probe beam, and the time-zero-point has to be found. Those disadvantages are solvable, but the compensation can get difficult.

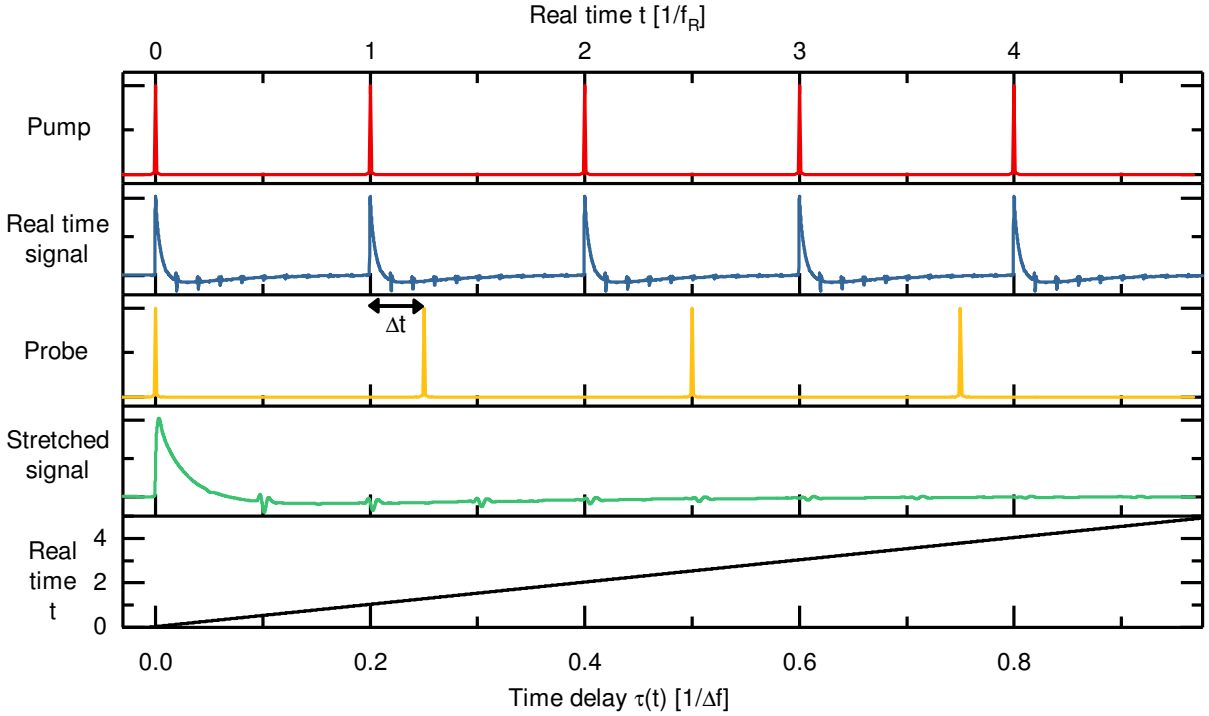

Figure 4.1.: Schematic description of asynchronous optical sampling. Top row: The pulse train of the pump pulses is shown with the real time normalized to the time between two pulses, e.g. the inverse repetition rate of the pump laser. Second row: A schematic real time signal which is excited with every pump pulse. Third row: The pulse train of the probe pulses with an additional time delay of Δt with each additional pulse. Fourth row: Due to the increased time delay between pump and probe the measured signal is reproduced from the real time signal with a stretching factor. Last row: Real time versus measurement time delay.

Asynchronous Optical Sampling

To avoid the mechanical delay line, one can employ the asynchronous optical sampling (ASOPS) principle [Elz87, Ada95, Tak99]. Instead of one laser delivering both pump and probe pulses, two lasers are used, one for the pump and one for the probe pulse. This is shown in Fig. 4.1. The temporal development of the excited sample, the pump and probe pulses, the measured signal and the real time versus measurement time is shown. A fixed frequency offset $\Delta\nu$ between both lasers leads to a consecutively increasing time delay between both the pump and probe pulses. Let the pump have the repetition rate ν_R and the probe the repetition rate $\nu_R - \Delta\nu$. While the pump excites the sample every $t = 1/\nu_R$, the probe scans the response of the sample. The time zero is assumed to be when both pulses hit the sample at the same time. At the next time step the probe pulse will be delayed with respect to the pump pulse by (under the condition $\Delta\nu << \nu$)

$$\Delta t = \frac{1}{\nu_R + \Delta\nu} - \frac{1}{\nu_R} = \frac{\Delta\nu}{\nu_R(\nu_R + \Delta\nu)} \approx \frac{\Delta\nu}{\nu_R^2} \tag{4.1}$$

The next data point will be the signal from the probe pulse $2\Delta t$ after the pump pulse. This happens $(\nu/\Delta\nu)$ times, until both pump and probe hit the sample at the same time again. The measurement of one whole time window takes $1/\Delta\nu$ with the number of data points $\nu/\Delta\nu$. This gives the relation between real time and measured time delay:

$$\tau(t) = \frac{\Delta\nu}{\nu_R} t \tag{4.2}$$

Assuming $\nu_R = 800\,\text{MHz}$ to be the repetition rate and a repetition rate offset of $\Delta\nu = 5\,\text{kHz}$ one time trace takes 0.2 ms with a nominal time resolution of 8 fs.

4.1.2. Laser system

The acoustic dynamics are investigated with a pump-probe setup utilizing high-speed ASOPS. The system is shown in Fig. 4.2 and is described in detail in [Bar07]. A Coherent 10 W Verdi V-10 laser with a wavelength of 532 nm pumps a GigaOptics GigaJet TWIN laser with two cavities. Each cavity consists of a Ti:sapphire crystal and 6 mirrors establishing a ring cavity. The mirrors and an additional silica prism are dispersion compensating elements. The prism also allows to tailor the dispersion and change the central wavelength between 750 and 850 nm. The pump light is focused into the Ti:sapphire crystal, where it overlaps spatially with the stimulated emission fed back into the crystal by the ring cavity. Due to the Kerr-lens of the Ti:sapphire crystal, the pump beam is focused with the crystal and a better overlap of pump beam and laser beam is established. The light is coupled out of the cavity by one mirror acting as the output coupler (OC). The pulse length is below 50 fs and the spectral width is $< 20\,\text{nm}$. The OC is also movable to adjust the cavity length and the repetition rate is around $f_R = 800\,\text{MHz}$. This defines a measurement window given by $1/f_R = 1.25\,\text{ns}$.
One oscillator is called the master and one the other one the slave, where the slave laser has a slight repetition rate offset from the master of 5 kHz. The repetition rate and the repetition rate offset will fluctuate due to thermal expansion and vibrations. Therefore the offset is actively stabilized by two of the mirrors in the slave laser's cavity being mounted on piezoelectric crystals. The stabilization works as follows: The repetition rate of each oscillator is measured behind

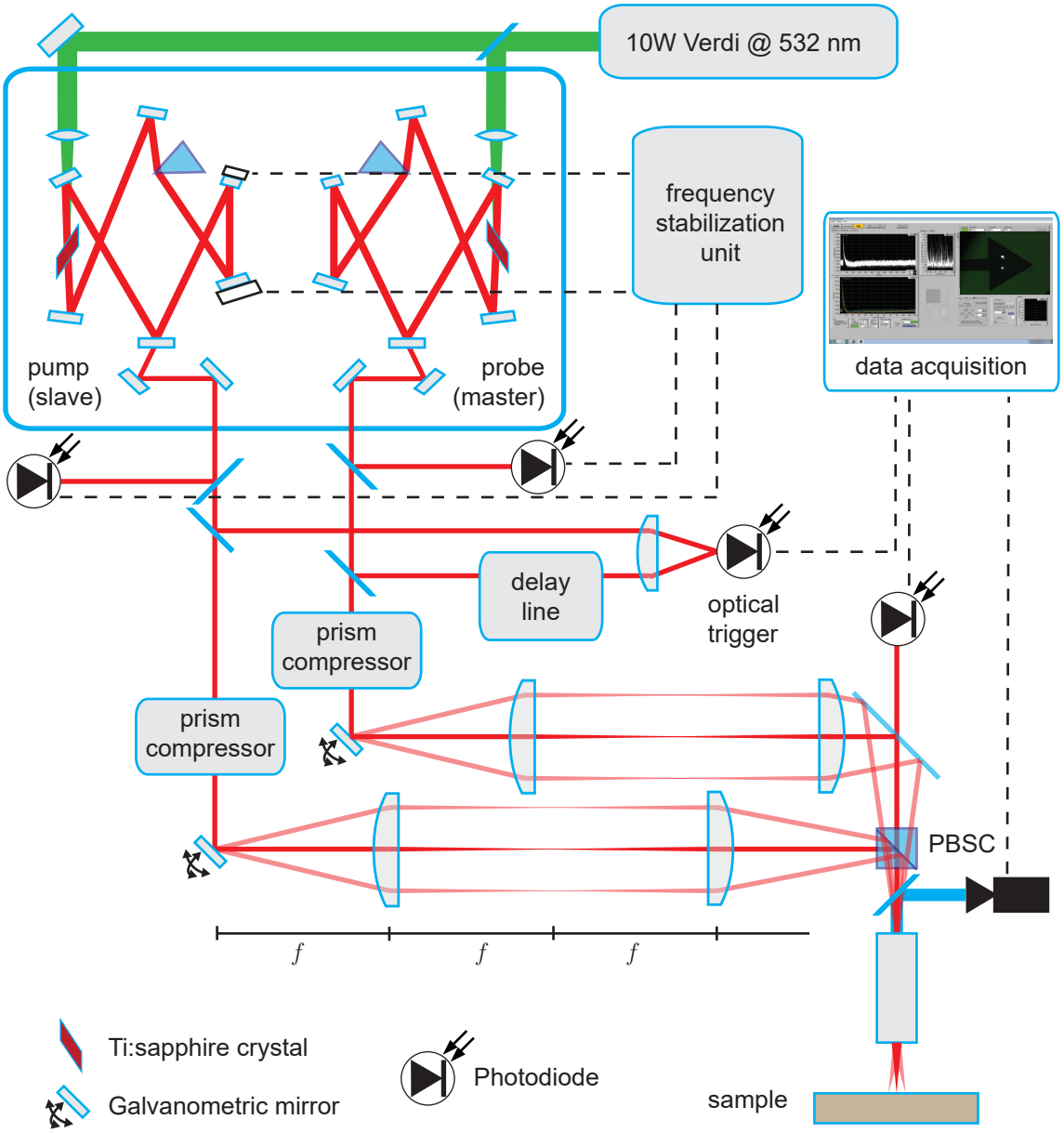

Figure 4.2.: Overview of the experimental setup. Optical paths are drawn with solid lines, electrical paths with dashed lines. Three optical paths through the $4f$-setup are shown for normal incidence parallel to the optical axis in red and for two non-normal incidence angles (exaggerated) in light red. Further details are given in the text.

the output coupler with a photodiode with a bandwidth that is at least 12.5 GHz. The high bandwidth is needed to detect higher harmonics of the repetition rate and, hence, to enhance the sensitivity. The 12th harmonic of the master is mixed with the 12th harmonic of the slave minus the electronically adjusted target repetition rate offset. The mixed signal is fed into an electronic stabilizing unit, which changes the voltage on the piezoelectric crystals to change the cavity length accordingly to minimize the frequency-offset variation. The 5 kHz offset corresponds to a minimal time resolution of 8 fs. This is smaller than the actual resolution, because also the optical pulse lengths and the timing jitter are important. The oscilloscope is a CompuScope, Gage 14200, which has a bandwidth of 125 Mbit/s and the detector is a New Focus 1801FS with 125 MHz bandwidth.

Hence, the laser pulses from the master and slave have a linear increasing time delay and one measurement over the whole time delay is done in 0.2 ms. This allows to accumulate a large number of measurements in a very short time, which results in a signal-to-noise ratio better than 10^7 in 10^3 s.

To determine the starting time of one measurement and to be sure that every transient will have the same phase corresponding to the pump pulse, an optical trigger is used. This is a photodiode made of GaP (EPD-440-0/0.9), which only absorbs light between 190 and 570 nm. A part of the light from both oscillators is incident on the GaP-diode. Due to two-photon absorption the excited electron-hole pairs generate a unique and distinct voltage spike corresponding to the time, at which both pulses are incident at the same time on the trigger. Due to the large non-linearity of this process, one pulse alone does not have enough energy to excite sufficient electron-hole pairs. To compensate for an arbitrary time delay between pump and probe on the trigger diode, which could shift the time zero of the measurement, a variable time delay is included in one of the beam paths with a mechanical delay stage.

To detect the reflectivity changes of the sample a collinear microscope setup is used. Both beams are polarized perpendicular to each other and are overlapped with a polarizing beam splitter cube. The microscope objective (Mitutoyo M Plan Apo NIR $50x$, NA= 0.42) focuses the laser spots down to a spatial FWHM below 2 µm. The reflected probe light is focused on a photodiode. The pump beam is separated from the probe beam in front of the detector with a polarizer and most of the times a color filter, as it is easily possible to separate pump and probe wavelength with the double cavity setup. Each cavity can be tuned between a wavelength of 750 to 850 nm while keeping the repetition rate stable. Thus pump and probe can have different wavelengths.

It shall be noted, that the different optical elements (beam splitter cubes, microscope objective) increase the group velocity dispersion and the optical pulses are stretched to 200 fs. To decrease the group velocity dispersion, a single-prism compressor can be included in the beam path. The laser pulses pass four times through the tip of a silica prism, assembling negative dispersion with every round trip. By tuning the optical path length behind the prism the amount of negative group velocity dispersion can be adjusted. Utilizing this setup the pulses can be shortened to a FWHM < 68 fs [He15].

The microscope objective is a plan-apochromat, which guarantees a flat image surface over the entire field of view. By slightly detuning the input angle in the objective one is thus able to move the laser spot on the sample up to 30 µm. Additionally the pump and probe spots can be separated from each other, which allows to measure lateral phonon propagation. In the work of this thesis two galvanometric scanner were included in the setup to be able to control the

movement of the laser spots in a very precise way.

4.1.3. Scanning 2D pump-probe

The plan-apochromacy of the microscope objective allows to keep a good beam spot size in the focal plane while entering it under an angle. The angle-entrance leads to the spot being at a different position in the focal plane. To be able to change this position precise and reproducible a galvanometric scanning units is implemented [Tac06, Wid15].
The galvanometric scanner consists of 2 movable mirrors, which allow to deflect the beam in x- and y-direction. The scanners (Cambridge Technology 8320K) have an angle resolution of $\Delta\alpha < 8\,\mu\text{rad}$, which enables position changes of the laser spot far below the spot size itself.
The deflection not only changes the angle of propagation but also the propagation direction. To be able to continuously sweep the entrance angle on the objective without shifting the laser spot on the entrance pupil, a $4f$ setup is implemented. This is depicted in Fig. 4.2. The moving mirrors of the scanner are assumed at the origin. After the distance of f, it will pass a confocal plan-convex lens with the focal distance f. This leads to a focus of the laser beam at the distance $2f$. A second lens at the distance $3f$ leads to a parallel beam again. It leads to an identical image of the laser beam leaving the galvanometric scanner on the entrance pupil of the objective. The entrance angle can be changed arbitrarily, by the use of the scanner without distorting the spots in the focal plane on the sample. Pump and probe spots can be moved both dependently and independently from each other, which allows for the detection of lateral phonon propagation.
The detectable area without distortion of the spots and detection errors $\approx 50\,\mu\text{m}$ and limited by the manual tracking on the detector. Because the detector is not mounted in a $4f$ setup and the distorted probe beam also leaves the objective under an angle, the focused beam misses the detector for larger distortions.

4.2. Sample fabrication and characterization

The roughness, doping and general quality of the samples is of great importance for accurate measurements. Therefore, nearly all investigated samples were fabricated in the nanostructure laboratory at the University of Konstanz and in the group of Stefan Fascko in the Helmholtz-Center Dresden-Rossendorf. Si membranes were fabricated with thicknesses between 250 and 350 nm. Those membranes were either structured nanoscopically with ion beams or nanopatterned with Al structures. With the help of ellipsometry, atomic force microscopy, and scanning-electron-microscopy the effects of the different treatments were quantified.

4.2.1. Si membranes

The single crystalline Si membranes are obtained from a commercially available Si-on-insulator wafer with a layered structure of 500 µm Si, 400 nm SiO_2 and 350 nm Si shown in Fig. 4.3(a). In the beginning of this thesis, a process developed by Waitz [Wai12a] was used. While the front side – the thin Si side – is protected by a poly(methyl methacrylate) (PMMA) layer, the bulk Si is wet etched from the backside with potassium hydroxide using a Si-nitride etch mask [Bru97]. The residual SiO_2 layer acts as an etch stop for the wet etching and is removed by consecutively dipping the wafer in hydrofluoric acid. The area of the free-standing Si membranes is defined

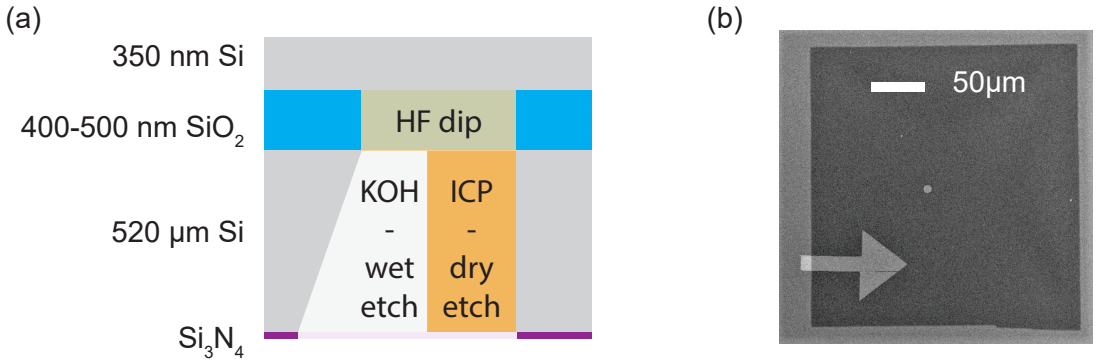

Figure 4.3.: (a) Fabrication process of the Si membrane. First the Si_3N_4-protection mask on the backside is opened by laser ablation. Then the substrate is removed with either an KOH-wet etch, or an ICP dry etch until the SiO_2 stop layer is reached. The SiO_2 is removed by a subsequent HF dip. Further details are given in the text. (b) Scanning electron microscope image of a Si membrane. The dark rectangle corresponds to a membrane and looks darker due to a large amount of electrons transmitted through the membrane. This membrane has already been processed and the burn spot and an Al arrow evaporated on the bulk and membrane are visible.

by the respective Si-nitride etch mask and is usually $600 \times 600\,\mu m^2$ large. The thickness is along the [100]-direction and given by the initial layer of 350 nm.
One disadvantage of this approach was the arbitrary breaking of the wafer upon the etchant reaching the vicinity of the SiO_2-layer. To overcome this problem, a distinct dry etching technique was developed. An inductively coupled plasma ignites the etching-plasma of O_2 and SF_6. By parallel plate reactive-ion-etching a highly anisotropic etch profile is obtained with an etching rate of $\approx 110\,nm/s$. Further details regarding this process can be found in the thesis of Haberland [Hab15]. Contrary to the wet-etching where a rectangular profile will form, due to the high anisotropy of the dry-etching, it is possible to etch arbitrary profiles into Si, depending on the mask. Round membranes with a diameter of up to 2 mm were fabricated also.
To reduce the risk of scattered ions bombarding the front side of the membrane, later a combination of both methods was used. While the majority of the wafer is wet-etched, the last 20 µm of the Si backside are dry etched. Thereafter, the removal of the residual SiO_2-layer is done with hydrofluoric acid. It shall be noted, that a too long treatment with hydrofluoric acid results in an increased fragility of the Si membrane [Wai12a].

4.2.2. Ion milling

To examine the influence of the surfaces on the phonon properties of Si membranes, the membranes were nanopatterned: One approach is to thin the membranes, which leads to higher frequencies of the eigenmodes. The other approach is to bombard the surface under an angle with ions. This restructures the surface in a Wadden-Sea-like manner. Two different approaches to thin the membranes are used: i) reactive-ion etching with sulfur hexafluoride and oxygen and ii) Ar^+-ion beam milling with a flux of $1.2 \times 10^{17}/cm^2$ at an acceleration voltage of 300 V [Kel08, OI09]. The native oxide layer present at the membrane's surface leads to a large factor

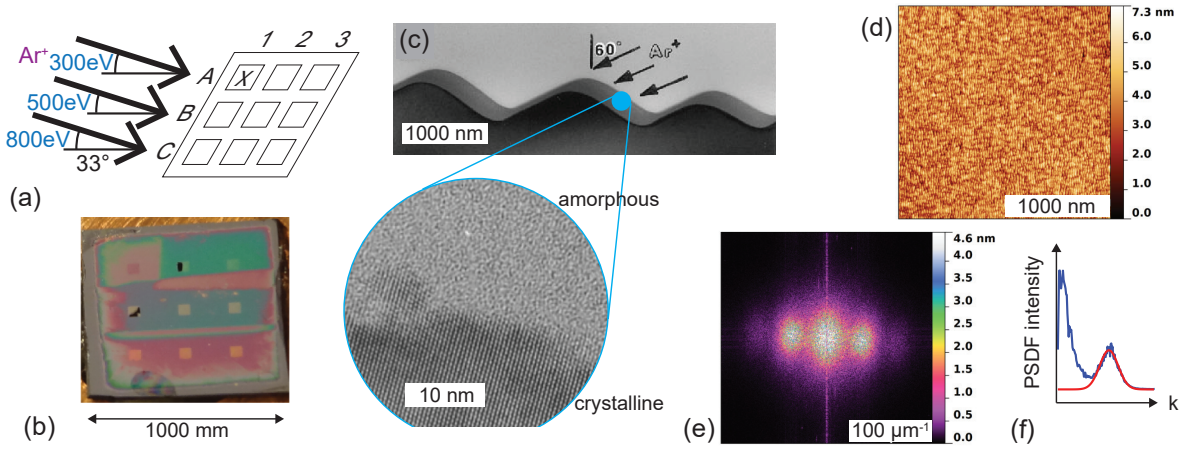

Figure 4.4.: Influence of Ar^+-ion milling. (a) A sketch of the treatment of all membranes on one wafer. The membrane marked by an x was shadowed during the ion bombardment. The rest was covered consecutively. (b) Optical picture of a wafer with 9 Si membranes of which 2 are broken. The color is determined by interference of white light. (c) Cross-sectional high resolution transmission electron microscope image of a Si surface sputtered with 50 keV Ar^+-ions and zoom (taken from [Chi03]). (d) $2 \times 2\,\mu$m-AFM image of the surface of a nanopatterned membrane. (e) The corresponding two dimensional Fourier transformation and (f) the PSDF, e.g. the autocorrelation function of (e).

of uncertainty in the thinning process. The layer thicknesses were determined by ellipsometry.

The subsequent nanopatterning of the surfaces of the individual Si membranes was done by Ar^+-ion erosion under an angle of 67°. The fluence was $1.0 \times 10^{17}/\mathrm{cm}^2$. Different batches were fabricated using different acceleration voltages of 300 V, 500 V, and 800 V. The other membranes on the respective wafers were masked by pure Si to prevent contamination by foreign atoms in the process. These low voltages were used to prevent too much erosion of the surfaces. This is schematically shown in Fig. 4.4(a) and (b). The cross-sectional transmission electron microscope image of a similarly structured Si surface is shown in Fig. 4.4(c). It was produced with a much higher acceleration voltage (50 kV), which leads to more intense patterns. The authors calculated for acceleration voltages similar to the ones used here a thickness of the amorphous top layer of about 3.5 nm [Chi03, Kel08]. Additionally, it was shown before, that for high temperatures $\leq 650\,°\mathrm{T}$, the surface should become crystalline instead [OI09]. It is worth to mention that only the front side underwent this treatment. The backside was not treated further after the HF-dip and should, therefore, have the same properties for all the samples.

The roughness of each membrane was measured by atomic force microscopy (AFM) on an area of $2 \times 2\,\mu\mathrm{m}^2$. Various different roughnesses on different length scales were obtained. On short length scales height variations are visible, while on longer length scales structured variations are visible, which are called ripples [Chi03]. This is shown in an exemplary AFM-picture in Fig. 4.4(d). To quantify the rippleness of the surface the power spectral density function (PSDF) is used. It can be described as the Fourier transformation (see Fig. 4.4(e) for the 2D Fourier transformation) of the spatial autocorrelation function and shows the intensity of the present wave vectors along

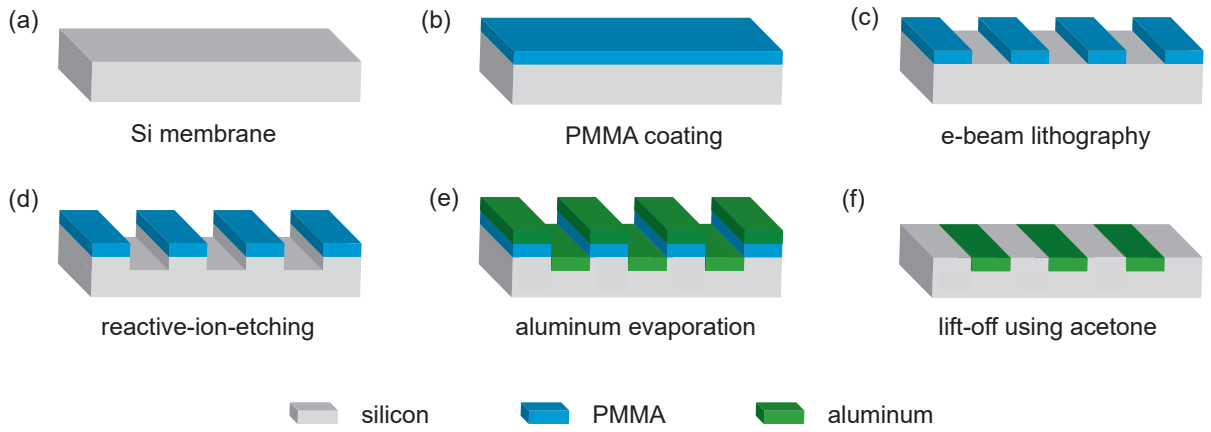

Figure 4.5.: Schematic of the grating fabrication using electron beam lithography.

the evaluated direction (see Fig. 4.4(f)). In general, a decay can be observed from lower to higher wave vectors. If the PSDF is evaluated perpendicular to the ripple pattern, additionally, a distinct peak is visible, whose wave vector belongs to the periodicity of the ripples. One finds that the ripples are oriented perpendicular to the ion beam irradiation direction, which is well understood for this patterning method.
It shall be noted that it is not straight forward to obtain a quantitatively comparable AFM picture on this small thickness scale. Details regarding the difficulties and solutions can be found in the thesis of Jan Haberland [Hab15].

4.2.3. Preparation of patterned Al structures

Bilayer membranes are prepared by evaporating or sputtering 10-40 nm Al on the front surface of the Si membrane. A preceding HF treatment removed the native oxide on the membranes surface, but the uncertainty of the different processes and fluctuations led to strong and weak adhered films.
Additionally, the Si membranes were nanopatterned with an Al grating to imprint distinct wave vectors on the generated spectrum. This is shown in Fig. 4.5: (a) the process was started by cleaning the samples, (b) spinning a thin layer of poly(methyl methacrylate) (PMMA) on top, and (c) the grating patterns were defined by electron beam lithography down with a period between 600 and 100 nm with a filling fraction of $\approx 50\,\%$. (d) After the development in methyl isobutyl ketone (MIBK) a short reactive-ion-etch with sulfur hexafluoride and oxygen was used to etch ≈ 3 nm nanometers into the material to improve the adhesion of (e) the evaporated 10-20 nm Al filling the grooves. (f) The residual Al on top of the PMMA and the PMMA itself was removed by a lift-off in acetone. This process yielded a very good reproducibility for large grating periods, while for small grating periods (< 100 nm) during the lift-off also the grating structure could detach. As the gratings were fabricated on the Si membranes it was easy to align them perpendicular to the [100]-direction, e.g. parallel to the membrane edges.
Further details regarding these processes can be found in the theses of Widmann and Ristow [Wid15, Ris16].

Chapter 5

Roughened silicon membranes

5.1. Introduction

Phonon dynamics in Si membranes are discussed in great detail in the literature [Tor04, Gro08, Bru11, Wai12b, Cuf13, Wan14, Sch15, Maz15, Neo15, Lia16]. However, it remains unclear where extrinsic attenuation crosses the intrinsic damping processes and governs the lifetimes of acoustic phonons. Two studies investigated the influence of the membrane's thickness on the lifetime and explained the extracted lifetime below the theoretical value with surface roughness of both surfaces [Cuf13, Maz15]. Cuffe et al. investigated the ground mode oscillation, while Maznev et al. investigated the central frequency of a short acoustic pulse generated by a short absorption length introduced due to a short laser wavelength. In these studies only one frequency was investigated per sample. However, it is important to measure a range of frequencies for one sample. With the 800 MHz laser setup it is not a straight forward process to measure lifetime above 1.2 ns. Bruchhausen et al. showed that this problem can be circumvented by performing a resonance measurement and detuning the laser cavity repetition rate to a subharmonic of the membrane's ground mode. These experiments are very tedious to conduct. Therefore, in this chapter a 82 MHz ASOPS setup from Laser Quantum is used to measure lifetimes up to 12 ns. The long time window allows to extract frequency- or more specific mode-dependent lifetimes very accurately and to study higher-order thickness resonances for up to eleven modes simultaneously in one sample. To tailor the roughness of the Si membranes without changing the other parameters in a non convenient way, noble gas ion bombardment is used. Roughnesses between 0.2 and 0.9 nm root mean square roughnesses are measured and investigated.

5.2. Surface characterization

The examined Si membranes are prepared as described in Section 4.2. A new - during this thesis - developed process consisting of a mixture of wet and dry etching is used.
In order to broaden the available acoustic frequency distribution every other membrane was thinned by ion beam milling with a flux of $1.2 \times 10^{17}/\mathrm{cm}^2$ at an acceleration voltage of 300 V [Kel08, OI09]. The ion beam treatments have been carried out with Ar^+-ions, which minimizes the implantation of ions into the Si membranes, contrary to the use of Ga^{2+}-ions in focused-ion-beam milling. This resulted in a thinning of about 15 nm which is considerably smaller than expected, based on similar experiments carried out previously. This may be due to the native oxide layer initially present at the membrane surface, but this is not further investigated.

For the nanopatterning of the surface layer after a similar bombarding earlier experiments found a thickness of the amorphous top layer of about 3.5 nm [Chi03, Kel08]. It was shown before, that for temperatures $\leq 650\,°\mathrm{T}$, the surface should become crystalline instead [OI09]. The sound velocity in amorphous Si is found to be $76.8 \pm 3\%$ of the corresponding directionally averaged crystalline speed [CS85], while the density only changes to a value $1.8 \pm 0.1\%$ less dense than crystalline Si [Cus94]. This is very similar to the values of SiO_2. Neogi et al. showed that due the removal of the native oxide (1 nm SiO_2) on each side of the membrane surface only the resonance frequency changes, but the lifetime stays the same [Neo15]. The influence of an amorphous layer on the lifetimes remains an open question. However, as amorphous Si and SiO_2 exhibit very similar acoustic properties, the influence of the amorphous layer on the lifetime is assumed to here to be low in comparison to the influence of the roughness. It should be mentioned that only the front side underwent this treatment. The backside was not treated further after the HF-dip and should, therefore, have the same properties for all the samples.

The roughness was measured as explained in Section 4.2 and in the thesis of Haberland [Hab15]. The following notation will be used throughout this section: N_δ denotes a non-pretreated sample with a root-mean-square-roughness of δ measured on an area of $2 \times 2\,\mu\mathrm{m}$. Different roughnesses are obtained on different length scales from 0.2 to 0.89 nm for 18 different samples. As a lower roughness example, the AFM measurement of sample $N_{2.5}$ is shown in Fig. 5.1(a). This is an untreated membrane with visible unordered height variations on short length scales. The

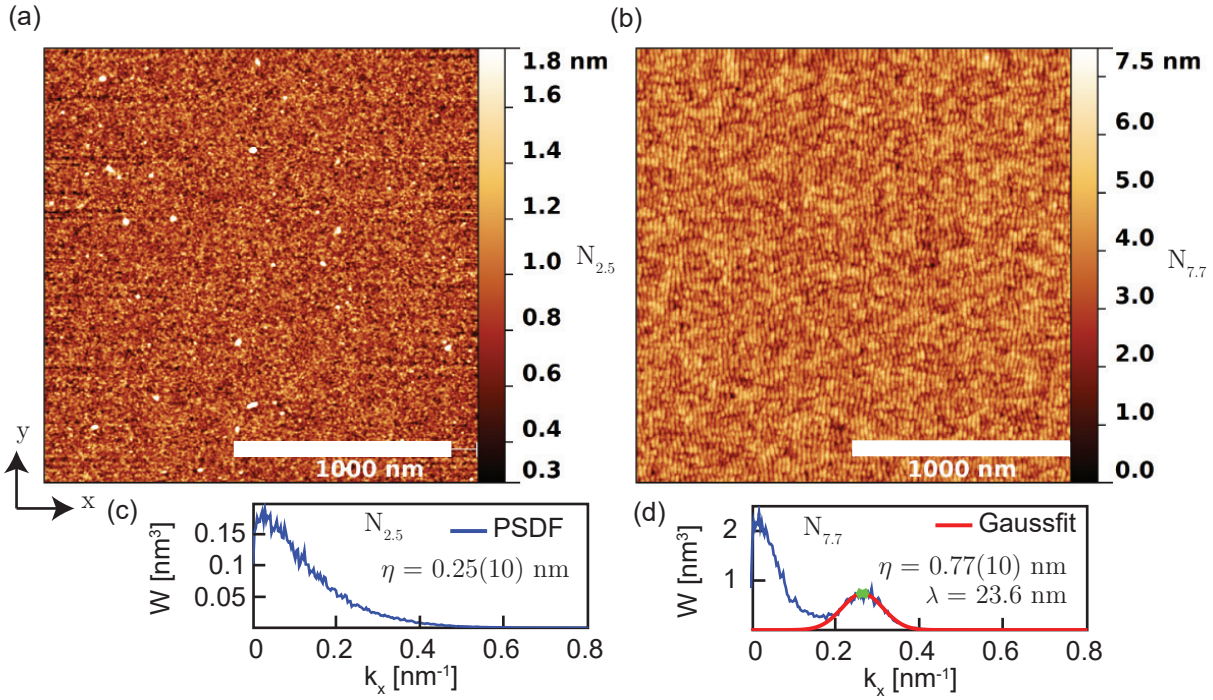

Figure 5.1.: AFM data for two different Si membrane surfaces. (a) untreated ($N_{2.5}$) and (b) bombarded with an Ar^+-ion beam under 67° and 300 V ($N_{7.7}$). (c) and (d): The corresponding power spectral density functions are evaluated along the x-direction, i.e. perpendicular to the line pattern visible in (b).

Table 5.1.: The properties of the produced samples N_δ, T_δ. T denotes the prior thinning process of half the samples. The thickness d is calculated from the ground mode frequency. The samples $N_{2.5}$ and $T_{2.0}$ did not undergo an ion bombardment. η denotes the root-mean-square-roughness, λ the peak of the power spectral density function.

	$N_{2.5}$	$N_{6.4}$	$N_{6.6}$	$N_{7.3}$	$N_{7.6}$	$N_{7.7}$	$N_{8.0}$	$N_{8.1}$	$N_{8.4}$
d (nm)	351	295	295	285	307	321	290	324	312
η (Å)	2.5	6.4	6.6	7.3	7.6	7.7	8.0	8.1	8.4
λ (nm)	∞	40	30	36	28	24	53	24	30
Ion Voltage (V)	0	800	500	800	500	300	800	300	500
# (modes)	5	2	4	2	2	2	2	4	4
	$T_{2.0}$	$T_{4.8}$	$T_{5.0}$	$T_{5.2}$	$T_{5.5}$	$T_{5.7}$	$T_{6.3}$	$T_{6.7}$	$T_{8.9}$
d (nm)	337	339	297	323	297	293	321	317	310
η (Å)	2.0	4.8	5.0	5.2	5.5	5.7	6.3	6.7	8.9
λ (nm)	∞	42	30	58	27	31	26	79	30
Ion Voltage (V)	0	800	500	800	500	500	300	800	300
# (modes)	11	2	4	2	3	3	4	2	4

amplitude of the features goes up to 1.8 nm with $\delta = 0.25(10)$ nm. The corresponding power spectral density function (PSDF) evaluated along the x-axis is shown in Fig. 5.1(c). A decay is observed from lower to higher wave vectors, however no specific correlation at a given wave vector is apparent.
Different to Fig. 5.1(a), as a comparison, an AFM measurement of a membrane with a large roughness is shown in Fig. 5.1(b). The membrane was treated with an Ar^+-ion beam under 67° angle of incidence and 300 V. The root-mean-square-roughness is 0.77(10) nm with height features up to 7.5 nm, as reflected in the nomenclature: $N_{7.7}$. In the AFM image an ordered structure emerges, which resembles a vertical stripe pattern [Chi03]. This becomes more apparent in the PSDF spectrum evaluated perpendicular to the stripes, where a distinct peak is visible which corresponds to the wavevector of the ripple pattern. The ripples are oriented perpendicular to the ion beam irradiation direction, which is well understood for this patterning method [Kel08, OI09]. An overview including further sample parameters is given in Table 5.1

5.3. Experimental results

The phonon lifetimes are determined by an optical pump-probe setup from Laser Quantum, where measurements were performed by myself in their development laboratories in Konstanz. Two 82.3 MHz GECCO^{TM} Ti:sapphire lasers from Laser Quantum are working in an asynchronous optical sampling scheme [Bar07]. This means both lasers have a slight repetition rate offset of 0.3 to 2 kHz, which leads to a consecutively ramped time delay between both laser pulses from 0 up to 12.5 ns. The pulses have a central wavelength of 800 nm and a bandwidth of < 40 nm. In order to start the measurement a two-photon generation process in a BBO crystal focused on a 125 MHz-bandwidth Si-photodiode was used as trigger signal. The pump was focused via a 100 mm lens on the sample with 70 mW power, while the probe was focused using a 35 nm lens and 30 mW power (spot size < 30 µm). The probe light was detected with another 125 MHz-bandwidth Si-photodiode. To reduce the influence of the individual laser pulses a 22 MHz electrical short pass was used behind the photodiode. The excitation is explained in

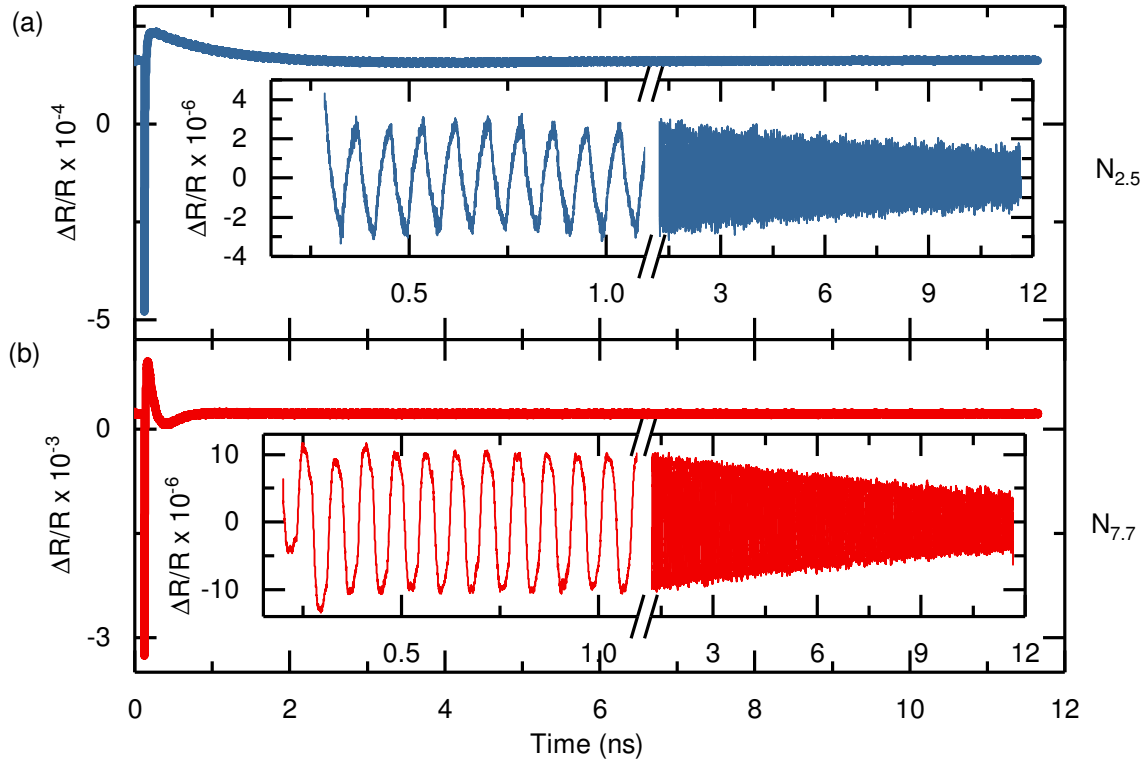

Figure 5.2.: Experimental temporal reflectivity data of the same membranes as shown in Fig. 5.1 in the case of (a) untreated and (b) treated. In the insets the acoustic signal without electronic background is shown.

Section 3.2 and the interferometric detection is explained in Section 3.7. The signal-to-noise-ratio was maximized by tuning the probe wavelength to a position where the reflectivity change due to the membrane oscillation is strongest. Due to the large spectral bandwidth of the laser pulses the tuning to a specific spectral range was done with an optical bandpass filter in front of the photodiode. Experimentally this was accomplished by trying different filters in front of the photodiode and turning the filter by hand to an angle, where the highest intensity change was observed in the real time measurement. Details regarding the setup can be found in the bachelor thesis of Stritt [Str15].

In Fig. 5.2(a) and (b) the obtained time domain data for the two samples ($N_{2.5}$ and $N_{7.7}$) are shown. Regarding the detected spectrum, for sample $N_{7.7}$ in front of the detector an optical bandpass centered at 820 nm and tilted under an angle of 20° is used, while for the sample A2 an optical bandpass centered at 800 nm and tilted at 30° is used. The reflectivity signal shows a sharp rise and relaxation in the beginning of the time window. Superposed on this transient are oscillations over the whole time window. These are extracted from the decaying background by a triple exponential fit and shown in the insets. A decay of the oscillations with time can be seen on longer timescales. The oscillations look slightly different for both membranes, which becomes even more apparent upon comparison of the FFT spectra. The sample $N_{2.5}$ shows a zic-zac like pattern in the beginning and a decay of the total amplitude over the 12 ns time window of 60 %. At the end of the oscillation the zic-zac features are not visible anymore and a

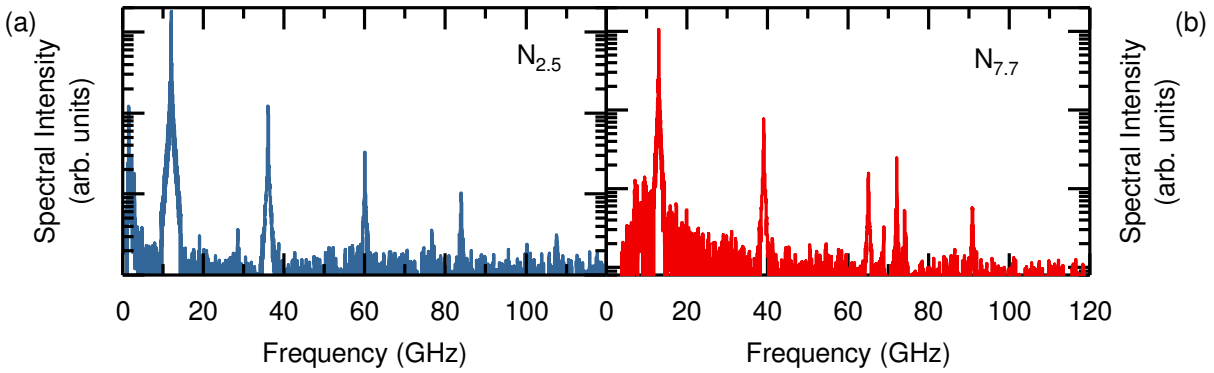

Figure 5.3.: Fourier transformations of the transients of the two samples (a) $N_{2.5}$ and (b) $N_{7.7}$.

sine-like behavior emerges. The sample $N_{7.7}$ has less sharp saw-tooth features and an amplitude decay of 60 % over 12 ns as well. This hints at the faster damping of higher frequencies compared to low frequencies.

In the Fourier transformation of the time domain signal of sample $N_{2.5}$ (see Fig 5.3(a)) 4 equidistant peaks become visible. The first one, called fundamental mode, is at $f_1 = 12\,\mathrm{GHz}$ and the higher harmonics are at odd multiples of this. This behavior is predicted for a homogeneously excited membrane (Section 2.4). The frequency is given by: $f_n = nv_\mathrm{L}/2d$, where n is the mode number and only odd modes are present due to the symmetry, v_L is the longitudinal speed of sound and d is the thickness of the membrane. With the literature value of $v_\mathrm{L} = 8433\,\mathrm{m/s}$ a thickness of $d_{2.5} = 351\,\mathrm{nm}$ is obtained, which corresponds well to the value of 350 nm given by the manufacturer and which was checked by ellipsometrical measurements. The higher harmonics have a smaller amplitude, which is expected from the theory in the case of a homogeneous excitation throughout the membrane. In fact a $1/n$-decay of the n-th mode amplitude is expected due to the excitation and detection processes. This is explained in detail in the thesis of Klingele [Kli13].

The spectrum of sample $N_{7.7}$ (see Fig 5.3(b)) looks similar but the peaks are shifted to higher frequencies with a fundamental mode frequency of 12.8 GHz and higher order modes at odd multiples of this value. The thickness of the membrane is calculated to be $d_{7.7} = 329\,\mathrm{nm}$ and thus $\approx 20\,\mathrm{nm}$ of Si have been removed due to the Ar^+-ion patterning. This value is different from the milling value at zero degree. Here an important conclusion can be made: The overall acoustic spectrum does not change after the ion pattering. This allows the comparison of different roughnesses and their influence on the respective mode lifetimes. The additional mode at 74 GHz is an artifact of the measurement system and the non-perfect adjustment in the electronics for the frequency offset between both lasers.

Higher acceleration voltages should lead to a thicker layer of the amorphous Si. This seems to weaken the optical detection quality, as only membranes bombarded with Ar^+-ions at 800 V show at most two detectable modes. This is attributed to the reduced signal-to-noise ratio of these measurements.

5.4. Evaluation of the lifetimes

Contrary to previous experiments [Dal09, Bru11, Cuf13, Maz15] the lifetime determination can be done not only for the fundamental mode, but also for the higher harmonics (up 263 GHz) in one measurement. The determination of mode lifetimes in the case of multiple oscillatory superpositions is non-trivial. Therefore the applied method is explained in the following.
In the frequency space, a frequency range of $f_n \pm 5\,\mathrm{GHz}$, centered around the individual modes, is Fourier-transformed back to the time domain and a $A_n \cdot \sin(2\pi f_n t + \phi_n)$-fit is performed to obtain the single mode signal. By shifting the center frequency from the fundamental mode to the higher harmonics, a fit can be made for all measured frequencies. The advantage of this procedure is that the lower-frequency noise can be reduced and contributions from other harmonics do not influence the fit. This comes at the cost of additional artifacts/ringing from the two Fourier transformations arising at the edges of the signal. However, the artifact allows to check the quality of the method – a small artifact at the end of the back transformed time data compared to the beginning part suggests a good results. The quality of the fit is checked by subtracting the superposed fitted sines from the experimental data and evaluating the residual. Lifetimes ranging from the upper limit of 12 down to 0.1 ns are extracted for frequencies ranging from 12 to 263 GHz.
In Fig. 5.4 the evaluated lifetimes for the distinct frequencies of the eighteen different membranes are shown. To get a better insight in the damping behavior these results are compared to different theoretical models derived in Section 2.7.1. The data are plotted as well in Fig. 5.4. One sees

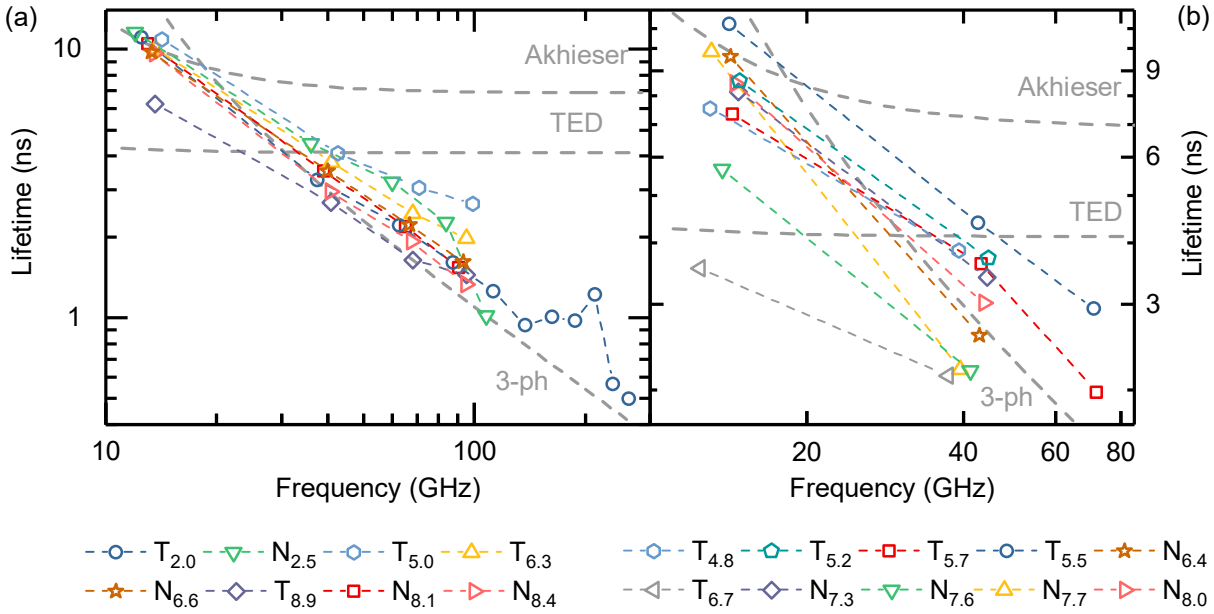

Figure 5.4.: The evaluated lifetimes of the different harmonics and their frequencies for all samples are plotted for more than three frequencies. (a) shows the results where more than 3 frequencies could be measured. (b) shows the results of the samples with less than 3 frequencies. The gray dashed lines correspond to the lifetime limits given by Akhieser, thermoelastic damping (TED), and 3-phonon-decay (3-ph).

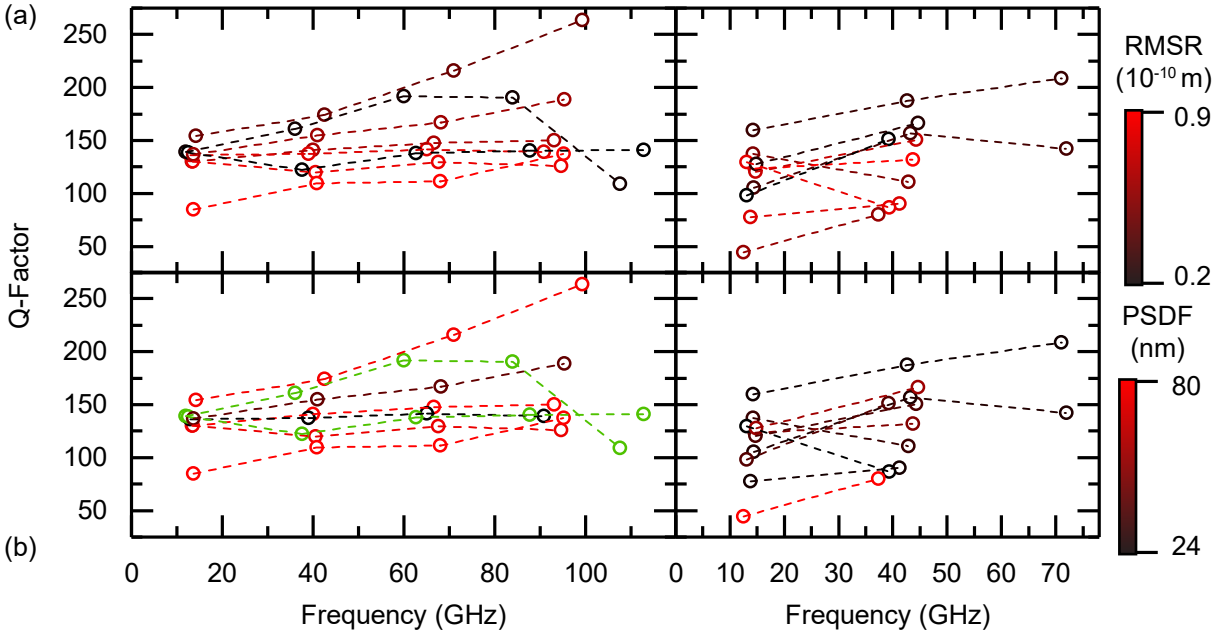

Figure 5.5.: (a) The evaluated Q-factors of all measured modes are plotted compared to the root-mean-square-roughness. (b) The evaluated Q-factors are plotted compared to the peak of the power spectral density function. A black circle denotes the least RMSR or PSDF-value, while a red circle denotes the highest value. The green circles belong to the untreated samples without any structuring.

that the lifetimes extracted in these measurements are not limited by Akhieser damping nor surface boundary roughness scattering, but they seem to be governed by thermoelastic damping (TED) and three phonon decay processes (3-ph). A comparison to values found in the literature is given in the Appendix.
The lifetime values are also compared to the surface roughness. For a better visibility the Q-factor is used instead of the lifetime. The Q-factor is defined as $Q = \omega\tau$, which is a good choice, as the measured lifetimes exhibit roughly a $\tau \approx \omega^{-1}$ behavior. In Fig.5.5(a) the Q-factor is plotted for all frequencies and the RMSR ist color coded, where black encodes a low RMSR and red denotes a large RMSR. Q-factors from 50 to 250 are extracted with a span of up to 100 for the different harmonics in one membrane. While the spread is quite large, it is clearly visible that a lower RMSR donates a higher Q-factor. In Fig.5.5(b) the color code symbolizes the peak value of the power spectral density function. The green circles are showing the modes of the non-structured samples. Within the variation of the Q-factor no clear trend with the PSDF can be seen.

5.5. Inhomogeneous broadening

The roughness will give rise to an inhomogeneous broadening. Due to the different thicknesses of the membrane on a small scale, the fundamental frequency will differ spatially. The AFM-measurements show the topography of the membranes quite well and by assuming every surface

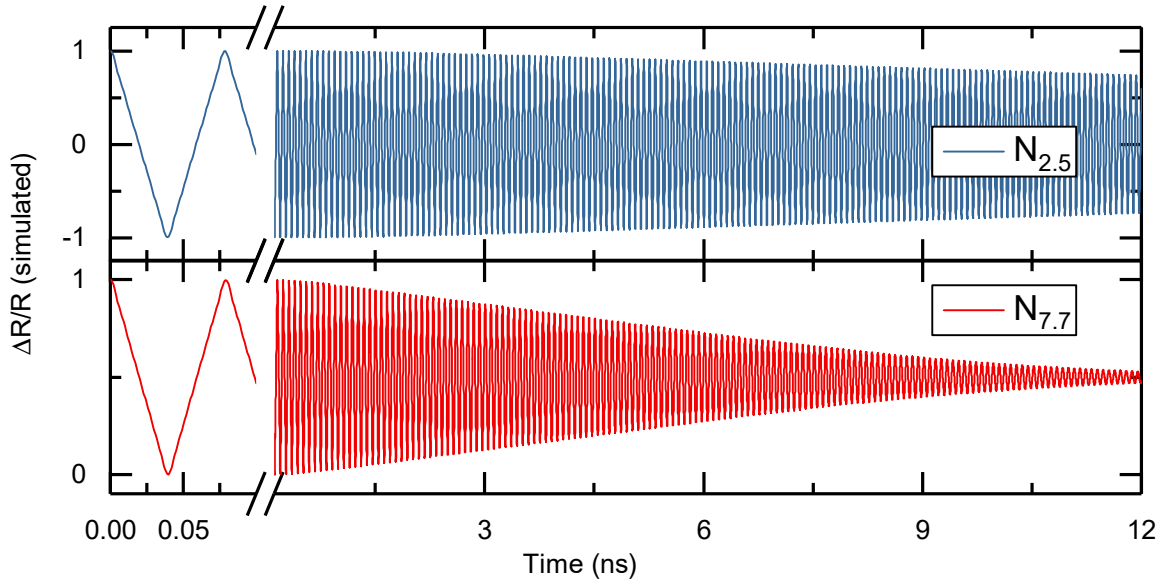

Figure 5.6.: Simulated thickness oscillation of the two different AFM measurement fields (effects through inhomogeneous broadening). (a) Simulation of $N_{2.5}$ and (b) $N_{7.7}$

point to be a single membrane, one can simulate the detected signal by the super position of all single membranes at every pixel. It shall be noted that in the experiment the optical detection averages over the laser spot size, which, additionally, is also diffraction limited: No individual pixels could be resolved. A membrane with $d = 330\,\text{nm}$ thickness is assumed to which the AFM height topology (with 512×512 pixels) of the samples $N_{2.5}$ and $T_{N.7}$ is added. The bottom surface is assumed to be atomically flat. Surface oxidation has been completely omitted. The measurement is simulated by assuming the detected signal $M_i(t)$ for every pixel:

$$M_i(t) = \sum_{n=1}^{9} \frac{1}{n} \sin\left(\frac{n\pi t v_\text{L}}{d + \delta_i}\right) \tag{5.1}$$

with n being the odd mode number and v_L the longitudinal speed of sound. By averaging all simulated measurements M_i, the simulation for inhomogeneous broadening can be obtained.
In Figure 5.6 the results for two topographies are shown. The results of the simulation of sample $N_{2.5}$ show a slower temporal decay than the one measured. In that case the lifetime measurement is not limited by inhomogeneous broadening. For the sample $N_{7.7}$, however, the amplitude decay given by inhomogeneous broadening is larger than the experimentally measured one. This stems from two weak assumptions in the simulation: i) the laser can detect each pixel individually and ii) the surface atoms are not connected to each other. By averaging over surrounding thicknesses, the error might be reduced. Neighboring atoms should keep neighboring atoms in phase. This will be simulated by a moving average algorithm in two dimensions. This means the convolution of a rectangular window with the set of data – the arithmetic mean around the assessed point. A window with the value of ± 6 pixels in x and y direction yields an amplitude decay due to inhomogeneous broadening comparable to the measured decay. A theoretical averaging over 50 nm occurs, which is well below the diffraction limit. It shall be noted that the obtained decay

is not purely exponential anymore, but exhibits a drop-shape like decay due to the beat of the different frequencies.
It can be concluded that this simple model is not sufficient, as the binding forces and the detection are only assumed to smoothen surface and, thus, the frequencies. A more detailed approach would be necessary. For example, the roughness could be assumed to lead to a change in mass-loading of the surface.

5.6. Conclusion

In conclusion, the influence of surface roughness on the lifetimes of coherent acoustic phonons is studied in free standing Si membranes. Therefore, Si membranes are prepared with different roughnesses. The roughness can be divided into roughness features on the atomic scale ranging from 0.2 to 0.89 nm and waviness, which is determined by variations of a perfect surface on a larger lateral scale, e.g. a small changing slope of the surface with wavelengths between 24 and 80 nm. An 80 MHz asynchronous optical sampling setup was employed to measure frequencies from 12 up to 263 GHz and corresponding lifetimes from 12 down to 0.1 ns. These measurements and results show that the so far assumed influence of surface roughness on phonon lifetimes in Si is not as strong as expected. All the lifetimes resemble a $1/\omega$-decay. In fact only a very weak influence was observed in the investigated range. With increase of the roughness changes by a factor of 4 the Q-factor shrinks by a factor of 2. This is only just above the variation of the Q-factor within one membrane.
This was the first measurement using multiple acoustic eigenmodes of the membrane to characterize frequency-dependent phonon lifetimes. The theory for boundary scattering proposes a non-negligible influence above 200 GHz. The measurement of higher frequencies could be done by pumping with a lower wavelength, which would lead in turn to a short acoustic pulse and, thus, high frequency components – i.e. of 270 GHz for a wavelength of 400 nm [Maz15].
To separate intrinsic from extrinsic dissipation processes in the Si membranes, the measurement should be redone at different temperatures. This would result in a change of the intrinsic decay processes, as the population of thermal phonons will change. The boundary scattering, however, will not be influenced.

Chapter 6

Characterization of bilayer membranes

6.1. Introduction

In this chapter a bilayer system consisting of polycrystalline Al on crystalline Si is investigated. This system exhibits some remarkable properties. The impedances are close to each other to allow for a good transmission of phonons at the interface. However, the optical properties are very different. The high optical absorption in the Al allows for the intense generation of coherent acoustic phonons. By making the Al film thin enough, very high acoustic frequencies can be generated and a broad spectrum is achieved. This huge spectrum allows to investigate the variation of material properties of the bilayer with in dependence of the frequency. Additionally the different optical properties allow for a strong asymmetric detection. By evaluating the pulses generated in the Al film and in the Si, the relative generated stress amplitudes can be extracted. The pulses exhibit the structure of a pulse train, resembling a frequency comb in the frequency domain. *Optical* frequency combs became an important tool since the development 20 years ago for distinct frequency measurements, for example for chemical detectors due to the fixed frequency lines, LIDAR (light detection and ranging) due to the precise measurements of Doppler shifts and in telecommunications due to the heightened sensitivity.
One expects *phononic* frequency combs to fulfill similar accomplishments. In the presented measurements, the frequency comb allows to define a very sensitive measurement for the impedance mismatch between both layers and for the ratio of the propagation times in both layers. Additionally by comparing the individual pulses of the pulse train, the spectral amplitude decay can be measured very precise. In the case of perfect adhesion the direct comparison yields the frequency dependent phonon-lifetime. For weaker adhered sample with the use of a modeled spring coupling between both layers, adhesion and attenuation values can be extracted quantitatively.

6.2. Perfect adhesion

In this section acoustic frequency combs are optically excited and detected in bilayer systems consisting of Si membranes covered with perfectly adhered thin Al layers. The thickness of the Al ranges from 40 down to 10 nm, which allows to measure frequencies from 10 up to 500 GHz. Depending on the eigenmodes of the system this corresponds to frequency combs with 11 up to 45 modes. The different thicknesses of the Al films allow for shadowing the Si membranes in a very

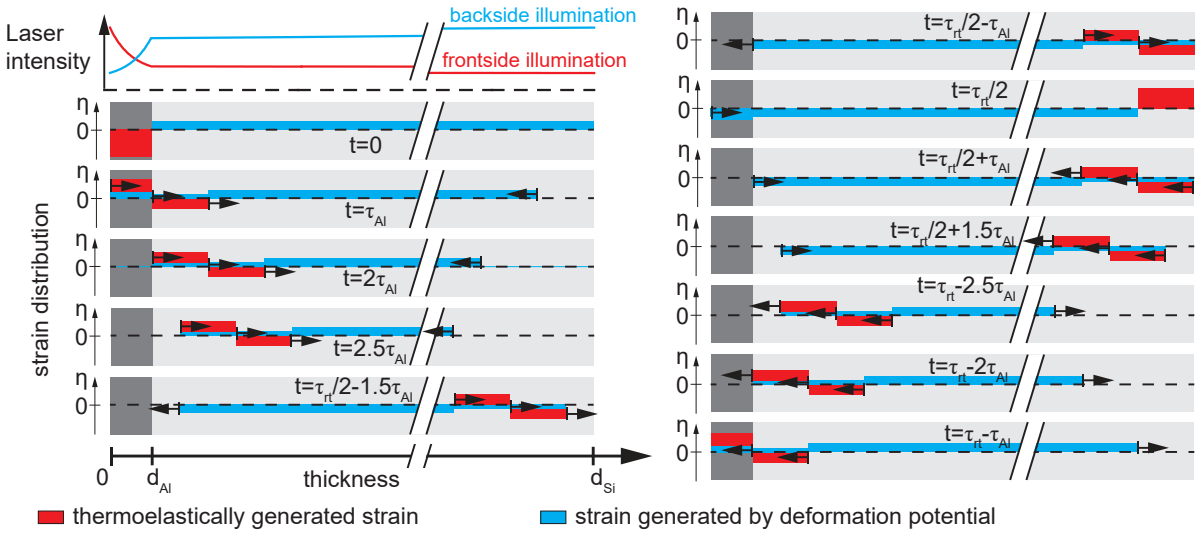

Figure 6.1.: Sketch of the laser intensity and illustration of the initial strain distribution and subsequent evolution in the sample. On the top left the spatial intensity of pump and probe is plotted for front side and backside illumination. Below, the initial case ($t = 0$) of the bilayer excited by front illumination is shown. The initial generated acoustic strain by thermoelastic excitation in the Al (red) and by deformation potential in the Si (blue) is shown. Additional strain distributions at relevant time steps after excitation are shown. The arrows indicate the propagation direction of the various strain fronts. Details are given in the text.

controlled way. This facilitates changing the contribution of contractive stress by deformation potential in Si to the expansive stress by thermoelasticity in the Al over a broad range. In the time domain the frequency comb corresponds to quasi-regularly separated pulses, where the spacing is given by the round trip time of the acoustic cavity given by the bilayer system. The comparison of the individual reflected pulses, i.e. their respective Fourier transformations, allows for the precise extraction of frequency dependent lifetimes over the whole pulse spectrum.

6.2.1. Sample description

In Fig. 6.1 the bilayer sample structure is shown. It consists of a crystalline Si membrane and different thick Al films. The fabrication process is explained in detail in Section 4.2. In the scope of this thesis adhesion promoters were tested. Therefore, one of the investigated membranes was reactive-ion-etched with sulfur hexafluoride and oxygen before Al deposition. This resulted in three $d_{\mathrm{Si}} = 350\,\mathrm{nm}$ thick membranes and one $d_{\mathrm{Si}} = 328\,\mathrm{nm}$ thick membrane. Although the fabrication process was replicated, it was not possible to forecast the outcome adhesion-wise. This allows to discuss the cases of perfect adhesion in this section and weak adhesion in Section 6.3 individually. Four different perfectly adhered samples were fabricated with the thicknesses of $10 \pm 1\,\mathrm{nm}$, $23 \pm 1\,\mathrm{nm}$ and $40 \pm 4\,\mathrm{nm}$ in a sputtering process on the thick membranes and a $d_{\mathrm{Al}} = 17 \pm 1\,\mathrm{nm}$-thick Al film on top of the thinner membrane. The thickness of the membrane was measured optically by ellipsometry and the thickness of the Al film was

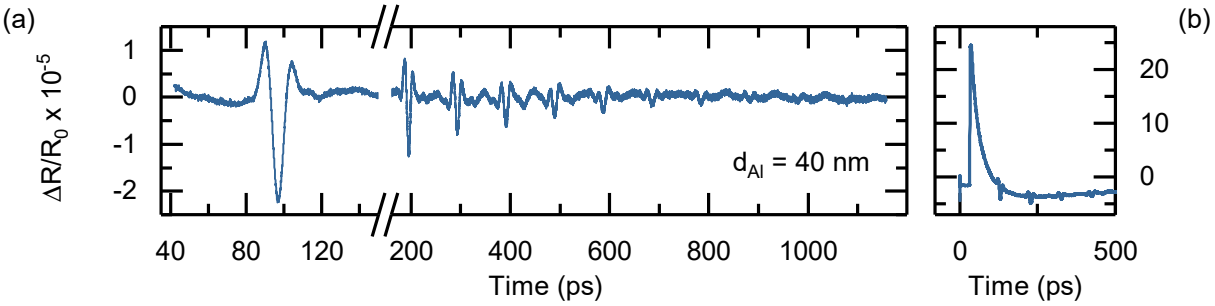

Figure 6.2.: (a) Time-resolved modulation of the reflected probe beam $\Delta R/R_0$ without electronic background (shown in (b)). The Si membrane is 350 nm thick and the Al film 40 nm.

measured mechanically by a quartz crystal during evaporation and atomic force microscopy after deposition. All thicknesses were remeasured acoustically in the pump-probe experiments. The pump power was 20 mW at a wavelength of 790 nm and the probe laser power was 3.5 mW at a wavelength of 820 nm. The spot sizes were below 2 µm. The refractive indices and absorption coefficients of Si and Al are given in Table A.1. 78 % of the incident light is transmitted in the Al, where 95 % (73 %) is absorbed in the 40 nm (10 nm) Al film. Most of the residual light is transmitted into the Si, in which 4 % of the residual light is homogeneously absorbed.
The physical processes following the pumps excitation are explained in Section 3.2. Here, the results are discussed qualitatively. In Fig. 6.1 the strain generated in Al by thermoelasticity (TE) and the strain generated in Si by deformation potential (DP) upon front illumination are shown. Nearly homogeneous strain is visible in both layers, but due to the high absorption of the Al, more strain will be generated in the Al. The difference is largest for the thickest Al film and weakest for the thinnest Al film. But the thickness also has an impact on the detection. Depending on the thickness, i.e. the absorption of the probe in the Al, the detection is governed by the photoelastic effect in thick films and by a dynamic Fabry-Pérot like effect in thin films. This is due to the fact that the light from the backside is able to propagate through the Al film and to interfere with the initially reflect light. The following sections are divided accordingly, where the effects will be explained in more detail.

6.2.2. Experimental results

6.2.3. Thermoelastic excitation in thick Al layers

First, the sample with the thickest Al film will be discussed, where the influence of the DP can be neglected because 99 % of the entering pump light is absorbed in the d_{Al}=40 nm thick Al layer. Additionally, nearly no light enters the Si, which leads to the assumption of purely photoelastic detection in the Al film. In Figure 6.2(a) the extracted time trace of the measured signal without the electronic background (shown in Fig. 6.2(b)) is visible. At 98 ps a tripolar pulse is apparent, which repeats with weaker amplitude, slowly changing amplitudes, and additional oscillatory components at multiples of that time resulting in equidistant spaced pulses. The amplitude decay of the repeating pulses is exponentially.
The tripolar pulse shape exhibits a characteristic shape of two maxima and a minimum in

between. Each feature can be identified with the detection of a separate strain front. The first strain front (leading to the first maximum) is generated at the Al/Si interface and is emitted directly into the Si membrane. The second strain front (leading to the minimum) is generated at the Al-air surface and enters the Si with a time delay relative to the first one given by the propagation of the front once through the Al film: $\tau_{\mathrm{Al}} = d_{\mathrm{Al}}/v_{\mathrm{Al}}$, where v_{Al} is the longitudinal speed of sound in Al. The third strain front (leading to the latter maximum) is generated together with the first front but propagates in the Al instead and is emitted into the Si only after one round trip in the Al with an additional delay of $2\tau_{\mathrm{Al}}$ relative to the first strain front. The initial configuration after excitation (at $t = 0$) and the evolution in time $t > 0$ of these fronts is schematically shown in Fig. 6.1 as red strain. After τ_{Al} a bipolar strain pulse emerges with the above mentioned strain fronts. After one round trip the strain pulse incident on the Al film is detected photoelastically, which in first approximation of Eq. (3.25) means the integral of the strain, a tripolar reflectivity change, is detected.
From the quantitative amplitudes of the measured extrema one can corroborate these assumptions. The relative amplitudes of the first pulse in Fig. 6.2 are 1, -2 and $1 - \epsilon$ for the first maximum, the minimum, and the latter maximum, respectively. This corresponds directly to the three separate strain fronts generated by TE in the Al as can be seen in Fig. 6.1. In this simple picture the two maxima should have the same amplitudes, but as the latter strain front passes once through the Al, heat conduction will soften its amplitude (for the influence of heat conduction see Sec. 3.4) by a factor ϵ, leading to the measured asymmetry. Furthermore the slight difference in impedance between Al and Si leads to a reflection of 7 % at the interface (for reflection coefficients at interfaces see 2.5). This adds the trailing oscillatory part after the main pulse upon transmission in the Si and the preceding part before the main pulse upon transmission in the Al as can be seen in the measurement.
Considering the measured thicknesses and the respective speed of sounds it is straightforward to calculate the round trip time of the acoustic cavity established by the bilayer system between the Al/air-surface and the Si/air-surface. With the temporal length of the membrane $\tau_{\mathrm{Si}} = d_{\mathrm{Si}}/v_{\mathrm{Si}}$, where v_{Si} is the longitudinal speed of sound in Si, one obtains for the round trip time $\tau_{\mathrm{RT}} = 2(\tau_{Al} + \tau_{Si}) = 97.6\,\mathrm{ps}$. This is in very good agreement with the experimentally observed value of 98 ps.

6.2.4. Excitation through deformation potential for thin Al layers

In this section two samples are discussed where the Al film is thin enough to let pump light excite the Si, but not thin enough to let probe light reflected from the Si/air-surface pass the Al film. Therefore, the effect of the strain excited by DP can not be neglected anymore. The Al films are 23 and 17 nm thick and absorb 95 and 89 % of the entering light, respectively. In Fig. 6.3(a) and (b) the extracted time traces of the measured signals without the electronic background for both samples are shown. Each trace consists of two equidistant pulse trains: i) one appearing at 45.5 ps (41.5 ps) with the unipolar shape of a single minimum and ii) a tripolar pulse with two maxima and a minimum in between appearing first at 91.1 ps (83.0 ps) with a tripolar pulse shape. A zoom-in of the larger and later pulse is shown in the insets. The pulses decay exponentially in amplitude over time and with every repetition new front and back oscillatory components are acquired.
First, the tripolar pulse will be discussed. It looks very similar to the measured pulse of the 40 nm Al film above, where only the influence of TE generation was important. But, by comparing the

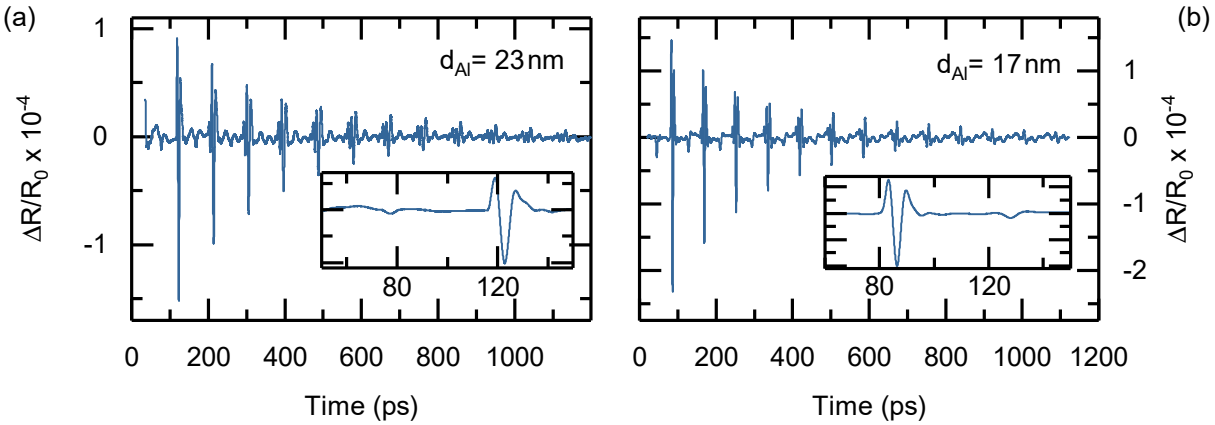

Figure 6.3.: Influence of the deformation potential. (a) Time-resolved modulation of the reflected probe beam $\Delta R/R_0$ without electronic background of the 350 nm Si membrane with 23 nm Al on top. (b) Si membrane with a thickness of 328 nm with 17 nm Al on top.

amplitudes of the relative maxima (relative to the amplitude of the minimum) in detail it shows that the relative maxima are larger here: The relative amplitudes of the three extrema of the detected pulses become $(1+\mu)$, (-2), $(1+\mu-\epsilon)$, with µ as a factor quantifying the influence of the DP strain. This is apparent in Fig. 6.1, where one can see that at the presence of the first and third TE strain front in the Al film the DP strain front (blue) is also present and is leading to a larger signal. It shall be noted that the earlier detection of the tripolar pulse compared to the 40 nm sample matches the shorter cavity length due to the thinner Al films.
However, the largest change of the transient due to DP is in between the tripolar pulses, where the negative unipolar pulse is apparent. It corresponds to the detection of the strain fronts generated at Si/air-surface by the DP with the relative amplitude of µ compared to the TE strain. This is shown in Fig. 6.1, where after half the round trip time the strain fronts are detected in the Al layer. As the strain does not change signs, the signal is just an unipolar dip. From the sketch it is straightforward to extract the relative amplitude µ from the measurement. The comparison of the minima of the consecutive unipolar and tripolar pulses gives $\mu \approx 0.076$ for the 23 nm sample and $\mu \approx 0.130$ for the 17 nm sample. This is on accordance with the assumption that a thinner Al film absorbs less light and the Si will be more excited, leading to a larger µ for the thinner film.

6.2.5. Detection by dynamic Fabry-Pérot interference

So far photoelastic detection of TE and DP strain was discussed. Here, the additional process of interferometric detection is considered. There are two simple schemes to favor this detection mechanism: i) one is making the Al film thin enough to let light reflected light from both surfaces of the bilayer interfere on the detector or ii) the other is changing the direction of detection, i.e. probing the bilayer system from the Si/air-surface, upon which the light reflected at the Al/Si-interface and the Si/air-surface interferes on the detector.
First, the backside illumination is discussed. To make sure no light from the Al/air-surface is incident on the detector the 40 nm Al film sample was chosen and pump and probe were

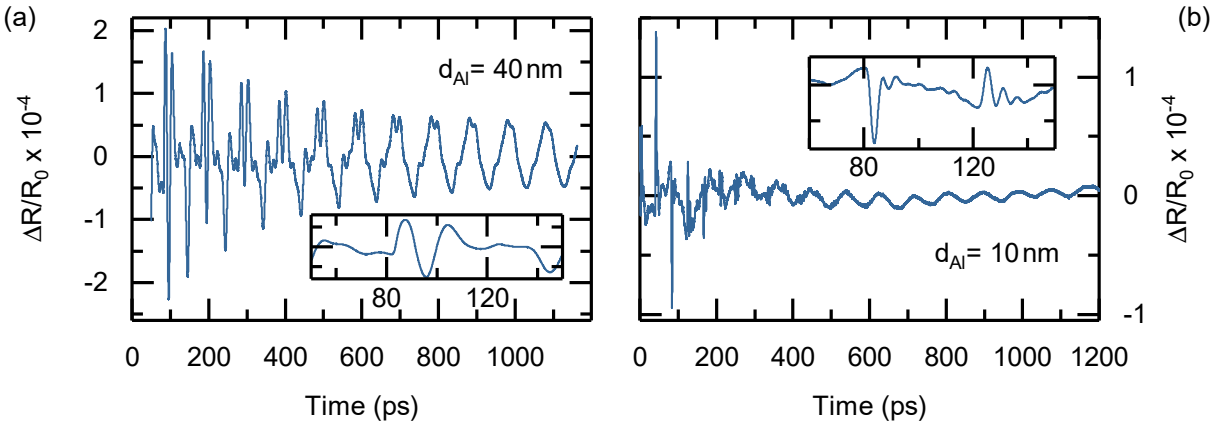

Figure 6.4.: Influence of the detection scheme. (a) Time-resolved modulation of the reflected probe beam $\Delta R/R_0$ without electronic background of the 350 nm Si membrane with 40 nm Al on top measured from the backside. A close up of the first pulse is shown in the inset. (b) Time-resolved modulation of the reflected probe beam $\Delta R/R_0$ without electronic background of the 328 nm Si membrane with 10 nm Al on top measured from the top. A close up of the first pulse is shown in the inset.

incident from the backside. The light intensity is shown schematically in Fig 6.1. Before the pump reaches the Al around 4 % of the intensity is absorbed in the Si leading to DP strain. The rest is absorbed in the Al and generates TE strain.

In Figure 6.4(a) the extracted time trace of the measured signal without the electronic background is shown. Similar to above, were TE and DP strain were present unipolar and tripolar pulses are visible, the unipolar one appearing first at 50 ps and the tripolar one at 100 ps. Furthermore, a strong oscillation at the end of the measurement is visible. In contrast to the other measurements the minima of unipolar and tripolar pulses have the similar amplitudes, which leads to a relative strain of $\mu \approx 0.9$. While the tripolar pulse dampens equally exponentially as in the front side measurement, the slow oscillation is visible over the whole transient. This is due to the weak attenuation at lower frequencies (see Section 2.7.1 and Section 6.3) and also the increased sensitivity of this detection method to the ground mode frequency.

Hudert et al. showed that the photoelastic contribution to the detection in Si membranes is very small compared to the interference detection given by the acoustic cavity [Hud09]. They showed that the moving strain inside the membrane leads to a linear elongation and compression of the end surfaces, a dynamic Fabry-Pérot cavitiy. This is also discussed in the previous Section 5 discussing roughened membranes. The interferometric method is also sensitive on the strain inside the membrane (see Fig. 6.1) as the integral over the whole strain leads to a elongation or compression of the whole system. Therefore, the slow frequency component leading to the unipolar dip in the beginning of the transients is steady over the whole transient, while higher frequency components get dampened faster and only the linear elongation and compression survives. Additionally, the highest frequency components after excitation are present in the short bipolar pulse generated by TE strain. The short pulse does not change the total strain in the membrane while propagating inside the membrane, but can only be detected at the surfaces, where the detection is enhanced on one side due to photoelastic detection in the Al film.

Thus, a method of further reducing the photoelastic contribution is used. The sample is pumped from the thin 10 nm Al film side. The Al absorbs about 74 % of the entering pump light, while the rest enters the Si membrane and also reflected probe light from the backside is still able to be measured. The somehow transparency of the Al film suppresses the photoelastic detection and favors interferometric detection between the air-surfaces of the bilayer system. A positive effect of the thin film is the short length of the TE strain pulse, which leads to very high frequency components. In Fig. 6.4(b) the extracted time trace of the measured signal without the electronic background is shown. In the beginning of the transient alternating unipolar maxima (first at 41.5 ps) and minima (first at 83.0 ps) can be seen, while at later times only a slow oscillation is visible. The extrema appear at every half integer of the calculated round trip time. From the argumentation above and shown in Fig. 6.1 each peak corresponds to the coincidence of the bipolar TE strain overlapping with the same sign at a surface and the presence of the unipolar DP strain present at the other surface. Simplified, the integral over the bipolar strain is always zero unless it is incident on a surface, where at the top surface the strain has a negative sign and at the bottom surface the strain has a positive sign. The total strain leads to a thickness change and as the signs of the strain are different, the therefore unipolar displacement signal has also a different sign. The strain flip happens as explained in Section 2.5 due to the phase shift of π at the reflection of the acoustic pulse at a stress free surface. The peak at the Si surface (the maximum) is shorter in time than the peak at the Al surface (the minimum) corresponding to the different speeds of sound in media. The ratio of the Si peak width to the Al peak width is 4/3 in perfect agreement with the ratio between v_{Si} and v_{Al}. This evaluation will be advanced in the following section regarding the frequency analysis.

6.2.6. Frequency domain analysis

In this section the phonon dynamics will be investigated further utilizing advanced methods in the spectral domain. In Fig. 6.5(a)-(d)(corresponding to d_{Al} of 40 nm, 23 nm, 17 nm, and backside measurement of d_{Al} = 40 nm sample) and Fig. 6.6(d_{Al} = 10 nm sample) the Fourier transformations of the whole time transients shown in the figures 6.2 to 6.4(a) are shown (blue curves). The pulse train in the time domain transforms into a frequency comb with clearly separated equidistant spaced peaks. For the different samples sorted by their thickness (decreasing) the comb's modes range up to 100 GHz, 200 GHz, 300 GHz, and 500 GHz. As a consequence of the periodicity introduced in the system - due to the high-quality acoustic reflectors at the Al/air and Si/air free surfaces - these modes correspond to the longitudinal eigenmodes with the ground mode found at f_0 =10.0 GHz, 11.0 GHz, 12.05 GHz, and 12.05 GHz, respectively. The higher harmonics are visible up to the 9th, 18th, 24th, and 43rd order with the intensity equally distributed over nearly the whole frequency range with a maximum in the center around 50 GHz, 100 GHz, 120 GHz, and 150 GHz. When comparing the individual spectra, it is noteworthy that for the 10 nm sample only the odd modes are visible. This is due to the above mentioned suppressed asymmetric photoelastic and enhanced symmetric interferometric detection from the bipolar strain pulse at both surfaces.
The pulse trains in the time domain allow for the observation of each pulse's individual spectrum. Using a time-window with a width corresponding to the round trip time, i.e. the temporal distance between two pulses, with the center at the pulses pronounced minimum, the Fourier transformation yields the respective spectrum. For the 10 nm sample the pulse is detected two times per round trip, therefore, half the window width is used. The pulses are extracted from

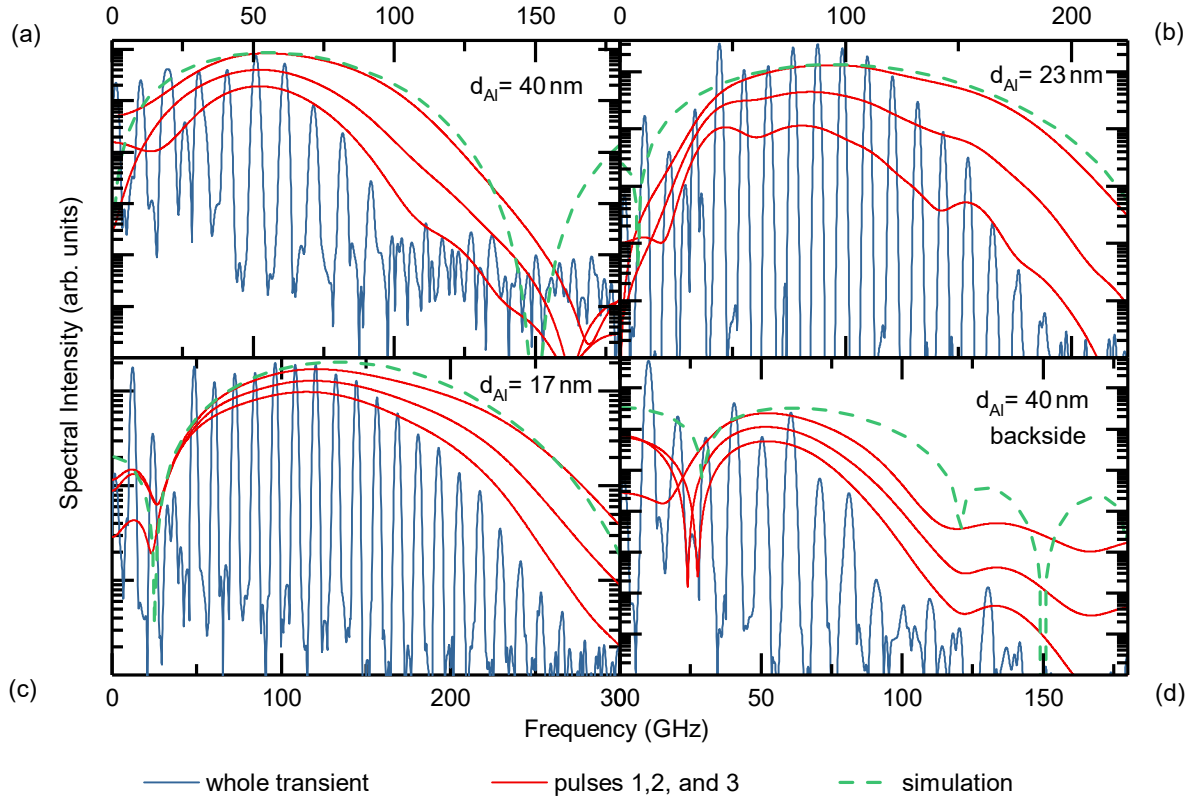

Figure 6.5.: Fourier spectra of the whole time transient (blue) and the first three pulses (red) of the a) 40 nm thick Al sample, b) 17 nm thick sample, c) 23 nm sample and d) backside-measurement of the 40 nm sample. The green dashed line shows the theoretical simulation of the excited pulse.

Fig. 6.2-6.4 with the time windows of 100 ps, 91.1 ps, 83 ps, and 41.5 ps. In Fig. 6.5(a)-(d) and Fig. 6.6 are additionally the first three Fourier spectra of the respective pulses plotted. Contrary to the spectrum of the pulse train, the individual spectra are continuous over the whole frequency range - resembling the envelope of the frequency comb. This is expected, as each pulse itself does not exhibit the information of the confinement, and the non-periodicity does not necessitate the splitting into eigenmodes. In the single pulse spectra it is seen from the comparison of the three spectra of the consecutive individual pulses that higher frequencies have a faster decay. This will be discussed in more detail further below.

By comparing the individual spectra at the 17 nm Al layer and the backside measurement of the 40 nm Al layer a dip in the low frequency regime becomes apparent. The dip appears in the pulses' spectra at 20-25 GHz, but is not visible in the spectra of the samples where no DP strain is generated. In fact, it can be explained as the result of the mutual compensation of the spectral amplitudes of TE and DP strain at this certain frequencies. In Fig. 6.1 both temporal strain distributions are plotted with different signs and the corresponding spectra are calculated in Section 3.7.4. Approximating Eq. (3.32) under the assumption of no impedance mismatch between the Al and the Si layers, which means the transmission at the interface is 1 and the

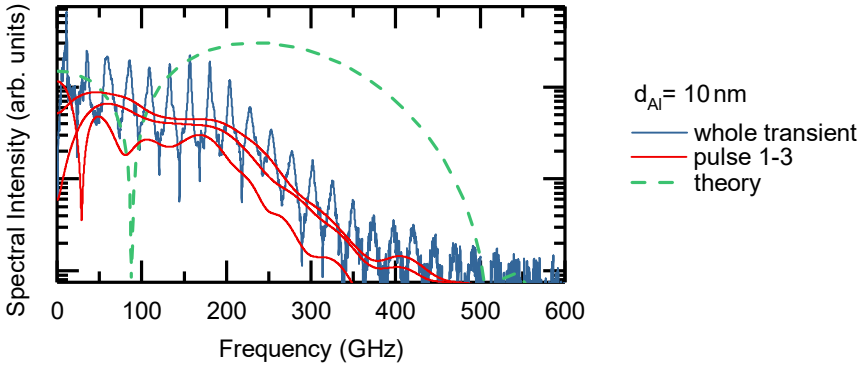

Figure 6.6.: Fourier spectra of the whole time transient (blue) and the first three pulses (red) of the 10 nm sample. The green dashed line shows the theoretical simulation of the excited pulse. Note the change of the frequency scale compared to Fig. 6.5.

reflection is 0, one obtains for the theoretical spectral amplitude:

$$\tilde{D}(\omega) = \tilde{D}_{TE} + \tilde{D}_{DP} \propto \frac{\sin^4(\omega\tau_{Al}/2)}{(\omega\tau_{Al}/2)^2} - \mu\frac{v_{\mathrm{Si}}}{2v_{\mathrm{Al}}}\frac{\sin^2(\omega\tau_{Al}/2)}{(\omega\tau_{Al}/2)^2}\cos(\omega\tau_{Al}), \tag{6.1}$$

where the first term of the sum ($\tilde{D}_{TE}$) labels the spectral amplitude of the TE strain and the second term ($\tilde{D}_{DP}$) the DP strain. The parameter μ quantifies the relative amplitudes of the DP and TE strain. The main difference beside the different signs of both strains is the non-zero amplitude of the DP strain at low frequencies compared to the zero amplitude of the TE strain. When one assumes $0 < \mu \ll 1$ to be small, i.e. for $\omega\tau_{Al}$ the small angle approximation to be true, one can find Eq. (6.1) to be zero at:

$$f_\mu \approx \sqrt{\mu 2 v_{\mathrm{Si}}/v_{\mathrm{Al}}}\frac{f_{Al}}{\pi} \ll f_{Al} \tag{6.2}$$

with $f_{Al} = 1/(2\tau_{Al})$ the fundamental resonance frequency of a free-standing Al film. Inserting $f_\mu = 23$ GHz from the 17 nm sample, one obtains $\mu = 0.06$. This is half the value obtained from the comparison of the amplitudes (evaluated above). The extraction from the spectrum seems to include less errors, as the amplitude-comparison depends on identical DP strains at the front and back side of the membrane and the attenuation in one round trip (the time between both looked-at amplitudes) might not by negligible. However, the approximations in Eq. (6.2) are only valid for small frequencies, where the solution gives a result at the edge of increased errors. But, the results are similar enough to corroborate the theory. Whereas the theory expects an absolute zero at the crossing point of both contributions, the experimental observation of the sharp non-zero dip instead stems mostly from thermal conduction. As previously shown in Section 3.4 this increases the low frequency parts in the TE strain for later times and leads to a weakened compensation due to the spectral components of both, leading and trailing part of the first pulse.

The evaluation of the fundamental resonance frequency of the respective Al film provides a quick estimate at which frequency the spectrum of the acoustic pulse has an absolute maximum. One obtains for the different samples: 50 GHz for the 40 nm sample, 130 GHz for the 23 nm

Table 6.1.: Simulation parameters for the different samples. For the 42 nm sample two different parameters for the front and backside simulation were used.

v_{Al} [m/s]	Z_{Al} [GPa s/m]	d_{Al} [nm]	d_{Si} [nm]	μ
6000	16.2	10	336	0.33
		17	326	0.055
v_{Si} [m/s]	Z_{Si} [GPa s/m]	23.5	351	0.01
8430	19.6	42	358	0 / 1

sample, 175 GHz for the 17 nm sample, and 300 GHz for the 10 nm sample. This is in fairly good agreement with the measurements.
In Fig. 6.5(a)-(d) and Fig. 6.6 the theoretical spectral amplitudes of the first pulse are calculated with Eq. (6.1) and shown as dashed lines. The values used for the simulation are taken from Table 6.1 and were chosen for the best agreement of all samples.
A good agreement between experiment and the analytical model is observed. The dips stemming from the compensation of the TE and TP strain are well reproduced and the maximum positions and widths are quantitatively well reproduced. Only for the 10 nm sample - where photoelastic detection is not the main detection mechanism - the modeling fails. This could be optimized by using a more detailed model including symmetric detection with a Fabry-Pérot mechanism.
The relative amount of DP strain compared to the TE strain was changed in the 40 nm sample by pumping and probing from the backside. The spectra have the same spectral width, but, by comparing the spectra of the front side and backside measurement (see Fig. 6.5(a) and (d), respectively), additional dips arise in the backside measurement, which are very good reproduced by the model.

6.2.7. Distinctive two-layer modes

When assuming only one layer, the possible eigenmodes will be given the by the inverse round trip time and its higher harmonics (see for example the standing waves in Section 2.4). A strictly linear relationship between eigenmodes and modenumbers evolves. The evaluation of the modes in Figs. 6.5-6.6, however, shows a slight variation around the expected linear relationship. This is due to the different impedances of the two materials of the bilayer. An analytical prediction is calculated in Section 2.6. The normalized deviation of each modes frequency from the linear slope $n \cdot f_0$ over mode number n is plotted in Fig. 6.7. The normalization was done by dividing with the ground mode frequency f_0, which can be calculated by the inverse round trip time of the bilayer system. A sine-like modulation around zero (zero defining the linear relationship) is apparent. While the amplitude for all thicknesses is the same with 3 %, the period is thickness dependent and a thinner Al film leads to a larger period. The theoretical curve plotted as dashed line Fig. 6.7 is described by (see Eq. (2.48)):

$$\frac{f_n - n \cdot f_0}{f_0} \approx \frac{1}{2\pi}\left(1 - \frac{Z_{\mathrm{Si}}}{Z_{\mathrm{Al}}}\right)\sin\left(\frac{2\pi}{1+\tau_{\mathrm{Si}}/\tau_{\mathrm{Al}}}n\right), \tag{6.3}$$

where Z_x is the impedance and τ_x the propagation time for the x =Al-, Si-layer. For the modeling the values given in Table 6.1 are used, where the material parameters for Al and Si are taken from the literature with the impedance and speed of sound of Al being 5 % smaller to

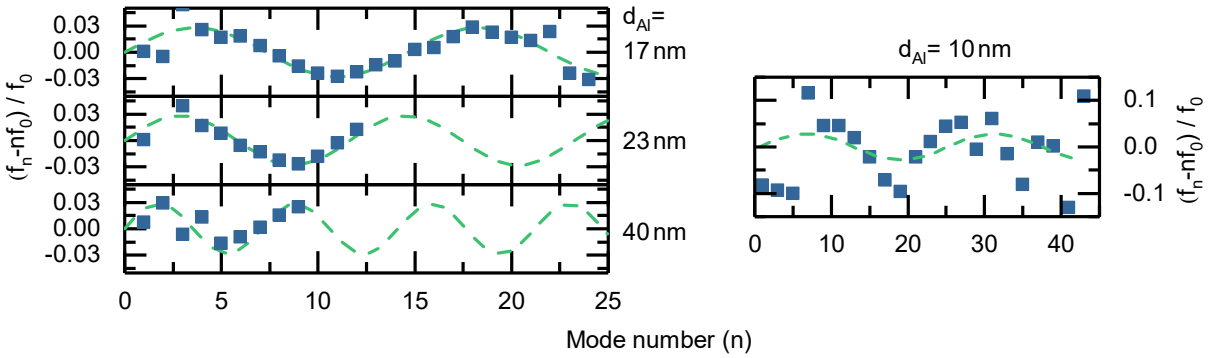

Figure 6.7.: Each modes deviation from a linear slope $n \cdot f_0$ is plotted over its mode number n for all discussed sample thicknesses. The deviation is scaled by the ground mode frequency f_0, corresponding to the inverse round trip time in the bilayer. The solution of the approximate eigenmode equation is shown as dashed line.

obtain the best results. This reduction may be an effect from the polycrystalline structure of the evaporated Al film. The period and amplitude of the model and the experiment match very well.

However, while the period is reproduced nicely, the deviations for the 10 nm sample are up to three times stronger than predicted by the theory. From Eq. (6.3) one can see that the amplitude of the oscillation is governed by the ratio of the impedances of the materials of the bilayer. A bilayer with identical impedances will not develop a modulation. This hints, that the impedance of the thinnest Al layer deviates from the thicker Al layers. Both, density and speed of sound of a very thin layer, will be dependent on the grain quality and oxidation of the film and the first effects are obtained from this measurement.

It should be mentioned that the parameters in Table 6.1 were chosen for a good agreement to the experimental data, but they are very close to the values, which were determined by ellipsometry and AFM measurements. Additionally, some details were not taken into account for the modeling. For example, the natural oxide layers of Si and Al were neglected, but are not assumed to have a large impact on the results. The effect of imperfect adhesion can be neglected and will be discussed for imperfectly adhered Al films in Section 6.3.

6.2.8. Frequency dependent phonon lifetimes

The time resolved measurement of the individual samples allowed so far to measure the effect of TE and DP strain and to detect the modulation of the eigenmodes. Furthermore, the clear separation of the pulses in time allows for the extraction of the frequency dependent phonon decay, i.e. the lifetime. In Fig. 6.8(a) the Fourier transformations of the 13 individual pulses of the 17 nm Al sample are shown. The same time window was used for every transformation as explained above for the extraction of the first three pulses. Cuts along three frequencies shown as black (solid, dashed, dotted) lines are. In Fig. 6.8(b) the amplitudes of the specific frequencies (indicated as solid, dashed, dotted line connecting the data points) over the time delay of the respective pulse's spectrum are plotted. In the logarithmic plot a linear relationship is visible, whereas the three different frequencies have three different slopes indicating a different

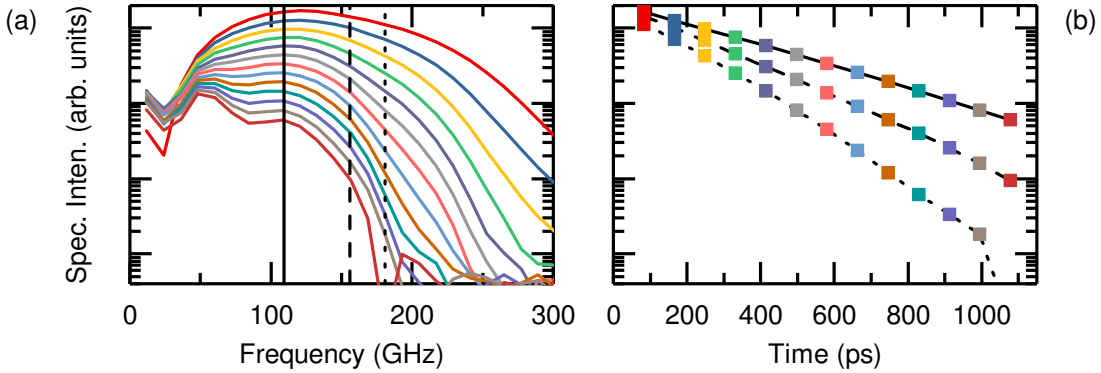

Figure 6.8.: (a) Fourier spectra of all 13 pulses visible in the time transient of the 10 nm sample.(b) Time resolved amplitudes of three different frequencies, marked as solid (110 GHz), dashed (155 GHz), and dotted line (180 GHz).

lifetime. By fitting an exponential function to the data points over time, individual frequency dependent lifetimes can be extracted. This is done for all measurements with 9 pulses for the 40 nm backside sample, 12 pulses for the 40 nm front side sample, and 13 pulses for the 23 nm sample.

The evaluated frequency dependent phonon lifetimes are shown in Fig. 6.9. Only the frequencies corresponding to the eigenmodes were evaluated, but in principle an extraction over the whole frequency spectrum is possible. Included are the error bars from the exponential fit, indicating a larger error for lower frequencies. Additionally two slopes proportional to ω^{-1} and ω^{-2} are shown as guide to the eyes. The lifetimes range from 800 ps at 50 GHz to 50 ps at 300 GHz. The extracted lifetimes below 36 GHz are not shown, because they seem to be larger than the measurement windows, which leads to a large error in the fit and the mutual compensation of TE and DP strain in this frequency range leads to not to trust worthy amplitudes. Comparing the individual lifetimes, the sample with the thickest Al film has a two times lower lifetimes indicating the main attenuation process to be in the Al and not in the Si. At lower frequencies the lifetimes follow a ω^{-2} behavior, whereas for higher frequencies a ω^{-1}-decay is visible. In the intermediate regime a plateau becomes apparent, which stems mostly from the resonant attenuation in the thin film, described by the spectral transfer function. Depending on the reflection between both materials its influence can be quite dramatic (see Section 6.3).

It should be noted that the determined lifetimes are not intrinsic lifetimes, but they are governed by extrinsic mechanisms [1]. This is corroborated by other measurements on pure Si. Daly et al. measured the amplitudes of two longitudinal acoustic phonon packets with 50 and 100 GHz generated in a thin Al layer on top of a 50 µm Si wafer after one and two round trips. They found, by comparing the amplitudes, the lifetimes to be 6.8 and 5.0 ns, respectively [Dal09]. In those samples the surface effects are mostly suppressed and thus the results should be a lower limit of the intrinsic lifetime (one magnitude larger than the measured values here). Cuffe et al. measured bare Si membranes in a similar frequency range, where the lifetime of the fundamental mode was determined [Cuf13]. By tuning the membrane's thickness, the frequency could be changed. Their results are shown additionally in Fig. 6.9. Similar frequency dependent

[1] For a summary of the most important intrinsic and extrinsic attenuation processes see Section 2.7.1

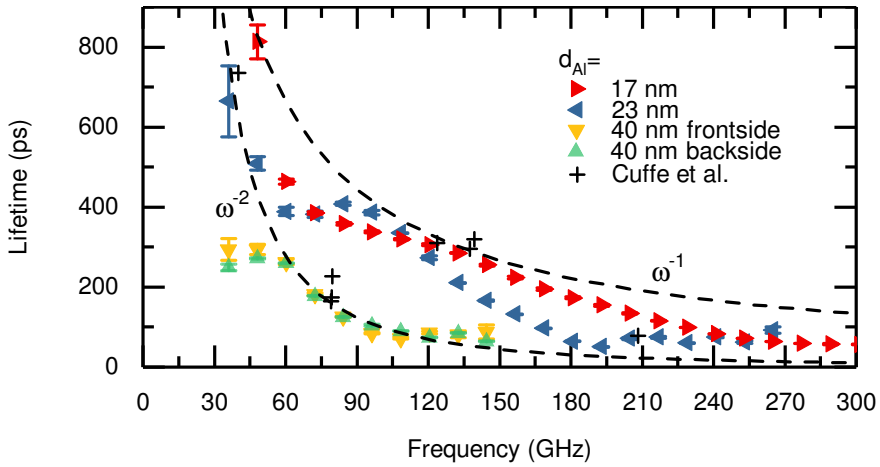

Figure 6.9.: Frequency-dependent phonon lifetimes extracted from the different samples. The error bars are calculated by the quality of the exponential fit of the spectral amplitudes over time.

lifetimes are found and Cuffe et al. explained the comparatively lower lifetimes compared to the intrinsic lifetimes by increased scattering due to surface roughness (this mechanism is explained in detail in Section 2.7.1). The membranes exhibit similar properties, although one surface has been exchanged by an Al film, allowing the generation of a broad range of frequencies and the simultaneous detection of many pulses, leading to a small error bar. The polycrystalline structure or roughness of the Al film seems to exhibit similar dissipation properties as a rough membrane's surface. In Section 5 intentionally roughened membranes are discussed. In this section scattering and inhomogeneous broadening will be important. Imperfect adhesion is measured and discussed for a similar system in Section 6.3. A comparison to further values found in the literature is given in the Appendix.

6.3. Weak adhesion

In this section the interfacial adhesion of Al thin films on Si membranes is studied. A detailed analysis of this bilayer is presented including a precise modeling of occurring features. It is shown that the adhesion can be modeled by a massless spring attaching both layers. However, dissipation in each layer has to be considered for an accurate simulation and description. By analyzing the changes of subsequent acoustic echoes in the Al layer, a spectral transfer function is extracted, which yields all necessary features for an exact description of the structure - just 5 parameters. The measured spectrum consists of frequencies from few GHz to 800 GHz. In the following $\omega = 2\pi f$ denotes the angular frequency with f the frequency.

6.3.1. Experimental results

A sketch of the sample is shown in Fig. 6.10(a). The detailed processing steps are explained in Section 4.2. Contrary to the samples in Section 6.2 the Al is thermally evaporated resulting in a reduced interface adhesion of the 13 nm Al film on top of a 350 nm thick Si membrane. The sketched springs depict the bad adhesion but are not willingly included during the fabrication process. The thickness of the membrane was measured optically by ellipsometry and the thickness of the Al film was measured mechanically by a quartz crystal during evaporation and atomic force microscopy after deposition. All thicknesses were remeasured acoustically in the pump-probe experiments. The experimental setup is explained in Section 4.1. The pump power was 30 mW at a wavelength of 790 nm and the probe laser power was 5 mW at a wavelength of 820 nm. The spot sizes were below 2 µm.

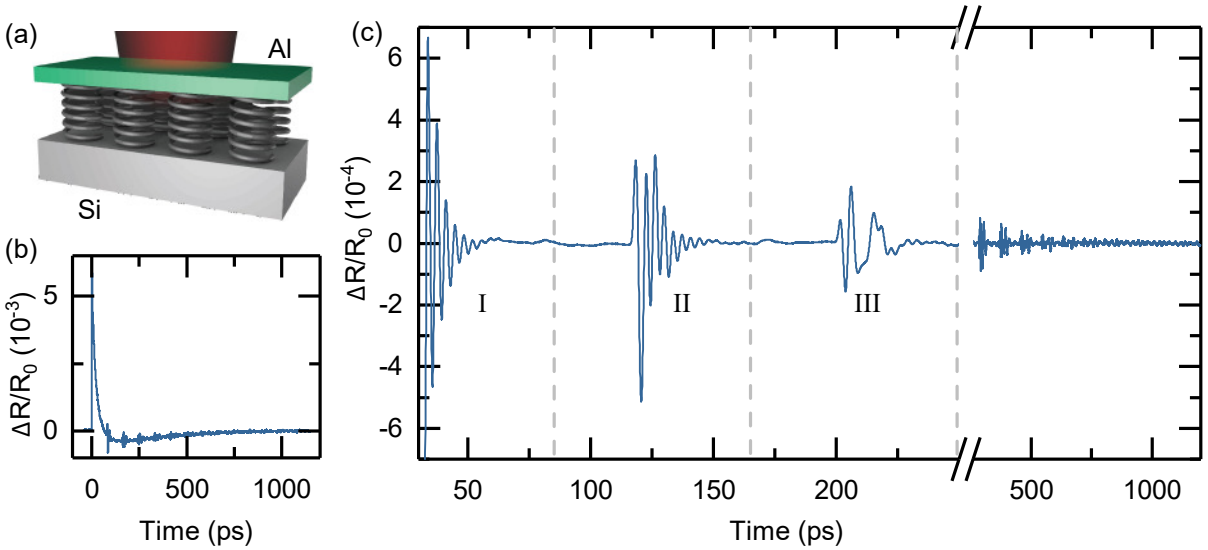

Figure 6.10.: (a) Sketch of the excitation and detection of a thin Al film coupled by springs to a Si substrate (thickness of layers and springs are not to scale). (b) Transient of the relative reflectivity change of the Al film upon excitation. (c) Time-resolved modulation of the probe beam without electronic background. The parts labeled with I, II, and III are described in detail in the text.

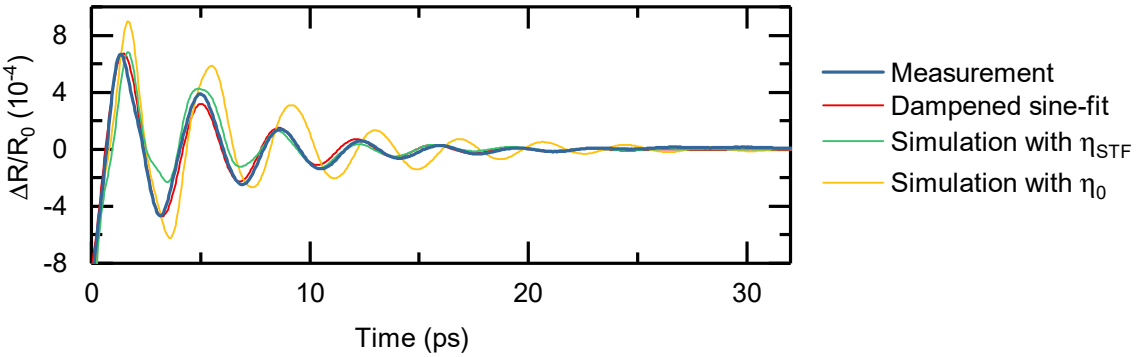

Figure 6.11.: Zoom of the regime I, the oscillation in the beginning of the measurement (blue line). A dampened sine fit is superimposed (red line). Additionally, two simulations assuming adhesion with attenuation (η_α, green line) and adhesion without attenuation (η_{STF}, yellow line) are shown. The parameters used are given in Table 6.2.

In Figure 6.10(b) the time trace of the relative reflectivity change is shown. The phononic contribution is shown in Figure 6.10(c) where the electronic background is subtracted. Starting at the electronic peak's maximum position within the first 30 ps a dampened oscillation is apparent, which is labeled regime I. After tens of picoseconds where no signal is apparent, 88 ps later, a pulse with a similar oscillation at its tail emerges in regime II. It appears again in regime III 88 ps later with a change in amplitude and of the oscillatory features. Each 88 ps it reappears, while undergoing amplitude and shape transitions.

The physical processes following the pump's excitation are explained in Section 3.2 and depicted for perfect adhesion in Section 6.2.1. Here, the explanation of the main features will be reproduced. The pump pulse excites hot electrons in the Al film and due to the high absorption of the Al (absorption length $\approx$ 10 nm at a wavelength of 800 nm) the pump's intensity in the Si is very low. The electrons equilibrate with each other and the Al atoms, thereby, inducing a homogeneous thermoelastic stress in the lattice. Because the pump spot is larger than the substrate's depth it is sufficient to consider the strain propagating perpendicular to the surface - across the interface into the Si.

In Section 6.2 the reflection and transmission at the Al/Si-interface were mostly neglected. However, it can not be neglected anymore to describe the transient sufficiently. The dampened oscillation in the beginning (regime I) is a direct consequence of the weak-adhesion-induced increased reflection at the interface. Upon reflection the strain pulse reverberates in the Al film leaking only a fraction of its energy into the Si membrane during each round trip. The transmitted strain distribution - including the multiple reflected components - returns after one round trip to the Al film and gets detected as echo 1 in regime II. Nevertheless, it will also undergo a reflection at the Al film and also reverberations in the Al film, leading to the detection of echo 2 in regime III and so forth. The different shapes of the echoes are explained in the following and can be attributed to frequency-specific mode shaping - induced by the weak coupling of both layers - and dissipation processes.

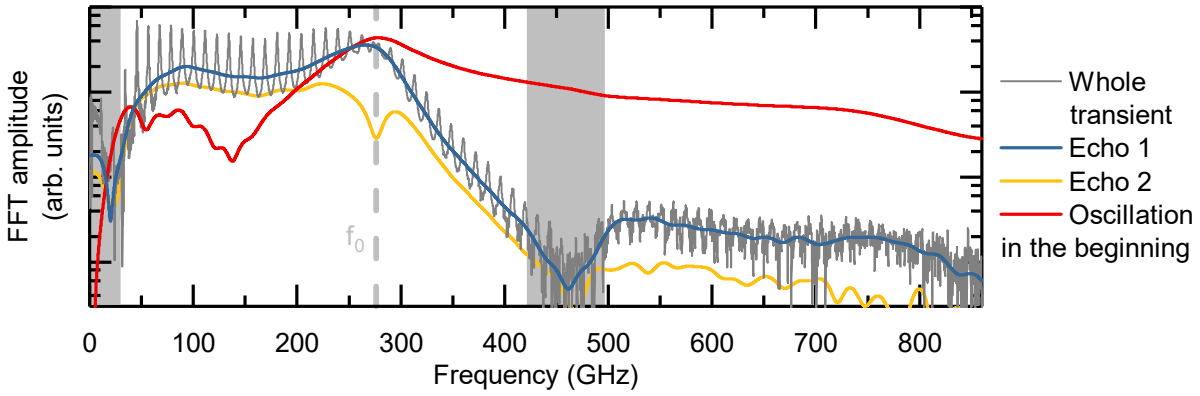

Figure 6.12.: (a) Fourier transformations of the time domain data of the regimes I, II, and III labeled in Fig. 6.10, and of the whole time transient. Note the logarithmic scale. The dashed gray line shows the frequency f_0 of the oscillation in the beginning evaluated by a sine-fit. The gray areas mark regions with a very low spectral amplitude of the echoes 1 and 2.

6.3.2. Initial oscillation of the film

In the following, the oscillation in the beginning will be discussed according to the usual approach in the literature [Tas98]. In first approximation this oscillation is assumed to be a fundamental eigenmode of the freestanding (weakly-coupled) Al film. An exponentially dampened sine-function is fitted to the measured data (see Fig. 6.11): $A \cdot \exp(-t/\tau_0)\cos(\omega_0 t - \phi)$, with A the amplitude, τ the damping time, ω_0 the angular eigenmode frequency, and ϕ a phase. A remarkably good fit is possible yielding for the frequency $\omega_0 = 1.77 \cdot 10^{12}$ /s, or $f_0 = 281$ GHz and for the damping time $\tau_0 = 5$ ps. Derived in Section 2.4, the frequency of a free-standing film is given by $f_0 = v_{\mathrm{Al}}/2h_0$, where $v_{\mathrm{Al}} = 6000$ m/s is the speed of sound in Al and h_0 is the thickness of the film. This gives for the Al film a thickness of $h_0 = 10.7$ nm, underestimating the thickness value obtained by other methods.

When one inserts the round trip time of the Al film in the oscillation's decay, the reflection coefficient is obtained: $r_0 = \exp(-f_0\tau)$. This can be compared with the reflection coefficient (Eq. 2.32) derived earlier for the case of imperfect coupling between both layer and the adhesion at the interface simulated by coupling both layers with springs. Inserting all parameters, the spring constant derived from the first oscillation is obtained: $\eta_0 = 8\,\mathrm{kg\,nm^{-2}s^{-2}}$. It is in the range of values found for Au on Si samples by Tas et al. of $\eta_{\text{Au-Si}} = 13\,\mathrm{kg\,nm^{-2}s^{-2}}$ [Tas98] and Antonelli et al. of $\eta_{\text{Au-Si}} = 6\,\mathrm{kg\,nm^{-2}s^{-2}}$ [Ant06]. So far, attenuation was neglected, but the measured eigenmode's damping time is limited by a convolution of transmittance into the Si membrane and attenuation in the Al film. Both effects can not be disentangled from observing just the oscillation in the beginning. It will become apparent in the following that a more detailed approach is necessary to obtain quantitative reliable values. This needs an analysis of regime II and III as well.

6.3.3. Frequency Comb

A deeper analysis of the residual data is not solely possible in the time domain, but needs to regard the frequency domain as well. The Fourier transformations of regime I, II, and III are shown in Fig. 6.12. Additionally the Fourier transformation of the whole pulse train of the echoes is shown. A maximum for regime I is seen at $f_0 = 280\,\mathrm{GHz}$, which was already obtained by the dampened sine-fit of that data. Its broad peak corresponds to the few oscillation in time.

As the echoes 1 and 2 are clearly separated in time, the Fourier transformation is not window limited and the echo's spectra will be quite precise. In the frequency domain the spectrum of echo 1 spans from a few GHz to 430 GHz and from 500 to 800 GHz. Between those maxima at 10 GHz and 460 GHz pronounced dips with a vanishing amplitude are visible. The spectrum has a maximum at f_0. The spectral amplitude of echo 2 resembles the spectral shape of echo 1, only with a decreased amplitude. Instead of the maximum at f_0 a dip in the spectrum is seen at exactly this frequency. The spectrum of the whole pulse train resembles the spectrum of echo 1. However, the spectrum is not smooth, but a frequency comb like structure with a frequency spacing of 12 GHz emerges. As explained in Section 6.2 the frequency comb stems from the repeated round trips of the echoes in the acoustic cavity given between the Al surface and the Si surface. The spacing of the peaks is given by the fundamental eigenmode of the system, i.e. the inverse round trip time, $f_{\mathrm{RT}} \approx t_{\mathrm{RT}}^{-1} \approx (2[t_{\mathrm{Al}} + t_{\mathrm{Si}}])^{-1} \approx (83\,\mathrm{ps})^{-1} \approx 12\,\mathrm{GHz}$ with t_{Al} and t_{Si} the respective propagation times for a single pass of the acoustic pulse in Al and Si, and t_{RT} the total round trip time in the bilayer system.

In Section 3.7.4 the theoretical spectrum of echo 1 for a bilayer is derived. It is found that in dependence of the adhesion the spectrum undergoes a strong change in shape. In Fig. 6.13(a) the measured spectrum of echo 1 is compared to the calculated spectrum (Eq. (3.32)) assuming the above extracted parameters (h_0, η_0) from the oscillation in the beginning (yellow dashed line). The agreement is not very good, as the overlap with the measured spectrum at higher frequencies is not present, while the dip in the spectrum at 200 GHz is overestimated and at f_{Al} the maximum is diverging. It shall be noted that the dip around 200 GHz is not present for the modeling of perfect adhesion.

Furthermore, the spectrum of weak adhesion including attenuation using the values given in Table 6.2 is shown (green solid line). A good agreement between theory and experiment is obtained. The main features are well reproduced, which shows the quality of this simple model. However, around 100 GHz the spectrum is overestimated and for frequencies around 500 GHz the spectrum is underestimated. It shall be noted that the parameters given in Table 6.2 are not chosen arbitrarily but exhibit the best fit to other system-dependent values obtained in the following.

Considering the derivation of the analytical model in Section 3.7.4 these assumptions might be responsible for the still present disagreement: The excitation and detection mechanisms are assumed to be perfectly homogeneous. Additionally, it is possible that the assumed attenuation behavior is wrong, but the assumptions will be corroborated in the following. Therefore, in the following an alternative approach to extract the interface adhesion and the adhesion in a self-sustaining way is presented. It does not need explicit knowledge of the excitation and detection process.

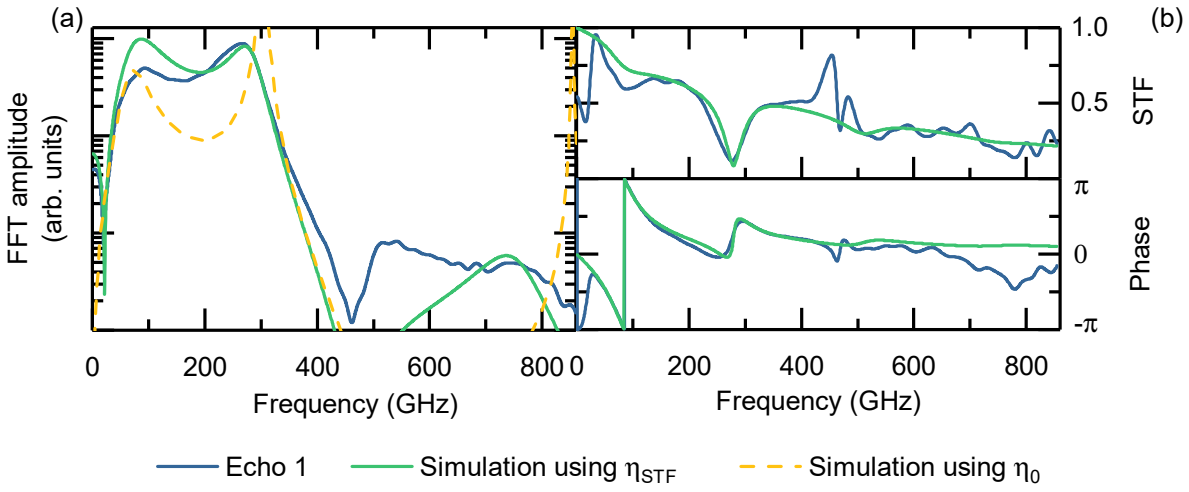

Figure 6.13.: (a) Comparison of the spectrum of echo 1 (blue line) to the simulation of weakly adhered bilayers with h_0 and η_0 obtained from the oscillation in the beginning (yellow dashed line), and with the values from Table 6.2 including adhesion (green solid line). (b) The experimental spectral transfer function (STF) given by the ratio of echo 2 and echo 1. It is splitted into absolute value and phase. Additionally, the simulated STF is shown.

6.3.4. Spectral transfer function

By utilizing a spectral transfer function STF only the clear separation of the pulses in time is necessary. This can be understood by looking at the evolution of the pulses. One can assume the exact generation in the Al and transmission into the Si membrane to be given by G_{Al}. The propagation in the Si membrane, reflection at the Si membrane's surface to be 1, and the back-propagation in the Si membrane shall be given by P_{Si}. The detection in the Al shall be given by D_{Al}. The reflection of an acoustic pulse including reverberations in the Al film is given by the spectral transfer function Γ - derived in Section 2.5.3. Then, the detected signal by echo 1 can be written as $R_{\mathrm{echo1}} = D_{\mathrm{Al}} \cdot P_{\mathrm{Si}} \cdot G_{\mathrm{Al}}$ and the detected signal by echo 2 can be written as: $R_{\mathrm{echo1}} = D_{\mathrm{Al}} \cdot P_{\mathrm{Si}} \cdot \Gamma \cdot P_{\mathrm{Si}} \cdot G_{\mathrm{Al}}$. The ratio of both pulses is given by: $STF = P_{\mathrm{Si}} \cdot \Gamma$ and, thus, independent of the excitation and detection processes.

In Figure 6.13(b) the ratio of the spectra of the second and the first echo - the experimental STF - is shown as blue solid line separated into absolute value and phase. At lower frequencies it is near 1 and decreases for higher frequencies to 0, while exhibiting a pronounced dip in between at f_0. The double-peak like structure around 460 GHz is an artifact due to the small spectral amplitude of echo 1 and 2 at that frequency. Considering the phase, this is mostly smooth around zero exhibiting only a strong decrease in the beginning and a bipolar feature at f_0.

The analytical spectral transfer function is described in detail in Section 2.5.3. When the scattering at the Al/air-surface and the Si/are surface is assumed to be included in the overall

attenuation of each layer. It can be written as:

$$STF = P_{\mathrm{Si}} \cdot \Gamma = \exp(2ik_{\mathrm{Si}}h_{\mathrm{Si}}) \cdot \left(1 - \frac{2}{1 + \frac{i\omega Z_{\mathrm{Si}}}{\eta} - \frac{Z_{\mathrm{Si}}}{Z_{\mathrm{Al}}}\frac{1+\exp(2ik_{\mathrm{Al}}h_{\mathrm{Al}})}{1-\exp(2ik_{\mathrm{Al}}h_{\mathrm{Al}})}}\right) \tag{6.4}$$

with k_{Al} and k_{Si} the complex acoustic wavevectors, h_{Al} and h_{Si} the thicknesses, and Z_{Al} and Z_{Si} the complex acoustic impedances of Al and Si, respectively. The spring constant η is the real valued spring constant per unit area defined in Section 2.3. Γ is defined in Eq. (2.41) and P_{Si} denotes the dissipational changes to the spectrum while passing the Si twice. The STF is plotted in Fig. 6.13 with the values from Table 6.2. A good agreement between experiment and simulation for absolute value and phase can be seen. Careful tuning of the 5 different parameters was done to obtain the best fit. It shall be noted that the fit was done only at frequencies where the spectral amplitude of echo 1 is non-negligible (the non-grayed areas).

The thicknesses and the spring constant are three constant parameters and, thus, easy to fit to the best value using a least-square algorithm. For the attenuation a frequency dependent function is needed. In Section 2.7 different models for the attenuation are presented and shown to follow a constant decay, a $1/\omega$, and/or an $1/\omega^2$ decay - depending on the mechanism and the looked-at frequency range. It is found here that for the bilayer system Al on Si, the best fit is obtained when assuming a $1/\omega$ decay in both layers.

To check for the quality of the fit and proof the precise evaluation of the material parameters, next, the extracted parameters are slightly varied. From Eq. (6.4) it is clear that the STF can be clearly separated in two parts: P_{Si} and Γ. It is found that the variation of the Si impedance by variation of the Si attenuation in Γ can be neglected compared to the contributions of the attenuation in Al and the spring constant. Therefore, the discussion is divided in three parts, where i) the attenuation in Si is changed to check for changes in P_{Si}, ii) the attenuation in the Al is changed to check for changes in Γ, and iii) the spring constant is changed in the resulting STF, while keeping the other parameters at the same values. The individual amplitudes of the respective $1/\omega$ decay are varied by $\pm 30\,\%$. Furthermore, a constant and a $1/\omega^2$ decay are assumed with the amplitudes adjusted to obtain a similar decay at f_0 after one round trip.

In Fig. 6.14(a) P_{Si} is plotted for different attenuations in Si. Corresponding to the assumption of the $1/\omega$ decay an exponential frequency decay becomes apparent after one round trip in the Si. The variation of the amplitude changes the slopes of the decay slightly (dashed and dotted gray lines) sandwiching the extracted value (green line). The constant decay leads to a constant value, while the $1/\omega^2$ decay exhibits a very different curvature - bending two times.

In Figure 6.14(b) Γ is plotted for different attenuations in Al. The spring constant is fixed at the value given by Table 6.2. It shows the changes to the spectrum before entering the Al film and

Table 6.2.: The parameters used for the simulation. h denotes the thickness of the respective layers. τ denotes the lifetime in dependence of the frequency. η is the spring constant.

h_{Al} (nm)	h_{Si} (nm)	τ_{Al}	τ_{Si}	η_{STF} ($\mathrm{kg\,nm^{-2}s^{-2}}$)	h_0 (nm)	η_0 ($\mathrm{kg\,nm^{-2}s^{-2}}$)
13.2	352	$12.6/\omega$	$300/\omega$	17	10.7	8

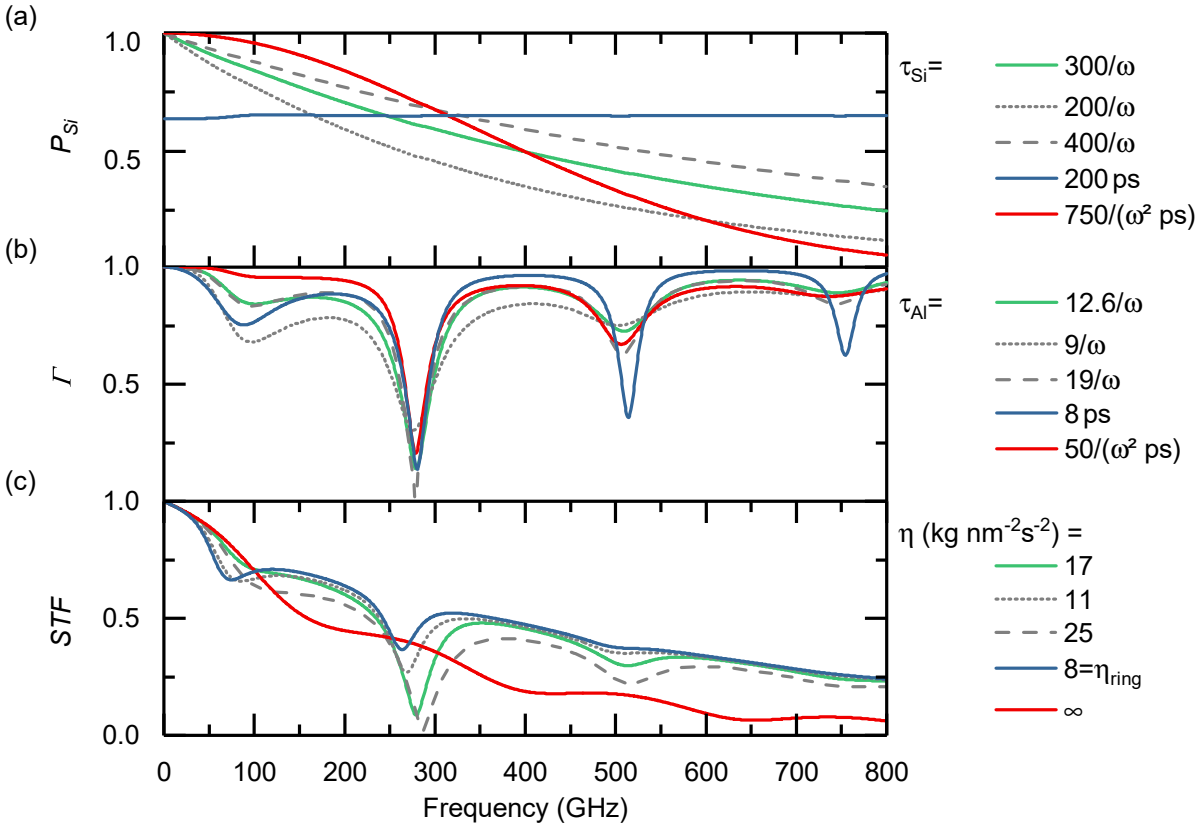

Figure 6.14.: (a) Simulated spectral transfer function P_{Si} in the Si layer - leading to a decay only. Three different lifetime behaviors are used for the simulation $(1/\omega, 1/\omega^2, const)$. (b) Simulated spectral transfer function Γ. Three different lifetime behaviors are used $(1/\omega, 1/\omega^2, const)$ while keeping the spring constant fixed. (c) Simulated spectral transfer function STF for different spring constants while keeping the attenuation in the Al and Si fixed.

after leaving the Al film. For the assumed $1/\omega$ decay given by Table 6.2 it is seen that the low damping at lower frequencies in the film and the increased reflection for higher frequencies at the interface (Eq. (2.32)) lead to a nearly frequency-independent slope with an overall negligible attenuation (green solid line). However, pronounced dips at 100 GHz, 280 GHz, and 510 GHz emerge with the dip intensity decaying upon increasing frequency. This increased damping is due to resonant coupling into the Al film at exactly those frequencies. The amplitude variation for the $1/\omega$ decay sharpens (dashed gray line) or softens (dotted gray line) the dips. The constant decay leads to an increase of the dip intensity at higher frequencies, while the $1/\omega^2$ decay softens the dip at 100 GHz nearly up to extinction. The frequency spacing between the individual dips is given by the undisturbed eigenmode oscillation of the Al film $v_{\mathrm{Al}}/2h_{\mathrm{Al}} < f_0$.
In Figure 6.14(c) the super position of both decays - in fact the STF - is plotted for the parameters from Table 6.1 (green solid line). Additionally, the effect of a variation in the spring constant is shown while keeping the attenuation fixed. A variation of the spring constant by ±30 % leads to an amplitude and frequency shift of the dips. Increased adhesion (smaller η)

increases the dips while leading to a blue shift and weaker adhesion (smaller η) weakens the dips leading to a red shift. When assuming perfect adhesion ($\eta = \infty$) the dips shift to higher frequencies until the first dip has the same distance from zero as the spacing in between the dips. Additionally, the dips intensity decreases to a mere modulation of the slope, induced by the weaker reflection and resonance effect just due to the impedance mismatch. For no adhesion ($\eta = 0$) the bilayer would be detached and perfect reflection would appear at the interface leading to a decay only due to the Si. However, no strain would be able to propagate from the Al film into the Si membrane and, thus, only the dissipation of the Al film would be measured.

In conclusion, the features of the STF can be qualitatively explained as follows. The overall decay is directly linked to the dissipation in the Si, where the lifetime decay is found to be $\tau = 300/\omega$. The spacing of the dips is given by the inverse thickness of the Al film. The amplitudes of the dips are dependent on the spring constant and the attenuation in the Al, where due to the monotone slop, only the lifetime at $f_0 = 280\,\mathrm{GHz}$ can be extracted to be $\tau = 45\,\mathrm{ps}$. Additionally, the zero offset of the dips depends on the spring constant.

The extracted Al dissipation of $\alpha_{\mathrm{Al}} = 23000\,\mathrm{cm}^{-1}$ at 280 GHz corresponds well to results found by Bryner et al. of $\alpha_{\mathrm{Al}} = 8900\,\mathrm{cm}^{-1}$ at 30 GHz and $\alpha_{\mathrm{Al}} = 20500\,\mathrm{cm}^{-1}$ at 50 GHz [Bry10]. The Si lifetime values extracted from the STF corroborate the findings in Chapter 5, where also a $1/\omega$ decay is found. The values itself correspond well to Si dissipation in the literature. The lifetime of $\tau = 300/\omega$ acts as an upper boundary for the data obtained by Cuffe et al. [Cuf13]. It shall be noted, that Cuffe et al. propose surface roughness as the governing dissipation process. Under this assumption an increase of the lifetime by exchanging one of the surfaces with an Al film seems reasonable. The surface dissipation may well be included in the strength of the spring or the attenuation in the Al. Further measurements would have to be done to distinguish extrinsic from intrinsic processes. A comparison to further values found in the literature is given in the Appendix.

The value obtained for the spring constant of $\eta_{STF} = 17\,\mathrm{kg\,nm^{-2}s^{-2}}$ is twice larger than the value of $\eta_0 = 8\,\mathrm{kg\,nm^{-2}s^{-2}}$ obtained from the oscillation in the beginning of the measurement (see Section 6.3.2). Comparing the STF for both values corroborates the need for this detailed analysis to obtain a precise value describing the adhesion. Furthermore this approach yields information regarding the acoustic damping behavior in the adhered layers. It should be noted, however, that the adhesion might by mediated by the native SiO_2 of the Si membrane's surface.

Although, the advantage of this method of extraction is at hand, it is convenient to see if the other developed tools explain the main feature of the measurement as well. Therefore the oscillation in the beginning and echo 1 are simulated with the values of Table 6.2 for both spring constants extracted by the oscillation in the beginning and the STF. Homogeneous excitation and detection is assumed. The simulation is done accordingly to Eq. (3.32). In Fig. 6.11 the time domain data of the oscillation in the beginning is shown. The agreement between simulation and measurement is very good for η_{STF}, whereas the simulation with η_0 shows a wrong oscillation period and decay time. In Fig. 6.13(a) the measurement and the simulation of the spectrum of echo 1 is shown. A good agreement between measurement and simulation can be seen for η_{STF}, but the measured spectrum is underestimated around 100 GHz, which may well be due to the assumed homogeneous excitation. These findings show the quality of the tools developed in the understanding of this bilayer system and corroborates the preciseness of the obtained values.

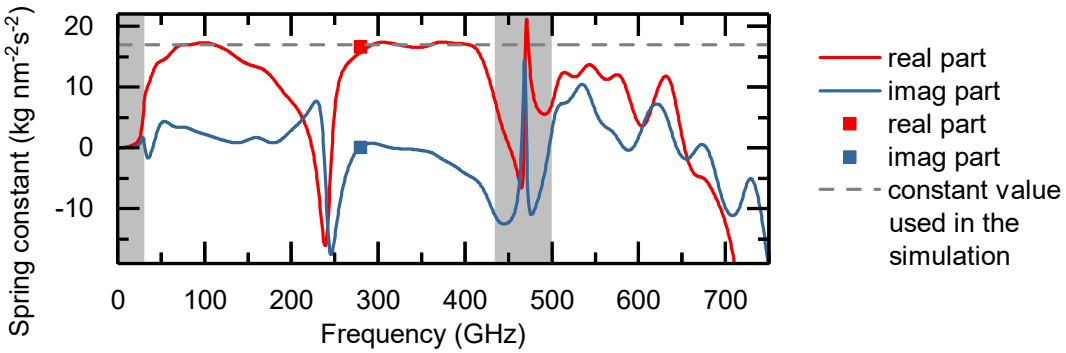

Figure 6.15.: The evaluated spring constant from the measured spectral transfer function STF given by the ratio of the first two pulses. The other parameters for the evaluation are given in Table 6.2. red: real part, blue: imaginary part. The solid line corresponds to the extraction from STF_{exp} and the empty circles correspond to the advanced extraction from the oscillation in the beginning of the measurement. The dashed gray line depicts the spring constant value from Table 6.2. The gray areas mark regions with a very low spectral amplitude of the echoes 1 and 2.

6.3.5. Extraction of the spring constant

Nevertheless, the approach so far assumed a constant spring constant. This does not have to be necessarily true. It is possible to extract the spring constant from the STF by solving Eq.(6.4) for η. Inserting the experimental STF yields:

$$\eta = i\omega Z_{\mathrm{Al}} \left[\frac{1 + e^{2ik_{\mathrm{Al}}h_{\mathrm{Al}}}}{1 - e^{2ik_{\mathrm{Al}}h_{\mathrm{Al}}}} - \frac{Z_{\mathrm{Al}}}{Z_{\mathrm{Si}}} \frac{STF_{exp} + P_{\mathrm{Si}}}{STF_{exp} - P_{\mathrm{Si}}} \right]^{-1} \tag{6.5}$$

The evaluated spring constant is dependent on the assumption of the adhesion in Al and Si. In Fig. 6.15 the spring constant is plotted evaluated with the values given in Table 6.2 and from the spectral transfer function from Fig. 6.13(b).

Neglecting the gray marked areas and higher frequencies, the extracted frequency-resolved spring constant has values which are nearly equal and in good agreement with η_{STF}. However, a pronounced dip is present between f_0 and f_{Al} ranging down to 150 GHz. A comparison of the calculated STF with the measured STF (see Fig. 6.13) shows a deviation between the phases of both at exactly the looked at frequency range between 150 to 300 GHz. Thus, the pronounced dip in Fig. 6.15 seems to be a numerical artifact due to the non-perfect modeling of this system. A variation in adhesion over the measured optical spot sizes or a thickness variation of the Al film might give rise to this effect. The extraction of the spring constant seems to be a good measure for the quality of the modeling.

It should be noted that by this approach also a complex spring constant can be derived, depending on the adhesion chosen for Al and Si. In principle, the scattering at the interface could be described by an imaginary spring constant. However, when including a complex spring constant, the fit of the STF and the simulated data does not improve, although an additional parameter is introduced. This indicates that damping at the interface and can be neglected, or is already included in the simple attenuation behaviors.

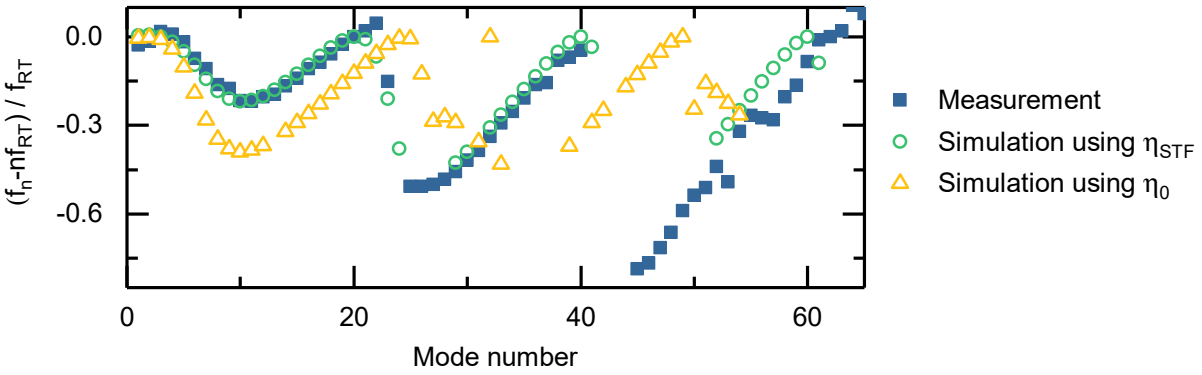

Figure 6.16.: Modes deviation from a linear slope $n \cdot f_{\mathrm{RT}}$ plotted over its mode number n. The deviation is scaled with the fundamental - undisturbed - mode frequency f_{RT}, corresponding to the inverse round trip time in the bilayer (blue squares). The numerical extracted theoretical predictions uses the values in Table 6.2 (green circles) and h_0 and η_0 obtained from the oscillation in the beginning (yellow triangles). Note the strong modulation compared to Fig. 6.7 in the case of perfect adhesion.

Furthermore, the spring constant can be extracted from the measurement of the oscillation in the beginning of the measurement data. Eq. (6.5) has to be changed accordingly (meaning $STF_{exp} \to \infty$) which corresponds to no acoustic pulse incident on the Al film. Inserting f_0 and τ_0 obtained from the fitting regime allows to extract the spring constant at the frequency f_0. The obtained result is shown in Fig. 6.15 matching very well with the spring constant in Table 6.2 and evaluated from the STF. It shall be mentioned that this result and the agreement of all extraction techniques is strongly dependent on the attenuation of the Al and, therefore, corroborates the extracted dissipation.

6.3.6. Adhesion-induced frequency shift

In Section 2.6 it is predicted that a bilayer system with a non zero reflection coefficient at the interface will show a modulation of the eigenmode frequencies and its higher harmonics around a linear trend. This is shown in Section 6.2 for a perfectly adhered bilayer due to reflection induced by the impedance mismatch. A sinusoidal modulation with the maximum change of 3 % is found. In the following it will be shown that the increased reflection due to weak adhesion shows a more intense modulation.

The normalized deviation of each modes frequency from the linear slope $n \cdot f_{\mathrm{RT}}$ over mode number n is plotted in Fig. 6.16. The normalization was done by dividing with the ground mode frequency f_{RT}, which can be calculated by the inverse round trip time of the bilayer system, given by the values in Table 6.2. A complex modulation below zero (zero defining the linear relationship) is apparent. It follows roughly a $-n \sin^2 ... n$ behavior with asymmetric minima shifted to lower mode numbers. A modulation above 75 % from the expected linear relationship can be seen - far larger than in the case of perfect adhesion.

In Section 2.6 the bilayer eigenmode equation is derived. It can be solved analytically for small modulations below 10 %, but for higher changes it has to be solved numerically. Using the values given in Table 6.2 the solution of Eq. (2.45) is shown in Fig. 6.16. A good agreement

in amplitude and period of the modulation is found. A detailed analysis shows that the period is given by: $N_{\text{modulation}} = (2 + 2t_{\text{Si}}/t_{\text{Al}})$. The missing points in the theoretical solution are due to diverging values in the numerical treatment. As can be seen in Fig. 2.13 the amplitude and distortion of the modulation is non linearly dependent on the spring constant, which is thus a very precise measurement of corroborating the obtained findings. This is also seen by the strong deviation of the values obtained by the extraction with the parameters from the oscillation in the beginning.
Furthermore, these findings explain, why the dip around $f_0 = 280\,GHz$ in the STF (see Fig. 6.14 (c)) shifts to lower frequencies for weaker adhesion. A lower adhesion leads to a stronger negative modulation of the eigenmode's frequency and thus a red shift of the mode.

6.4. Conclusion

To summarize this section, broadband acoustic frequency combs in the 100 GHz frequency range were generated, detected, and discussed. Defined by the round trip time in the acoustic cavity made up by an Al film on a Si membrane its fundamental mode and its higher harmonics are excited. The combs are spanning over up to 6 octaves including 9-45 well separated modes. For one layer the higher harmonics are perfect integer multiples, while for a bilayer, due to the different mechanical properties of the layers, a modulation around the linear relationship is expected and observed over one period. The short round trip times in the system allow to detect up to 13 individual acoustic pulses after excitation. Because the pulses can be clearly isolated, their individual spectra can be extracted. Fitting the amplitudes at each frequency with an exponential decay, frequency dependent lifetimes for the bilayer are obtained. These lifetimes are shorter than values found in measurements of bare Si-membranes and, thus, an increased amount of extrinsic dissipation is assumed.
It is shown that a weakly adhered Al/Si bilayer system can be precisely modeled by a coupling of both layers with a spring. 5 quantitative parameters are extracted: both thicknesses and attenuations and the spring constant. The measured spectrum consists of frequencies from few GHz to 800 GHz, over which the phonon lifetimes in Si proportional to $1/\omega$ are yielded. For the spring constant $\eta_{\text{Al-Si}} = 17\,\text{kg}\,\text{nm}^{-2}\text{s}^{-2}$ is obtained, while the lifetime of an acoustic phonon in polycrystalline Al with the frequency $f_{\text{Al}} = 240\,\text{GHz}$ is found to be $\tau_{\text{Al}} = 68\,\text{ps}$. The results show that the usual approach to neglect dissipation while extracting adhesion parameters in ultrasonic measurements causes considerable deviations from the precise evaluation. Therefore, it has to be included for quantitative measurements. Furthermore, this approach simplifies the characterization of bilayer systems due to the development of an approach, which does not need advanced knowledge about the excitation and detection processes of the acoustic sample.

Chapter 7

Hypersonic Lamb waves

7.1. Introduction

Lamb waves are guided acoustic waves between the surfaces of a plate, e.g. a membrane. Membranes become increasingly interesting for the high-tech industry, as the intrinsic pathways in these structures promise a convenient fabrication of devices utilizing those pathways [Rog11]. Additionally, Lamb waves are utilized for structural health monitoring of thin plates and shells - being an integral part of an aircraft [Wev06]. Therefore, techniques and methods for the characterization of their parameters and quality are needed. Here, the dispersion relation and attenuation in Si membranes will be analyzed for acoustic waves at GHz frequencies.
Previously, it was shown that on nanopatterned [Bon01, Sch12, Li12] bulk Si Rayleigh waves up to 90 GHz could be generated and detected with the ASOPS technique [Sch12]. Mainly, the scattering of high frequency parts into the bulk limited the propagation length (for dissipation processes see Section 2.7.1). To circumvent these losses, here, a second surface in the vicinity of the front surface is facilitated, e.g. a Si membrane is used. The reflection of the radiated phonons leads to new boundary conditions and to guided waves in the membrane, e.g. Lamb waves, of which Rayleigh waves are a special case. This enables the detection of higher frequencies up to 197 GHz.

7.2. Experimental results

The general layout is shown in Fig. 7.1(a). On a crystalline Si membrane of 326 nm thickness, rectangular stripes with different widths between 50 nm and 1.5 µm are etched and the grooves are filled by Al evaporation. The non-etched parts are covered by a protection layer of PMMA. Details regarding the fabrication of the membranes and the stripes are given in Section 4.2. Al gratings with periods between 100 nm to 500 nm and a total width of 15-20 µm and unique detection stripes at distances larger than 5 µm are fabricated. The stripes are oriented perpendicular to the [110]-direction on the (001)-surface of Si with a filling fraction of 50 %. This means half of the grating area is covered with Al and the other half is untreated Si. The stripes are partly (3-5 nm) embedded in the membrane and have a total thickness of 17 nm as was determined by ellipsometry on a larger evaporated area next to the gratings. A 2D sketch of the sample along the (001)/(110)-plane is shown in Fig. 7.1(b).
As pump and probe polarization are perpendicular to each other a careful choice of the grating orientation is crucial. Previously, the strongest excitation of Lamb waves was found to be with

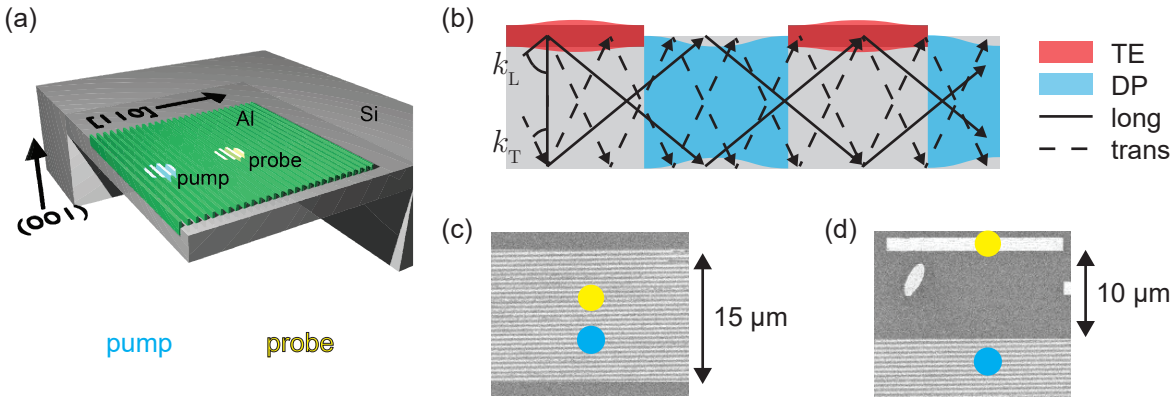

Figure 7.1.: (a) Pump-probe scheme of the measurement on a thin Si membrane with an Al grating. Pump and probe pulses are laterally displaced and the crystal orientation is depicted. (b) Excitation and propagation scheme of the structure. The Al is expanded by thermoelasticity (TE) and the Si is contracted by deformation potential (DP). The longitudinal and transverse phonons create the Lamb wave. (c) Excitation and detection on a grating without discontinuity. (d) Excitation on a grating and detection on a single 1.5 µm-wide stripe.

the pump polarized orthogonal to the stripes and the probe polarized parallel to the stripes [Gro11]. One can understand the increased excitation in a simple picture by the increased scattering of electrons excited in the vicinity of an edge of the stripe and, therefore, an increased relaxation of the excited electrons. Contrary to the generation, the detection is dependent on the photoelastic properties of the Al stripes and the stripes work as antennas upon parallel polarized illumination. This leads to an increased sensitivity.
By exciting the grating with an optical pump pulse of 780 nm wavelength and a power of 20 mW the Al will expand due to thermo-elastically generated stress and the non-shadowed Si will contract due to stress generated by deformation potential (for the explanation of the physical mechanisms see Section 3.2). As the excitation is done from the Al side of the membrane, most of the light will be absorbed by the Al and only a small part will propagate in the shadowed Si below [Ant02]. The spatial periodic expansion of the Al metal stripes and the compression of the Si bars leads to distinct Lamb waves with the wavelengths determined by the grating period (see Fig. 7.1(b)). The sub-wavelength metallic array will lead to a complex near-field electrical field, which should be taken into account for a detailed analysis [Bar02, Ste03]. The change of the optical properties is detected with a probe of 820 nm wavelength and a power of 3.5 mW. Details regarding the measurement setup are given in Section 4.1.
In Fig. 7.2(a) the measurement on 5 different gratings (100-500 nm period) with pump and probe spot spatially overlapping are shown. The electronic background with a maximum of the electronic peak of $\approx 10^{-3}$ is already subtracted for all samples. Please note that the scale for the 200 nm grating is larger by a factor of 5 compared to the other samples, which hints to a change in the pump power in this measurement, as the measured DC-level is similar for all samples. As no quantities between the individual gratings will be compared, this will be no problem in the following. In the measurement one sees oscillatory components, which correspond to coherently excited acoustic phonons representing guided acoustic eigenmodes of the membrane. In Section

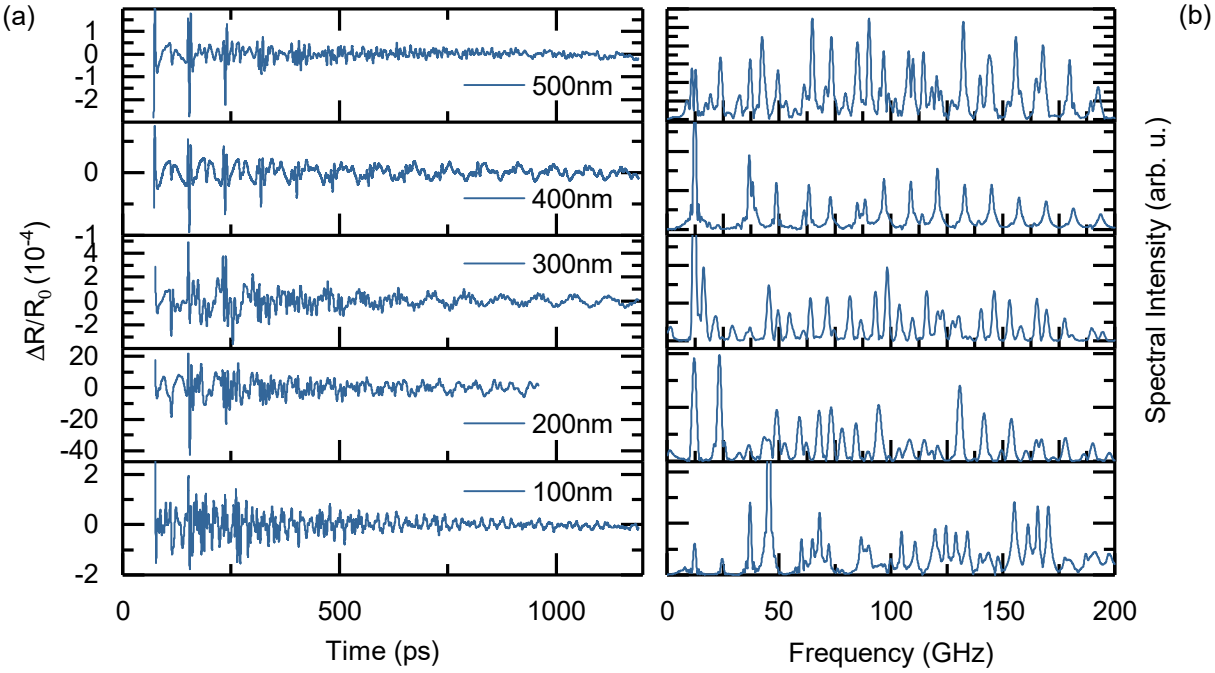

Figure 7.2.: (a) Time-resolved modulation of the reflected probe beam $\Delta R/R_0$ of gratings with 100-500 nm period and oerlapping pump and probe spots. (b) Fourier spectra of the different time transients.

2.4 the corresponding plate modes are introduced. Their measured frequency spectra are shown evaluated from the Fourier transformation of the temporal data in Fig. 7.2(b). In the spectra with both pump and probe spatially overlapping a dense frequency distribution is seen. This is due to the detection of standing waves along the depth direction and of propagating waves along the membrane perpendicular to the stripes. In the Sections 6.2 and 6.3 the phonon dynamics of the standing waves for the Si membrane with perfectly and weakly adhered Al films are discussed explicitly. In this chapter the discussion is narrowed down to propagating Lamb waves.

To distinguish propagating from non-propagating waves pump and probe spots can be spatially displaced one relative to another. By changing the entrance angle in the microscope objective the laser spots in the focal plane change their position up to a distance of 30 µm without distorting the spot quality too much. This has been measured via DC-level measurements of the probe spot with changing spot positions.

Fig. 7.3(a) shows the measurement on the same 5 gratings as before (with 100-500 nm period) but pump and probe spots are separated by 6-10 µm, which is 3-5 times the spot size. In contrast to the measurement with overlapping spots, no data editing has been done. The electronic contribution is barely visible due to the limited diffusion of hot electrons < 5 µm. Note a change in the amplitude of $\Delta R/R_0$ by two orders of magnitude between the overlapping and separated beams. Details regarding experimental hot electron diffusion in thin Al films on Si membranes can be found in the Master thesis of Matthias Klingele [Kli13]. In the measurement oscillations with different frequency components and a Gaussian-like amplitude envelope are visible. The envelope stems in first order from the optical Gaussian excitation and detection profiles. The

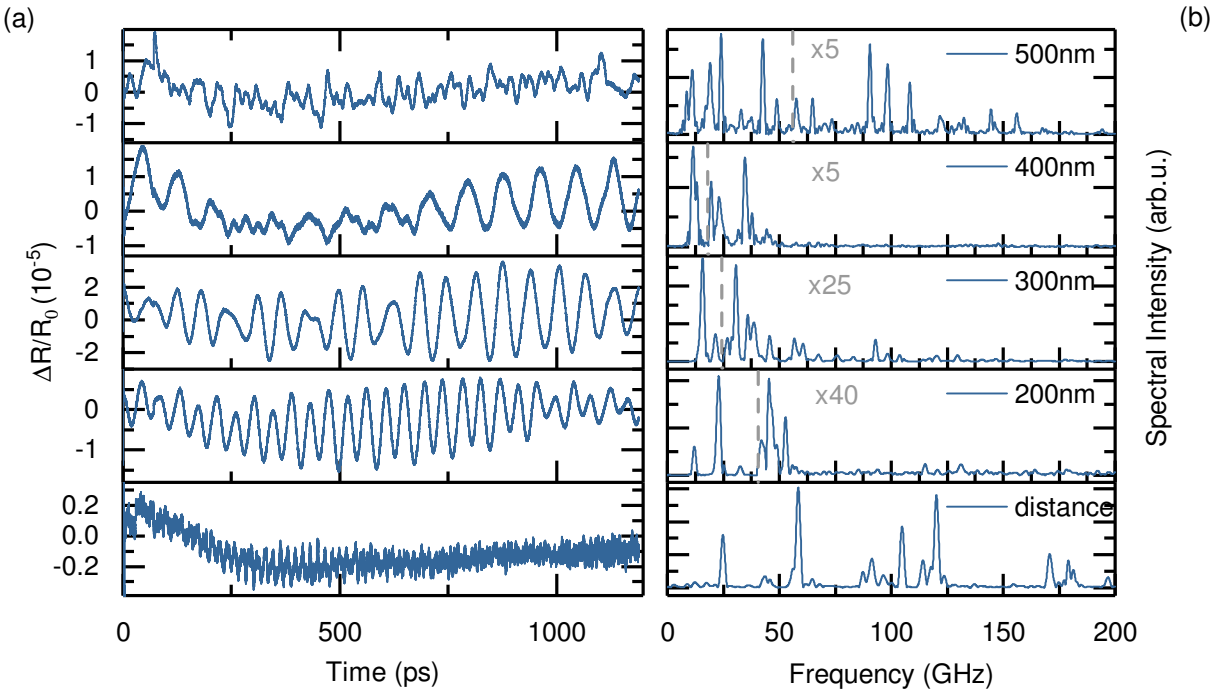

Figure 7.3.: (a) Time-resolved modulation of the reflected probe beam $\Delta R/R_0$ of gratings with 100-500 nm period and pump and probe spot separated between 6 and 10 µm. (b) Fourier spectra of the different time transients. Note the zoom for higher frequencies at the larger period gratings.

center of the wavepackets is distributed seemingly arbitrarily along the time window. But one has to keep in mind that due to the high repetition rate of the lasers (800 MHz) the measured signal stems from a preceding pump pulse at a multiple of the inverse repetition rate (1.25 ns). Thus, the given time is not absolute but relative to the absolute time modulo the inverse repetition rate. From the temporal difference between the center of the wavepackets, one can deduce the different propagation times given by the different distances between pump and probe spots or the different group velocity of the wavepacket. This will be discussed in detail further below.

7.3. Dispersion relation

In Fig. 7.3(b) the Fourier spectra of the propagating Lamb modes of the different gratings are shown. The spectra show a strong change of the amplitude ratios of different spectral components and a less dense mode spectrum compared to the overlapping spectra. Up to 21 unique peaks are visible per measurement. As it was previously observed for Rayleigh waves on bulk Si, the generated and detected frequencies are assumed to be defined by the inverse grating period [Sch12]. All observed frequencies are shown in Fig. 7.4 for three different wave vectors, i.e. their inverse grating period: the basic grating period, the first even harmonic and the first odd harmonic. Given the fact that the grating is not sinusoidal in period but rectangular and the initial stress distribution will not be sinusoidal, a Fourier analysis expects additional higher frequencies to be excited at odd harmonics. Furthermore, defects in the grating periodicity will

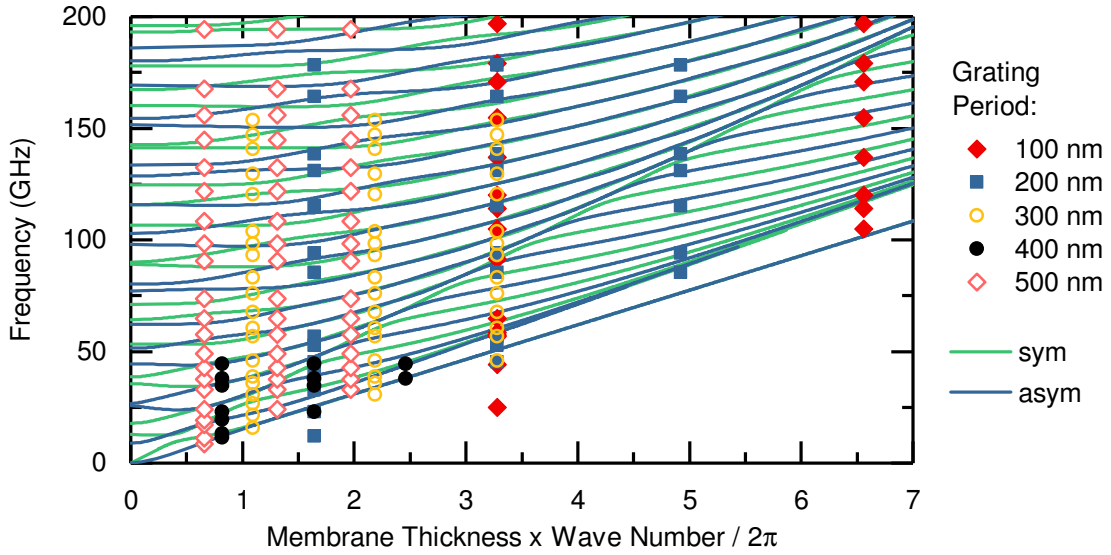

Figure 7.4.: Dispersion relation of Lamb modes in a thin Si membrane in the [110]-direction. Green lines mark the symmetric modes (sym) and blue lines the asymmetric ones (asym). The data points correspond to the first, second and sometimes third harmonic of the grating period (left to right) and the corresponding measured frequencies of the different gratings.

lead to even harmonics of the grating period.
Together with the measured frequencies the dispersion relation for Lamb waves in Si membranes along the [110]-direction, which was derived in Section 2.4, is shown in Fig. 7.4. First, only those modes are discussed, where the frequency is plotted over the basic wave number and not a higher harmonic. Although the frequency spectrum given by the dispersion relation is very dense, most of the measured frequencies can be clearly assigned to a mode given by the Lamb dispersion. Slight discrepancies can be explained by the measurement system: the gratings are excited with 800 MHz and because of time delay in the beginning of the measurement this limits the frequency resolution to around 1 GHz. Additionally, the exact value of the wave number is broadened due to the limited stripes illuminated per grating. As the FWHM of the pump spot is less than 2 µm the wave packet exhibits a finite length. This broadening is reduced for smaller grating periods as more stripes are illuminated in the laser spot. Furthermore, the fabrication process gives both a variation in grating period and membrane thickness (±5 nm), leading to an increased error for smaller grating periods. By including both contributions a simulation leads to a nearly homogeneous error of 5-6 % for the wave number of every grating period. At last, weak phononic effects should be expected based on the different mechanical properties of Al and Si. While the Al grating allows the excitation of ultra-high frequency modes in a simple manner, it may also affect the dispersion relation due to mass loading, different speeds of sound, and different impedances. The difference in the longitudinal impedances of Al and Si is negligible, but the difference in shear impedances is significant (see Table A.1). However, as the thickness of the Al is 5 % of the Si thickness this effect should be quite small. Indeed, it was demonstrated earlier that for Rayleigh waves in bulk Si, where the surface penetration depth is only 5 times larger than the Al thickness, the frequency shift is not larger than 10 % [Sch12]. As Lamb waves

are guided by the complete thickness of the membrane (324 nm) this shift should be smaller and one expects the frequency modification not to exceed 5-6 %. Nevertheless, these effects should be taken into account if a precise identification or modeling of the individual Lamb modes is necessary.
There are some frequencies, however, that cannot be attributed to a frequency given by the dispersion relation in the vicinity of the basic wave vector. Those frequencies can be attributed to the higher harmonics. This can be shown with the highest measured frequency: 196.8 GHz on the 100 nm grating. This is close to the theoretical frequency of 196.3 GHz of the 15th asymmetric Lamb mode at the second harmonic of the grating period. The nearest frequency obtained by the theory for the basic grating period would be 192.1 GHz of the 19th symmetric Lamb mode instead. The second harmonics means a wavelength of this mode of 50 nm.
Additionally, there are some modes below the frequency of the lowest branch in the dispersion relation, which cannot be explained by the assumption of the harmonics so far. Those can be explained by the spatial width of the pump laser spot, the FWHM is $< 2\,\mu m$, which excites Lamb waves with that wavelength convoluted with the grating stripes. These modes have a wave number far below the grating wave number itself. One can see in Fig. 7.4 that at low wave numbers those low frequency modes fit perfectly to the dispersion relation
Because it is not straightforward to distinguish the measured modes to be symmetric, asymmetric, or a higher harmonic with this kind of measurement setup, here shall not be assigned any mode to an individual wave number, but the reader is free to check the agreement for him-/herself. Therefore all frequencies are plotted for every harmonic of their wave number.
Some expected modes are missing in the spectra and so far the intensity distribution is not explained. These features can be attributed to the mutual compensation of the different contributions to the detection process. Those two processes are the photoelastic detection in the Al and Si and the interferometric detection in the Si membrane, which are discussed in detail in Sec. 3.7. Mechri et al. demonstrated that the optical detection process of confined eigenmodes can be either enhanced or reduced to zero following certain selection rules [Mec12]. In particular, they showed that certain detection configurations exist where the coherent acoustic phonons and probe light sensitivity functions are orthogonal, which leads to a cancellation of the photoelastic detection mechanism.
However, it is possible to explain some of the largest amplitudes. For example, in the spectrum of the 100 nm grating the mode at 58 GHz has the largest amplitude. By looking at the dispersion relation, one sees in the vicinity of this frequency at the given wave number two Lamb modes close together. The superposition of both might enhance the amplitude. It may be noteworthy that this frequency at the given wavelength of 100 nm corresponds perfectly to a transverse acoustic wave in bulk Si with the phase velocity of 5840 m/s.

7.4. Determination of the decay length

The possibility to change the probe distance in respect to the pump allows to measure the spatial decay and speed of sound of individual phonons in dependence of the distance. For the 100 nm grating in the two Figures 7.5(a) and (b) the frequency spectra of two distances, 6.8 and 7.8 µm respectively, are shown. Slightly different amplitudes are visible. By comparing those amplitudes the damping distance can be extracted. This is shown further below. First, the measurement of the speed of sound will be discussed.

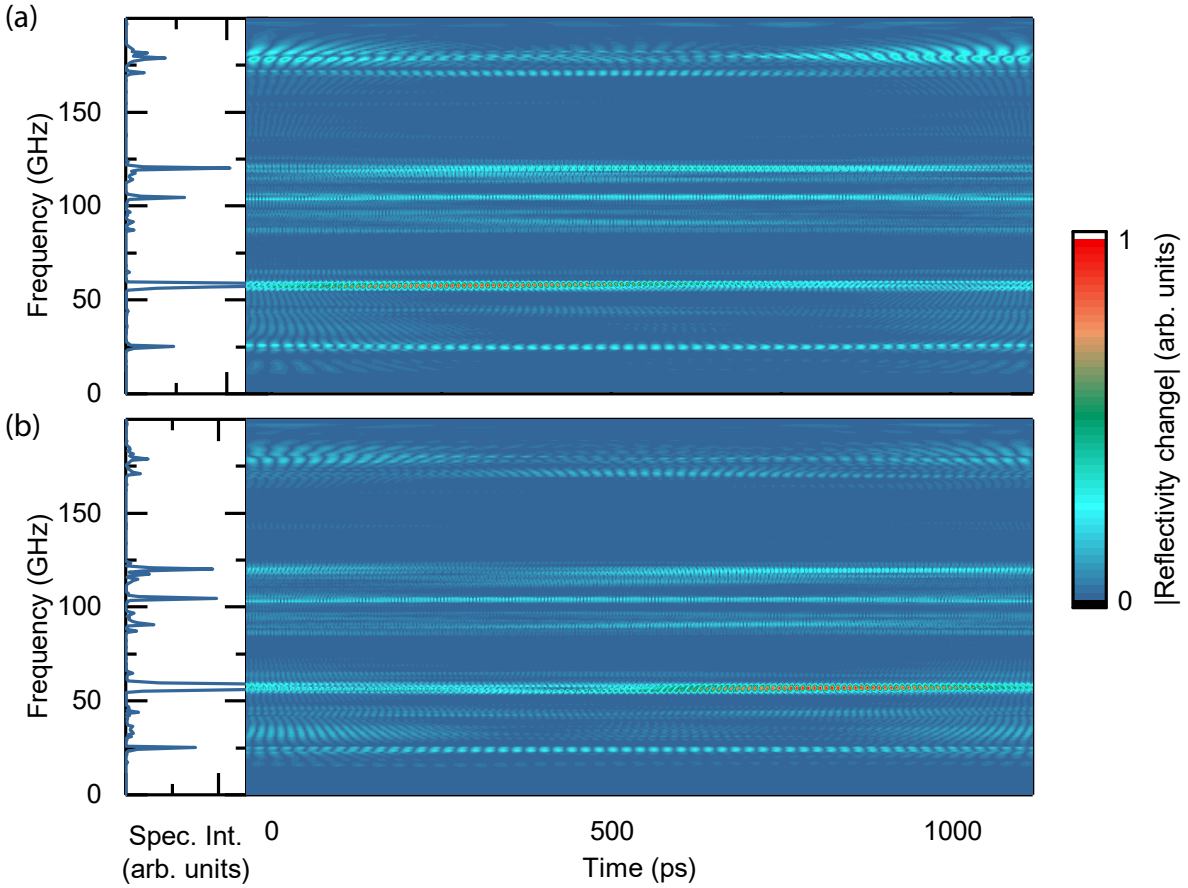

Figure 7.5.: (a) Time-resolved modulation of the individual frequencies of the 100 nm grating with the separation of 6.8 µm and (b) 7.8 µm between pump and probe spot. Details regarding the evaluation are given in the text.

On the right side of the Figures 7.5(a) and (b) the time signal is shown sorted by frequency. This has been accomplished by a Fourier transformation of the whole time transient and doing inverse Fourier transformations for spectral windows of 4 data points each time swept along the whole frequency spectrum. The 4 data points frequency window was chosen because it showed the best contrast in the two dimensional plot. The highest amplitude is mainly present at the modes with frequencies around 58 GHz, which was explained earlier due to the presence of two dispersion branches in close proximity at that frequency. The wavepacket is strongly localized for both measurements with a maximum at 380 ps and a FWHM of 400 ps for the shorter distance and a maximum at 820 ps with a FWHM of 400 ps as well for the larger distance. Calculating the temporal difference between the two maxima yields the additional propagation length, which the acoustic wave packet needs to travel in the membrane from the pump to the probe spot. With a 1 µm spatial distance and a 440 ps time delay one obtains for the group velocity: 2270 m/s. This means the acoustic wave packet needs for the 6.8 µm distance from excitation to detection 3 ns. Subtracting the measured central position of 300 ps (380-80 ps as one has to adjust for the time zero), the time window multiple should be 2.7 ns, which is in good agreement with two times

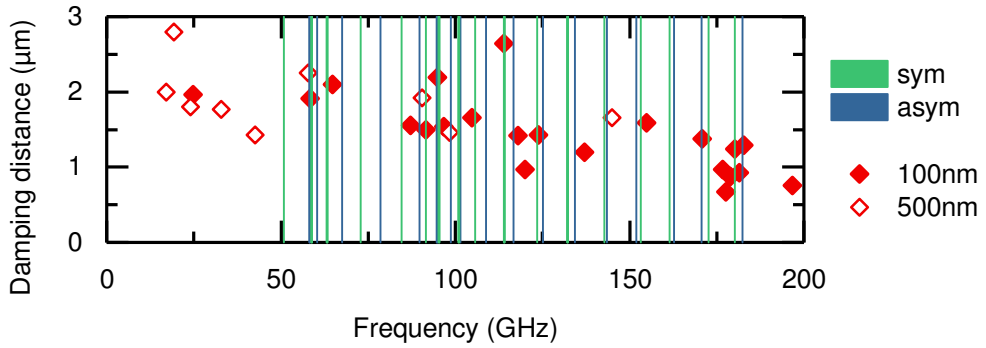

Figure 7.6.: The damping distance over frequency is plotted for the 100 nm and the 500 nm grating and the expected frequencies given by the Lamb dispersion relation are shown by vertical lines (for symmetric modes in green, for antisymmetric in blue).

the time windows of 2.5 ns.
Using this group velocity for the wavepacket one can calculate the spatial FWHM from the temporal FWHM of the wavepacket to be 910 nm. This FWHM is the convolution of the generation and detection profiles. Assuming an identical Gaussian profile of both laser spots, one can deconvolute this width by multiplying with $\sqrt{2}$ and obtains for the spots a FWHM of 1.3 µm. This is well below the nominal 2 µm assumed earlier, but also well above the diffraction limit of light at 800 nm wavelength and, thus, in the expected range.
In Figure 7.6 the damping distances for the individual modes of the 100 nm and 500 nm grating are shown along the frequencies given by the dispersion relation. The damping distance, i.e. the distance over which the respective frequency's amplitude reaches $1/e$, is evaluated by fitting the peak maxima of two spectra evaluated at different distances with an exponential decay. For both structures a similar frequency dependent damping behavior can be seen. For the lower frequencies damping distances around 2 µm are found, while for the higher frequencies lower damping distances around 1 µm are found. Possible dissipation mechanisms for Lamb waves are discussed in Sec. 2.7.1, but won't be quantified here.

7.5. Detection processes

To investigate the detection process more closely, besides the detection on a grating the detection on a 1.5 µm wide Al stripe is tested. This width was chosen to be large enough, but still smaller than the FWHM (< 2 µm) of the probe spot. It is deposited 10 µm away from the grating. To compensate for larger losses because of the larger distance between pump and probe spots, the pump power was changed to 30 mW and the probe power to 15 mW. The excitation is done identical to above on an Al grating with 100 nm grating period. Because both excitation gratings were not produced in the same fabrication process, first the qualitative agreement of the excited modes is compared. In Fig. 7.7(a) the spectra for pump and probe spots overlapping on the two nominally identical gratings are plotted. One sees the main spectral characteristics to be well reproduced at the frequencies of the propagating Lamb waves above 50 GHz.
Next, the spectrum with detection on the 100 nm grating with 6.8 µm distance between pump and probe spots is compared to the spectrum with detection on the single stripe. Here, the

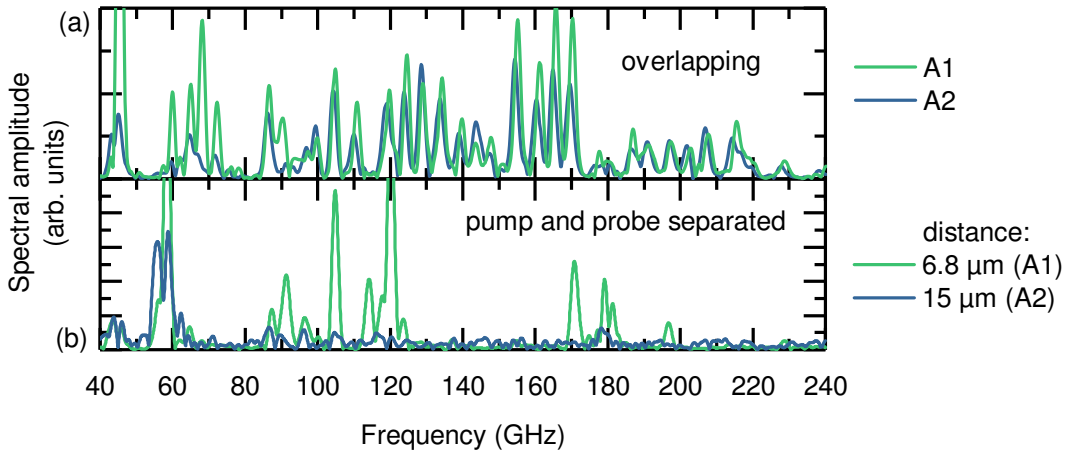

Figure 7.7.: (a) Fourier spectra of the measurements with pump and probe spots overlapping on two nominally identical 100 nm gratings (the previous described sample A1 and the new A2). (b) Fourier spectra of the measurements excited at the same position but probed (A1) 6.8 µm separated on the grating and (A2) on a 1.5 µm wide single stripe deposited in 10 µm distance parallel to the grating with 15 µm distance to the pump spot.

propagation distance is 5 µm along the grating and 10 µm along the bare membrane. Both spectra are shown in Fig. 7.7(b). In the single stripe measurement high frequency modes are weakly to not detected. As the damping distances for the different frequencies change with a factor of two in the looked-at frequency range and the amplitude of the modes at 58 GHz is still large, this indicates that the metallic grating enhances the optical detection especially of high frequency Lamb modes.

So far, the generation of a certain wave vector was imprinted in the strain profile by utilizing a grating. The detection was accomplished on a grating or on a single stripe. For completeness the generation on a single stripe and detection on different stripes has been investigated as well. The generation was done on a 1.5 µm wide stripe and the detection was done on different stripes with distances up to 55 µm. In Fig. 7.8(a) the relative reflectivity changes are shown for generation and detection on a single 1.5 µm wide stripe, detection on a 3 µm, at 20 and 37 µm distance, and detection on a 5 µm wide stripe at 55 µm distance. A small electronic peak is still visible at 20 µm, but vanishes for larger distances. Contrary to the expected damping evaluated earlier, at 55 µm there is still a pronounced signal visible. In Fig. 7.8(b) the spectral intensities of the Fourier transformation are shown. In the measurement of the pump and probe spots overlapping, one expects to detect the most signal from the standing waves between the front and backside surfaces. The two areas, the bare membrane and the stripe, will allow to generate and detect a super position of both the membrane's oscillation and the frequency comb below the stripe. As the modes of both processes, are lying next to each other, this superposition only becomes apparent for higher harmonics, i.e. around 58 GHz, where a double peak structure appears, peaking at 57.5 GHz (the frequency comb mode) and 59 GHz (the Si membrane's mode). Noteworthy is the very high amplitude of the mode at 35 GHz. This mode is also pronounced in the distance measurement, where otherwise only low frequency components

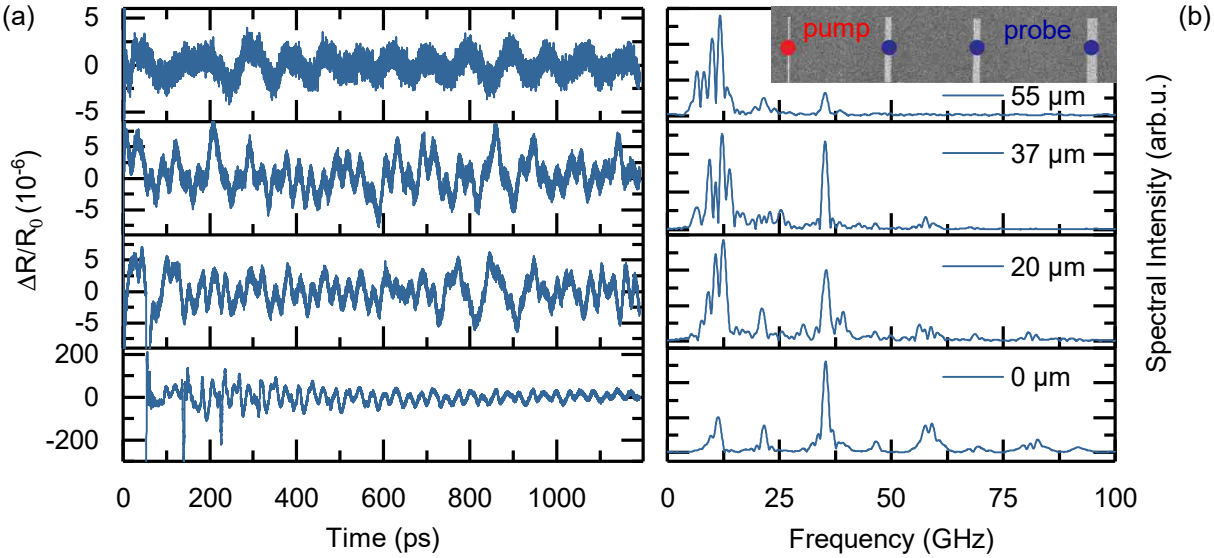

Figure 7.8.: (a) Time-resolved modulation of the detection on a single 1.5 µm wide stripe with pump and probe overlapping, detection on a 3 µm wide stripe, at 20 and 37 µm distance, and detection on a 5 µm wide stripe at 55 µm distance (b) Corresponding Fourier spectra.

are visible. Compared to the overlapping measurement, additional low frequency components between 6 to 12 GHz appear. They are assumed to be a result of the larger excited wave vector (stripe width: 1.5 µm) and its higher modes. The origin of the high amplitude and of the diversity of the low frequency modes is not clear and further investigations are recommended. It shall be noted that a detection with the probe on the bare Si membrane does not yield any detectable signal of coherent phonons.

7.6. Conclusion

In this chapter nanostructured Si membranes were used to generate and detect hypersonic Lamb waves propagating up to 55 µm in distance. Lamb modes with frequencies up to 198 GHz could be detected and wavelengths down to 50 nm could be reached. The comparison with Rayleigh waves on bulk Si yields the opportunity to obtain higher frequencies with the same spatial modulation. Although the Al grating is mechanically not negligible, because it allows for the generation and detection, the dispersion calculated for a bare Si membrane is only weakly disturbed. The possibility to measure with a spatial distance allows to extract damping distances for different grating periods.
Maznev showed that for certain conditions of longitudinal and transverse speed of sounds, a Dirac-like cone can be obtained in the dispersion relation [Maz14]. By tuning the relative thicknesses of the Al and Si layers, or the propagation direction, new properties arise, leading to the generation of high harmonics [Eve16]. Furthermore, the process of generating distinct wave vectors allows for the characterization of phononic crystals and new sensing applications, especially in the case of liquid loaded membranes [Ver06, Kar07, CM10, San11, Büy13, Deh15].

Chapter 8

Tin diselenide

8.1. Introduction

2D layered materials are of great interest for basic and advanced technologies. Since the discovery of graphene in 2004 much research has been done to investigate its properties due to its special nature as monoatomic layer shape [Nov04]. Very good in-plane electricity and heat conduction occurs, allowing for the measurement of quantum effects, the building of nanosized electronic components and nanoscopic sensors [Sny08, Her13, Zha14]. Apart from graphene, a wide variety of 2D materials has been discovered or rediscovered, of which the IV-VI semiconductors attracted broad attention [Zho16]. They are promising candidates for thermoelectric materials, i.e. converting waste heat into electrical energy [Bel08, Vin10]. Here, the indirect bulk semiconductor hexagonal tin diselenide ($SnSe_2$) is investigated. The hexagonal unit cell is of a D_{3d} type and the layered structure is shown in the inset of Fig 8.1. Every Se atom forms a trigonal pyramid with the base of covalently bonded Sn atoms [Had13]. The stacked 2D layers of the bulk are bonded by comparably weak Van-de-Waals forces. The band gap lies at 0.9 eV for bulk and around 1.7 eV for single sheets [Paw16]. The anisotropy leads to a high electron mobility in the sheet's plane and a very low electron mobility between the sheets. Due to the weak coupling between the sheets, heat conduction is remarkably low. The first acoustic studies were conducted in 1977, measuring the acoustic phonon dispersion curves by inelastic neutron scattering [Bre77]. The first optical phonons were measured in 1976 by Raman spectroscopy [Luc76]. Here, the first time resolved measurements on $SnSe_2$ determining acoustic and optical phonon lifetimes are presented.

8.2. Experimental results

The sample is excited at a wavelength of 780 nm with 10 mW and probed at a wavelength of 820 nm with 1 mW. The pump and probe spots are focused town to below 2 µm with the pulse width below 70 fs at the samples position due to the use of a prism compressor for both beams [He15]. To increase the time resolution a repetition rate offset of 2 kHz is chosen. However, due to limited memory of the oscilloscope, this limits the window to 950 ps. The sample is measured with the laser light parallel to the c-axis, and perpendicular to the $SnSe_2$ sheets. In Fig. 8.1(a) the relative reflectivity change is shown. After a sharp rise at excitation due to the hot electron system, a fast decay is visible, upon which moderate oscillations follow. In the inset the electronic contribution is subtracted and a fast decaying and high-frequency oscillation

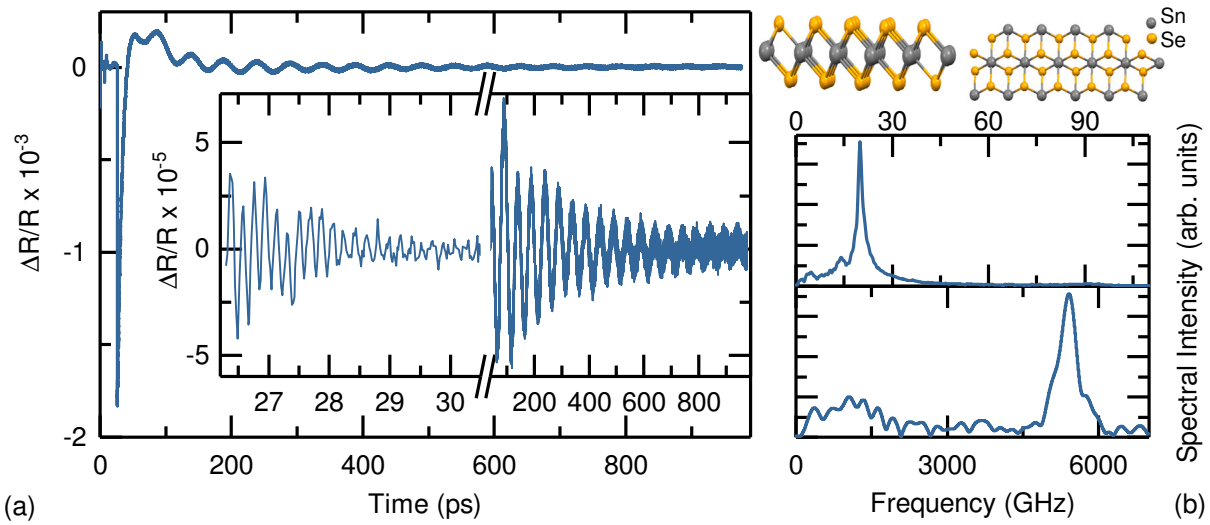

Figure 8.1.: (a) Relative reflectivity change of a $SnSe_2$ sample illuminated perpendicular to the sheets, c $\perp$ surface (the structure of $SnSe_2$ is shown in the top right, taken from Ref. [Paw16]). The inset shows the signal without electronic background for two different time regimes. A fast oscillation in the beginning, decaying after a few ps and a slower oscillation over the whole time window. (b) Fourier transformations of the two different time regimes. The top window shows the spectrum of the latter oscillation, while the bottom window belongs to the first oscillation. The different time scales transfer to different frequency scales by 2 magnitudes.

directly at the excitation time becomes apparent showing a beating signal with an amplitude similar to the slower oscillation. Both oscillations show an exponential decay after a few periods. The Fourier transformations of both oscillations are shown in Fig. 8.1(b) and show one frequency each. The first oscillation has a frequency of 5.40 THz, whereas the latter one peaks at 20 GHz.

8.2.1. Acoustic phonons

First, the origin of the 20 GHz mode will be discussed. In Section 3.7.2 the origin of the Brillouin scattering was explained. The probe light is reflected at the surface of the sample and at the acoustic pulse generated at the surface of the sample. The acoustic pulse propagates with the speed of sound into the sample and both reflected light components interfere with a sinusoidal modulation in time. The measured frequency is calculated to be (see Eq. 3.26):

$$f_{\text{Brillouin}} = \frac{2nv_{\text{L}}}{\lambda}, \tag{8.1}$$

with $n = 3.55$ the refractive index of $SnSe_2$ [Eva69], $\lambda = 820\,\text{nm}$ the probe wavelength, and v_{L} the longitudinal speed of sound in $SnSe_2$. This gives for the longitudinal speed of sound: $v_{\text{L}} = 2310\,\text{m/s}$, which corresponds well with the measurements of Brebner et al., who extracted a speed of sound of $v_{\text{L}} = 2150\,\text{ms}$ from the elastic modulus of $C_{33} = 27.6\,\text{GPa}$ [Bre77]. By fitting the oscillation with an exponentially decaying sine, one gets for the lifetime of the Brillouin oscillation: 228(1) ps. With the extracted speed of sound this gives a damping distance of

Table 8.1.: Extracted frequencies and lifetimes of the Brillouin and Raman (A_{1g}) modes.

pump (mW)	probe (mW)	$f_{\text{Brillouin}}$ (GHz)	$t_{\text{Brillouin}}$ (ps)	f_{Raman} (GHz)	t_{Raman} (ps)
3	0.5	19.82	439(3)	5554	4.9(8)
4	1	19.87	540(3)	5537	4.3(3)
5	1.3	19.84	417(1)	5534	4.5(3)
10	1.5	20	228(1)	5396	1.4(1)

527 nm. This damping is a convolution of the weaker signal due to the absorption of the probe with increased penetration depth and weakened reflection at the acoustic pulse due to phonon attenuation. In the literature the absorption coefficient at 820 nm is reported to be between $\approx 3 \cdot 10^4\,\text{cm}^{-1}$ [Eva69], which corresponds to an absorption depth between 250 and 500 nm - in good agreement with the measurement. The weakened probe absorption may stem from the non-equilibrium electron system due to the high repetition rate of the lasers.

To investigate the temperature dependence of the damping time, i.e. the absorption depths and attenuation length, further measurements were performed with pump powers of 3, 4, and 5 mW. The corresponding probe powers were 0.5, 1, and 1.3 mW. The results are shown in Table 8.1. An increased pump and probe power will lead to a higher temperature in the system. One sees a slight increase in the Brillouin frequency for higher temperatures suggesting either an increase of the speed of sound, or the refractive index. But the effect of temperature is even more pronounced in the lifetimes. While the noise floor is not negligible for the 3 mW measurement, for other powers a clear reciprocal dependence of lifetime with laser power - and thus with temperature - is visible. By doubling the power, the lifetime is reduced by half. This may be due to the increased thermal phonon population.

8.2.2. Optical phonons

The high frequency mode at 5.4 THz is Raman-active, an optical phonon. Optical phonons are described by oscillations within the unit cell of the lattice. The active atoms move opposite to each other and, depending on the charge, a dipole moment can be present leading to an infrared-active mode, or no dipole moment leading to a Raman-active mode. These can be measured in the steady state by Raman spectroscopy. A spectrally very sharp laser with the frequency ω_L illuminates the sample. The reflected light is incident on a spectrum analyzer. By filtering out the directly reflected light with the frequency ω_L it becomes apparent in the measurement that additional frequencies are detected at $\omega_S = \omega_L - \omega_{op}$ and $\omega_A = \omega_L + \omega_{op}$. Either the photon will excite an optical phonon with the frequency ω_{op} - giving rise to the Stokes peak in the spectrum - or absorb an optical phonon, called the Anti-Stokes peak. This process is limited by momentum conservation as the laser light has a very small wave vector compared to the Brillouin-zone size and thus only modes near the Brillouin-zone center can be measured. This is a spontaneous process and only a small fraction of the incident laser light will be Raman scattered. The scattering intensity can be expressed by the Raman tensor $\boldsymbol{R}$. It describes the symmetry and transition probabilities between the incident light polarization ($\vec{e_i}$)

and the scattered light polarization ($\vec{e_s}$):

$$I_S \propto |\vec{e_s} \cdot \boldsymbol{R} \cdot \vec{e_i}|^2. \tag{8.2}$$

Modes with a symmetric Raman tensor- independent of the polarization - are called A-modes and modes with a polarization dependency are called E-modes. The index g denotes the ground state.

For time-domain measurements the spontaneous Raman efficiency would be too low. To excite coherent optical phonons different processes are proposed: (i) Impulsive stimulated Raman scattering (ISRS) utilizes a pump pulse spectrally broader than the frequency of the optical phonons in the system, so both ω_L and ω_S are present. By stimulated Raman scattering the ω_L laser line will transmit its energy into the ω_S laser line emitting an optical phonon at the difference frequency $\omega_{op} = \omega_L - \omega_S$. The optical pulse has to be shorter than the frequency of the optical phonon to allow for coherent excitation. (ii) Displacive excitation of coherent phonons (DECP) utilizes the initial fast heating of the electronic systems (see Section 3.2). The new quasi-equilibrium gives rise to a displacement of the nuclei without changing the lattice's symmetry, allowing only the excitation of A modes [Zei92]. (iii) A third process is the Placzek effect, where the dipole moment of the unit cell gives rise to a polarization force, allowing the excitation of E modes [Gar08].

The optical phonon measured before has a frequency at 5.40 THz, which corresponds to an A_{1g}-mode [Had13]. The measurement is compared to a Raman spectrum taken of the sample with a MonoVista CRS (S & I). The 632.8 nm laser line of a HeNe-laser was used to measure the backscattered light of the 2 µm laser spot with 2 mW laser power. A notch filter at the laser wavelength suppresses the directly reflected light. The residual scattered light is spectrally broken up by a diffraction grating with 600 lines per mm. The spectrum is measured with a liquid-nitrogen cooled detector.

In Fig. 8.2(a) the measured Raman spectrum is shown. Three peaks at 3.3, 5.7, and 7 THz can be seen, where the 5.7 THz peak has the highest amplitude. It can be interpreted likewise to the time-resolved measurement to be the A_{1g}-mode. The slightly higher frequency can be attributed to the lower temperature of the sample. In Table 8.1 the A_{1g} mode's frequency is stated for different pump and probe powers. A clear dependence on the laser power, i.e. the sample's temperature can be seen. This is in agreement with previous temperature-dependent Raman measurements on few layers of $SnSe_2$ by Pawbake et al. [Paw16]. They measured a red shift with higher temperature and also a broadening of the Raman peak. This can be corroborated in the time-domain measurements. For all four measurements the first oscillation was fitted with a dampened sine and the lifetime of the A_{1g} was extracted. The results are given in Table 8.1. A pronounced drop in lifetime with higher laser powers can be seen.

To allocate the other two Raman modes, the dispersion relation, calculated by density functional perturbation theory [Had13], is shown in Fig. 8.2(b). The overlap of the 3.3 THz mode and the 5.7 THz (A_{1g}) and the Brillouin center is perfect. Thus, the 3.3 THz mode can be clearly assigned as E_g mode. Yet, the 7 THz mode, shown as the dashed gray line in the dispersion relation, does not fit to any mode given by the dispersion relation. However, for bare Se in special structures, like an n-fold chain (Se_n) or trigonal Se (t-Se), a Raman peak at ≈ 7 THz is found [Oli12, Sin14]. Although the spot's position in the microscope image of the Raman spectrometer looked fine, the material might be damaged, or surface defects may lead to the formation of segregated

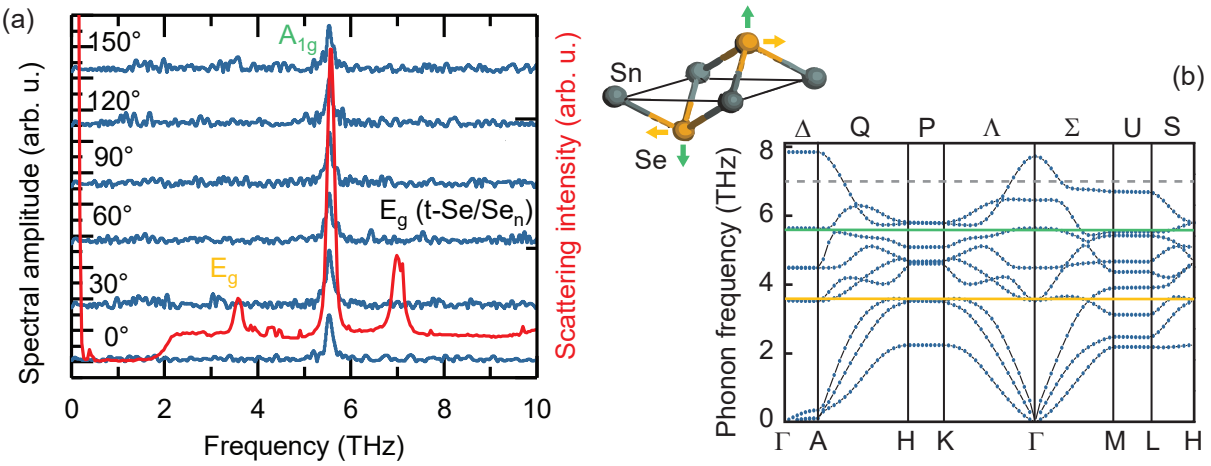

Figure 8.2.: (a) Fourier transformations of the first time regime for different polarizations between zero and 150 degree (blue). Superimposed is the Raman spectrum (red). (b) Dispersion relation of $SnSe_2$ adapted from [Had13]. Two frequencies are marked: E_g (yellow) and A_{1g} (green), whose oscillation direction is shown in the schematic graph. The dashed line corresponds to the third measured Raman frequency.

Se-clusters.
Lastly, to check for the E_g modes in the time domain-data, polarization dependent measurements were performed. A $\lambda/2$ wave plate was introduced in the setup in the vicinity of the microscope objective. By turning the half-wave plate a polarization change of both the pump and probe could be introduced. The measurement was repeated for a whole polarization change of 180 ° in steps of 30 °. The results are shown in Fig. 8.2(a). The A_{1g} mode is present in all measurements, but no additional modes arise. While for the higher frequency mode the time resolution of the setup may not be sufficient, in the polarization dependent measurement the lower frequency mode should be measurable. However, the lower symmetry and higher order processes may suppress the signal. An anisotropic measurement scheme could enhance the sensitivity of asymmetric modes enough, but did not work utilizing the setup used here [Dek95]. A higher pump intensity would be necessary and could be included by dismissing the microscope objective and using larger spot sizes. This would reduce the induced power per area.

8.3. Conclusion

In this chapter, the first pump-probe measurements on $SnSe_2$ measuring coherent optical phonons were presented. The A_{1g}-mode is measured at 5.5 THz at ambient conditions with a lifetime of $t_{A1g} = 4.9(8)$ ps. This frequency is corroborated by calculations of the dispersion relation by density functional perturbation theory and Raman scattering measurements. A clear negative shift of the frequency and the lifetime with temperature was observed. In the Raman measurement two additional optical modes at 3.7 and 7.0 THz were detected and the 3.7 THz mode could be attributed to the E_g mode. However, the 7 THz mode has not been measured in $SnSe_2$ crystals before and is assumed to be an optical phonon of distinct Se-formations.
Additionally, the Brillouin mode could be measured at 20 GHz, suggesting a speed of sound of $v_L = 2310$ m/s for longitudinal acoustic phonons parallel to the c-axis in $SnSe_2$, in good agreement with the literature. The lifetime is found to be temperature dependent but further measurements have to be made to quantify this influence and define a damage threshold for this system.

Chapter 9

Summary

Before I came here I was confused about this subject. Having listened to your lecture I am still confused. But on a higher level.
- *Enrico Fermi*

In this thesis hypersonic impulsively generated phonons are utilized to study eigenmodes, dissipation, adhesion, and spectral transformations of acoustic pulses. Acoustic phonons in the GHz range and optical phonons in the THz range are generated by an optical pump pulse. An optical time-delayed probe pulse detects the temporal response of the sample. The laser cavities, which produce the pump and probe pulses, have a slight repetition rate offset, which enables a consecutively ramped time delay between both pulses. Thus, a time resolved measurement of the sample's response is obtained. The technique is known as asynchronous optical sampling (ASOPS). The investigated and different prepared material systems, their special properties and the advances to the field of picosecond ultrasonics, i.e. for non-destructing testing, are presented in the following. As main results, frequency-dependent lifetimes measured for the investigated nanoscopic material systems (monolayer, bilayers with different adhesion) are obtained.

Roughened membranes: To understand the influence of surface roughness on lifetimes of longitudinal acoustic modes, Si membranes with different roughnesses are prepared. By Ar^+ ion milling of the surface with an acceleration voltage of 300-800 V and a flux of $1.2 \times 10^{17}/\mathrm{cm}^2$ the surface is restructured. Atomic force microscope measurements are employed to determine the roughness topology. Two distinct features become apparent: on a small area ($\approx$ atomic scale) incoherent height variations, e.g. roughness, are visible whereas on a larger area ($> 20 \times 20\,\mathrm{nm}^2$) a coherent waviness, e.g. a small changing slope of the surface, appears, called ripples. An 80 MHz pump-probe setup utilizing the asynchronous optical sampling principle is introduced to measure frequencies from 12 up to 263 GHz and corresponding lifetimes from 12 down to 0.1 ns. For all investigated samples the lifetimes resemble mostly a $1/\omega$-decay. Therefore, for every sample the quality factor ($Q = \omega\tau$) is nearly constant between 50 and 150 for all its modes. Comparing the quality factors of the different samples yields a small correlation to the roughness. Hence, it can be concluded that the influence of surface roughness is not as pronounced as assumed in the literature. A larger roughness corresponds to a smaller Q. However, for the ripples and their period no correlation can be seen. This is the first measurement using multiple acoustic eigenmodes of a membrane to characterize frequency-dependent phonon lifetimes.

Bilayer membrane (perfect adhesion): Measuring acoustic pulses in bilayer systems allows quantitative determination of values of thicknesses, impedances, absolute lifetimes, and a detailed observation of detection processes to be obtained. Four Si membranes covered with diverse Al films are fabricated. The thicknesses of the Al films are chosen so that the thickest one fully absorbs the pump light, while the other thicknesses allow for exciting the Si membrane as well. All but the thinnest Al films do not allow the probe pulse to pass through twice. Thus, the thinnest Al film enables the transition to a different detection scheme because the probe light reflected at the back surface of the membrane can be detected as well.

Upon optical excitation the Al film transducer generates a short acoustic pulse with a broad frequency spectrum. It propagates in the cavity built-up by the Al/air- and the Si/air surface getting repeatedly reflected. All repetitive incidents at the Al detection layer assemble a pulse train in the time domain. In the frequency domain a temporal pulse train corresponds to a frequency comb. Depending on the Al thickness the frequency combs span from 10 up to 500 GHz consisting of 11 up to 45 modes with a thicker Al film leading to less modes. The mode spacing is quasi-linear and given by the inverse round trip time in the bilayer. However, small deviations of the higher harmonics around this linear relation are observed. An analytical expression for this sinusoidal oscillation is derived depending only on the impedances and the individual round trip times for both layers. Perfect agreement with the experimental data is found: the impedance ratio defines the amplitude of the oscillation and the ratio of round trip times the period.

Furthermore, due to the clear temporal spacing of the pulses it is possible to compare the spectra of all pulses to each other. By fitting the Fourier amplitudes of up to 13 pulses with an exponential decay frequency-dependent lifetimes are obtained with great precision for the whole frequency range. A comparison of samples with different Al films indicates that the main dissipation occurs in the Al film. This is studied further in the case of imperfect adhesion. The lifetimes are comparable to values found in thin bare Si membranes. A detailed analysis of the pulse's spectra shows a nearly vanishing amplitude at lower frequencies. An analytical expression for the pulse shape is derived, in good agreement with the measurement. It is found that the dip arises from the concurring strain amplitudes of the acoustic pulses excited with different signs in Si and Al.

Bilayer membrane (imperfect adhesion): A non-destructive way to quantify adhesion and the respective lifetimes of each layer in a bilayer system is presented in the special case of an imperfectly adhered Al/Si-bilayer. Depending on the surface treatment and evaporation process of the Al film perfect or imperfect adhesion can be obtained. It is well known that imperfect adhesion can be qualitatively demonstrated by a fast decaying oscillation in the beginning of the measurement. It originates from the weak coupling between both layers and the impaired launching of the strain pulse from the Al film into the Si. This can be measured in the bilayer as well as a pulse train at later times in the time domain. Its corresponding frequency comb exhibits a pronounced dip at roughly the frequency of the Al film's fundamental mode (roughly the frequency of the oscillation in the beginning). However, the broad frequency spectrum of the acoustic pulses allows for a more precise determination of the adhesion strength than the oscillation in the beginning.

A spectral transfer function (STF) is derived, which describes the changes the acoustic pulse undergoes during one round trip in the bilayer. It includes dissipation in the Al and Si, perfect reflection at the Al/air and Si/air surfaces, and imperfect reflection and transmission at the

Al/Si-interface involving reverberations in the Al layer. The interface adhesion is incorporated by a spring model. The evaluation of the theoretical STF shows a pronounced dip at roughly the Al film's eigenmode frequency. By fitting the measured STF with the theoretical function a unique set of solutions can be found. This allows one to extract the dissipation in each layer and to quantify the adhesion strength between both layers. A comparison to alternative attenuation behaviors and different adhesion parameters corroborates the quality of the solution. In contrast to the modeling of the pulse's spectrum, the STF does not need any knowledge of the excitation or detection process, as long as the pulses are clearly separated in time.

For the interfacial adhesion a value for the spring constant of $\eta = 17\,\mathrm{kg\,nm^{-2}s^{-2}}$ is found. This is compared to the extraction of the adhesion by fitting the oscillation in the beginning of the measurement. When assuming that the oscillation stems from an increased reflection of the fundamental mode without any attenuation the spring constant is underestimated by a factor of 2 and the thickness is underestimated by 20 %. However, the adhesion result is in good agreement with literature values, where attenuation was neglected as well. The more detailed approach utilizing the STF yields for the lifetime at 240 GHz in polycrystalline Al $\tau_{Al} = 68\,\mathrm{ps}$ and a $1/\omega$-frequency dependence of the lifetime in Si with the value of $\tau_{Si} = 300/\omega$ from few GHz to 700 GHz. Those values are in good agreement with the literature, which shows the quality of the approach and hints to an exact extraction of the spring constant. However, further measurements have to be performed to corroborate these findings.

Lamb waves: Lamb waves are guided acoustic waves between the two surfaces of e.g. a Si membrane. In contrast to the other measurements presented in this thesis not only longitudinal phonons propagating perpendicular to the surface are detected. Instead, a superposition of longitudinal and transverse waves propagating in-plane, i.e. parallel to the surface, is detected. To generate a spatially modulated strain below the optical wavelength limit, Al gratings with periods below the optical wavelength are evaporated on a Si membrane. By excitation with a pump pulse an asymmetric strain distribution is imprinted on the membrane. The acoustic pulse and its wave vector is given by the inverse grating period, e.g. the spatial modulation. Grating periods between 100 and 500 nm and single stripes with widths between 1.5 and 5 µm are fabricated. The propagating Lamb waves are detectable with distances up to 55 µm between pump an probe spots. Frequencies between 10 and 200 GHz are generated. The results are compared to the theoretical dispersion relation of Si membranes and correspond quite well. Some frequencies, however, cannot be matched and are contributed to higher harmonics of the wave vector and thus wavelengths down to 50 nm. It is found that probing on a grating facilitates the detection of higher frequencies.

SnSe2: The first femtosecond pump-probe measurements on the transition metal dichalcogenide tin diselenide are performed. $SnSe_2$ consists of stacked nanosheets of a Sn monolayer sandwiched between two layers of Se. Progressive propagation of longitudinal acoustic phonons across the sheets is measured as Brillouin oscillation from which the speed of sound can be calculated to be: $v_\mathrm{L} = 2310\,\mathrm{m/s}$. For a solid this is a low value ($v_\mathrm{Al} \approx 6000\,\mathrm{m/s}$, $v_\mathrm{water} \approx 1500\,\mathrm{m/s}$), but it can be explained by the weak coupling between the single sheets and thus a low bulk modulus in this direction. The exponential decay of the oscillation is a convolution of the phonon attenuation and the optical absorption yielding an upper detection time limit of $\tau_\mathrm{Brillouin} \approx 500\,\mathrm{ps}$, which shortens by a factor of two upon heating the sample with a twofold increase of the pump power. This additionally indicates the weak heat conduction due to the weakly coupled sheets. Furthermore, three optical phonons are measured by Raman spectroscopy at 3.7, 5.5, and 7.0 THz. The

comparison with the dispersion relation identifies the 3.7 THz mode as an E_g-mode, whereas the 5.5 THz mode is identified as an A_{1g}-mode. The latter can also be determined by pump-probe measurements, where the lifetime is found to be 4.9 ps at the lowest pump power. For higher intensities the lifetime drops and a negative frequency shift of the mode is seen. Although the former modes can be explained easily, the latter mode at 7 THz can not be attributed to any mode of $SnSe_2$. It is, however, found in distinct Se-formations and, thus, hints to a recrystallization at the surface.

Conclusion & Outlook

In this thesis new experimental techniques and advanced theoretical tools were developed for the investigation of phonon dynamics. They allow for the further investigation and manipulation of nanostructures non-destructively.
A new technique to structure Si membranes enabled the development of innovative analysis methods: In bare Si membranes this enables the first determination of the lifetimes of the fundamental mode and its higher harmonics in one measurement. By comparison to the surface's topology it is found that the roughness does not influence the lifetimes as intensely as proposed so far in the literature. By using pump light with a shorter wavelength it is possible to excite short acoustic pulses. With these the lifetimes for a higher frequency regime would be extractable and, thus, a broader frequency spectrum could be characterized and compared to the theoretically predicted boundary scattering.
Al/Si bilayers are a versatile tool for the measurement of adhesion between two layers and their respective acoustic dissipation. For this system the adhesion can be described by a spring connecting both layers. A detailed analysis shows that only a unique set of parameters exist to describe the measurements. It is found that adhesion and attenuation are mutually dependent and have both to be taken into account for quantitative measurements. This advanced modeling approach eliminates the need to implement in detail the excitation and detection processes, which is a considerable progress in the evaluation of time-resolved opto-acoustic experiments in general. In addition, the presented modeling approach will be helpful especially for a better characterization and quantitative understanding of similar experiments. This includes for example thin film adhesion in a wide range of technical applications and fundamental research on 2D materials.
The study of guided waves in a Si membrane provides the highest generated frequencies of Lamb waves so far. These high frequencies and short wavelengths make it possible to test and evaluate thin membranes, to study fundamental problems of liquid rheology on membranes, and to probe the interaction of traveling acoustic waves with charge carriers and other type of excitations in solids in nanometer-confined geometries.
At last, one promising 2D material, SnSe2, is investigated in detail and insights on the lifetimes of acoustic and optical phonons are provided.
The knowledge of acoustic dissipation is of considerable importance for any applications based on phonon engineering at the nanoscale, e.g. opto-mechanical crystals or thermoelectric devices.

9.1. Zusammenfassung

In dieser Dissertation werden impulsiv erzeugte Phononen benutzt, um Eigenmoden, Dämpfung, Haftung und spektrale Transformationen von akustischen Impulsen zu untersuchen. Mithilfe eines optischen Anregeimpulses werden im GHz-Bereich akustische Phononen und im THz-Bereich optische Phononen erzeugt. Ein optischer (zeitverzögerter) Abfrageimpuls fragt die zeitliche Reflektivitätsantwort der Probe ab. Jeweils eine Laserkavität wird zur Erzeugung der Anrege- und Abfrageimpulse genutzt. Durch einen kleinen Versatz in den Repetitionsraten tritt ein fortlaufender Zeitversatz zwischen den jeweiligen Impulsen auf. Mit dieser Technik des asynchronen optischen Abtastens (englisch: asynchronous optical sampling: ASOPS) kann eine zeitaufgelöste Messung der Reflektivitätsantwort der Probe aufgenommen werden. Die untersuchten und verschieden hergestellten Materialsysteme, ihre speziellen Eigenschaften und die Fortschritte in der Untersuchungsmethode mit kohärenten akustischen Phononen, zum Beispiel für zerstörungsfreie Untersuchungen, werden im Folgenden präsentiert. Als bedeutendstes Resultat werden frequenzabhängigen Lebenszeiten für die verschiedenen untersuchten Materialsysteme (Si-Membrane und Zweischichtsysteme mit verschiedenen Haftungen) bestimmt.

Aufgeraute Membrane: Um den Einfluss von Rauheit auf die Lebenszeit von reflektierten longitudinalen akustischen Moden zu bestimmen, werden Si-Membrane mit verschiedenen Rauheiten hergestellt. Durch den Beschuss der Oberfläche mit Ar^+-Ionen mit einer Beschleunigungsspannung zwischen 300 und 800 V und einem Fluss von $1,2 \times 10^{17}\,\mathrm{cm}^{-2}$ wird die Oberfläche restrukturiert. Die räumliche Verteilung der Rauheit wird mit einem Rasterkraftmikroskop bestimmt. Zwei unterschiedliche Strukturen lassen sich feststellen: auf einer kleinen räumlichen Skala (entsprechend dem weniger Atomabstände) treten nicht zusammenhängende Höhenvariationen auf – im Allgemeinen Rauheit genannt; auf einer größeren Skala ($> 20 \times 20\,\mathrm{nm}^2$) tritt zusätzlich in einer Richtung eine gewisse Welligkeit auf. Mit Hilfe eines 80 MHz Anrege-Abfrage-Lasersystems von Laser Quantum werden Frequenzen zwischen 12 und 263 GHz gemessen und Lebenszeiten zwischen 12 und 0,1 ns bestimmt. Ein ungefährer $\tau \propto 1/\omega$-Abfall ist erkennbar, dem alle Messungen qualitativ entsprechen. Der Gütefaktor ($Q = \omega\tau$) ist daher nahezu konstant für die jeweilige Membran und bewegt sich zwischen 50 und 150. Der Vergleich der Gütefaktoren mit der Rauheit zeigt einen kleinen Trend, so dass einer höhere Rauheit zu einem niedrigeren Gütefaktor führt. Dieser Trend ist aber deutlicher kleiner als bisher in der Literatur vermutet. Der Vergleich der Lebenszeiten zur Wellenlänge der Welligkeit jedoch zeigt keinen Zusammenhang. Dies ist das erste Mal, dass mehrere akustische Eigenmoden einer Membran benutzt werden, um frequenzabhängige Phononenlebenszeiten zu bestimmen.

Zweischichtsystem (Perfekte Haftung): Die Messung von kohärenten akustischen Phononen in Zweischichtsystem erlaubt die Bestimmung von Dicken, Impedanzen und absoluten Lebenszeiten und eine eingehende Untersuchung des Detektionsprozesses. Vier Si-Membrane werden mit verschieden dicken Al-Schichten bedampft. Die Dicken sind so gewählt, dass der dickste Film das gesamte Anregungslicht absorbiert, während die dünneren Filme auch die Absorption im Silizium ermöglichen. Der dünnste Film ermöglicht zusätzlich, dass der Rückreflex des Abfrageimpulses von der Si/Luft-Grenzfläche auch durch den Al-Film transmittiert und somit Dickenschwingungen der ganzen Membran gemessen werden können.

Die Anregung des Al-Films mit dem Laserimpuls erzeugt einen kurzen akustischen Impuls mit einem breiten Frequenzspektrum. Der Impuls propagiert in der Kavität aus den Grenzflächen Al/Luft und Si/Luft hin und her. Das wiederholte Eintreffen in dem Al-Film sorgt für einen

detektierten Pulszug mit bis zu 13 Impulsen im Zeitbereich. Im Frequenzbereich entspricht ein zeitlicher Pulszug einem Frequenzkamm. In Abhängigkeit der Al-Schichtdicke reicht der Frequenzkamm von 10 bis 500 GHz mit 11 bis 45 verschiedenen Moden, wobei eine dickere Schicht weniger Moden generiert. Der Frequenzabstand der verschiedenen Moden ist quasilinear und durch die inverse Umlaufzeit im Zweischichtsystem gegeben. Bei genauerem Hinsehen werden aber Abweichungen von dem linearen Verlauf offensichtlich. Die sinusförmige Variation kann mit einer analytisch berechneten Formel beschrieben werden, die nur von den Impedanzen und den Umlaufzeiten in beiden Schichten abhängig ist. Eine perfekte Übereinstimmung tritt auf. Das Impedanzverhältnis bestimmt die Amplitude der Oszillation und das Umlaufzeitenverhältnis bestimmt die Periode.

Zusätzlich – da die Impulse im Pulszug klar getrennt sind – ist es möglich, die Spektren der einzelnen Impulse miteinander zu vergleichen. Für jede Frequenz können die Amplituden der einzelnen Pulsspektren mit einem exponentiellen Zerfall angenähert werden. Der Zerfall gibt direkt die frequenzabhängige Lebenszeit der einzelnen Proben wieder. Ein Vergleich der Lebenszeiten der Proben mit den verschieden dicken Al-Filmen zeigt, dass der bestimmende Dämpfungsprozess im Al-Film aufzutreten scheint. Dies wird ausführlicher bei der Untersuchung des Systems mit schlechter Haftung untersucht. Die extrahierten Lebenszeiten sind vergleichbar mit den Ergebnissen in reinen Si-Membranen.

Eine detaillierte Analyse der Pulsspektren zeigt zudem eine nahezu verschwindende Amplitude bei niedrigen Frequenzen. Eine Analyse der Erzeugung und Detektion des akustischen Impulses in dem Zweischichtsystem führt zu einem analytischen Ausdruck für das Spektrum, der zu einer guten Übereinstimmung mit dem Experiment führt. Das Verschwinden der Amplitude lässt sich darauf zurückführen, dass in Si und Al der Stress mit verschiedenem Vorzeichen generiert wird.

Zweischichtsystem (schwache Haftung): Eine zerstörungsfreie Methode, um die Haftung zwischen zwei Dünnschichten und die akustischen Lebenszeiten beider Schichten zu bestimmen, wird auf Grundlange eines Al/Si-Zweischichtsystems entwickelt. Der Herstellungsprozess bestimmt dabei die Haftungsqualität. In zeitaufgelösten Messungen kann schwache Haftung eines dünnen Filmes durch eine schnelle Oszillation am Beginn der Messung qualitativ nachgewiesen werden. Die Oszillation entspringt der Dickenschwingung des dünnen Filmes, die durch die verminderte Kopplung an die zweite Schicht nur langsam Energie verliert. Dies ist auch bei den wiederkehrenden Impulsen des Pulszuges zu sehen, die einige Nachschwinger aufweisen. Entsprechend zeigt der zugehörige Frequenzkamm eine Senke an ungefähr der Frequenz der Eigenmode des Al-Films, die etwa der Periode der Oszillation am Anfang entspricht. Eine tiefergehende Untersuchung zeigt, dass die Analyse des Pulszuges quantitativ genauere Werte liefert, als die Analyse der Oszillation am Anfang.

Eine spektrale Übertragungsfunktion (STF), die die Veränderung des akustischen Impulses während eines Umlaufs beschreibt, wird hergeleitet. Dämpfung im Al und Si, perfekte Reflektion an den Al/Luft- und Si/Luft-Grenzflächen und verminderte Haftung an der Al/Si-Grenzfläche werden angenommen. Die Haftung wird durch ein Federmodell modelliert. Die theoretische und experimentelle STF zeigen eine ausgeprägte Senke im Frequenzbereich der Eigenmode des Al-Filmes. Der Fit beider Funktionen liefert eine eindeutige Lösung mit einem spezifischen Satz von Parametern. Dadurch können eindeutig die Dämpfung und die Haftung in dem Zweischichtsystem quantitativ bestimmt werden. Ein graphischer Vergleich mit weiteren Dämpfungsmodellen und Federstärken zeigt die Güte der extrahierten Parameter. Im Gegensatz zur Simulation des Pulsspektrums benötigt die STF keine exakte Modellierung des Anrege- und Abfrageprozesses,

solange die Impulse in der Zeitdomäne klar separiert sind.

Für die Haftung wird eine Federkonstante von $\eta = 17\,\mathrm{kg\,nm^{-2}\,s^{-2}}$ bestimmt. Der Vergleich mit der Bestimmung der Federkonstante aus der Oszillation am Anfang – wo keine Dämpfung angenommen wird – zeigt, dass die Federkonstante um den Faktor 2 unterschätzt wird und die Al-Schichtdicke um 20 % unterschätzt wird. Diese Ergebnisse sind aber in guter Übereinstimmung mit Literaturwerten, in denen ebenfalls Dämpfung vernachlässigt wurde. Der präzisere Ansatz über die STF ergibt in polykristallinem Al bei 240 GHz für die akustische Lebenszeit $\tau_{\mathrm{Al}} = 68\,\mathrm{ps}$ und einen $1/\omega$-Verlauf der Lebenszeit in Si mit dem genauen Wert von $\tau_{\mathrm{Si}} = 300/\omega$ zwischen 10 und 700 GHz. Diese Werte sind in guter Übereinstimmung mit Werten aus der Literatur, in denen Einschichtsysteme untersucht wurden, und bestätigen die Qualität der entwickelten Analysemethode.

Lambwellen: Lambwellen sind geleitete akustische Wellen zwischen zwei Oberflächen von z.B. einer Si-Membran. Im Gegensatz zu den anderen Messungen, die in dieser Arbeit präsentiert werden, werden nicht nur longitudinale Phononen senkrecht zur Oberfläche propagierend detektiert. Stattdessen wird eine Superposition aus longitudinalen und transversalen Wellen, die sich parallel zur Oberfläche ausbreiten, gemessen. Um die angeregte räumlich modulierte Verspannung unterhalb des Beugungslimits zu bekommen, werden Al-Gitter mit einer Periode unterhalt der optischen Wellenlänge auf die Si-Membran aufgedampft. Bei der optischen Anregung wird eine asymmetrische Verspannungsverteilung in der Membran generiert. Der folgende akustische Impuls und der zugehörige Wellenvektor sind durch die inverse Gitterperiode gegeben – der räumlichen Modulation. Gitter mit Perioden zwischen 100 und 500 nm und einzelne Streifen mit Breiten zwischen 1,5 und 5 µm werden hergestellt. Die sich ausbreitenden Lambwellen werden bis zu Distanzen von 55 µm zwischen Anrege- und Abfrageimpuls detektiert. Dabei werden Frequenzen zwischen 10 und 200 GHz erreicht. Die Ergebnisse werden mit der theoretischen Dispersionskurve der Si-Membran verglichen und eine gute Übereinstimmung ist sichtbar. Einige Frequenzen können jedoch nicht direkt erklärt werden und werden einer höheren Harmonischen des Wellenvektors zugeordnet. Dadurch werden Wellenlängen bis zu 50 nm hinunter erreicht. Der Vergleich der Detektion von Gittern und einzelnen Streifen zeigt, dass Gitter die Detektion von hohen Frequenzen ermöglichen.

$SnSe_2$: Die ersten Femtosekunden Anrege-Abfrage-Experimente an dem Übergangsmetallchalkogenid Zinndiselenid werden ausgeübt. $SnSe_2$ besteht aus geschichteten Nanolagen bestehend aus Sn-Monolagen zwischen Se-Monolagen. Die Propagation von longitudinalen akustischen Phononen entlang der Lagen wird als Brillouin-Oszillation gemessen. Dadurch kann die longitudinale Schallgeschwindigkeit zu $v_{\mathrm{L}} = 2310\,\mathrm{m/s}$ bestimmt werden. Im Vergleich mit anderen Festkörpern ist das ein sehr geringer Wert (Al: $v_{\mathrm{Al}} \approx 6000\,\mathrm{m/s}$ und Wasser: $v_{\mathrm{Wasser}} \approx 1500\,\mathrm{m/s}$). Er kann aber durch die schwache Kopplung der einzelnen Lagen miteinander und damit einem kleinen Kompressionsmodul erklärt werden. Die exponentielle Abnahme der Oszillation ist eine Faltung der akustischen Dämpfung und der optischen Absorption, was für die akustische Dämpfung eine obere Grenze der Detektionszeit von $\tau_{\mathrm{Brillouin}} \approx 500\,\mathrm{ps}$ ergibt. Dieser Wert halbiert sich bei der doppelten Anregungsenergie und somit einer höheren Temperatur im System. Dadurch wird das Auftreten einer geringen Wärmeleitfähigkeit zwischen den einzelnen Lagen deutlich. Zusätzlich werden drei optische Phononen per Ramanspektroskopie gemessen. Durch Vergleich mit der Dispersionsrelation wird die Mode bei 3,7 THz als E_{g} identifiziert, während die Mode bei 5,5 THz der $A_{1\mathrm{g}}$-Mode zugeordnet wird. Die letztere Mode kann auch per Anrege-Abfrage-Spektroskopie gemessen werden. Die Lebenszeit wird dabei zu 4,9 ps bei der niedrigsten An-

regeleistung ermittelt. Bei höheren Intensitäten verringert sich die Lebenszeit; und die Frequenz der Mode schiebt zu geringeren Frequenzen. Die letzte gemessene Mode bei 7 THz kann keiner Mode der Dispersionsrelation von $SnSe_2$ zugeordnet werden. Der Vergleich mit Ramanspektren von verschiedenen Se-Komplexen spricht dafür, dass eine Oberflächenrestrukturierung stattfindet.

Fazit & Ausblick

In dieser Arbeit wurden neue experimentelle Methoden und fortgeschrittene theoretische Modelle entwickelt. Diese erlauben weitere zerstörungsfreie Untersuchungen und Manipulationen von Nanostrukturen.
Eine neue Technik zur Strukturierung von Si-Membranen ermöglichte die Entwicklung von innovativen Analysemethoden, die im Folgenden dargestellt werden. In puren Si-Membranen ermöglicht dies die erste Bestimmung der Lebenszeiten der Grundmode und ihrer höheren Harmonischen in einer einzigen Messung. Der Vergleich der Lebenszeiten mit der Rauheit zeigt, dass die Korrelation vorhanden, aber nicht so stark ist wie bisher angenommen. Mit einer kürzeren Anregewellenlänge sollte es möglich sein, höherfrequente akustische Impulse zu erzeugen, um eine größere Frequenzspanne bis jenseits von 200 GHz anzuregen, um den Einfluss der Grenzflächenstreuung genauer zu untersuchen.
Al/Si-Zweischichtsysteme sind ein vielseitiges Hilfsmittel, um die Haftung zwischen zwei Schichten und ihre jeweilige Dämpfung zu untersuchen. Die Haftung kann mittels eines Federmodells zwischen beiden Schichten beschrieben werden und das Modell liefert einen eindeutigen Satz an Lösungen. Insbesondere reichen nur Dämpfung oder nur das Federmodell nicht aus, um die Messungen quantitativ zu beschreiben. Dieser neuartige Ansatz mit der spektralen Übertragungsfunktion braucht keine Detailkenntnisse über die Anrege- und Abfrageprozesse, was zeitaufgelöste optoakustische Experimente deutlich vereinfachen könnte. Zusätzlich wird der entwickelte Modellansatz die Charakterisierung und das quantitative Verständnis von ähnlichen Experimenten deutlich vereinfachen. Dies beinhaltet die Haftung von dünnen Schichten, die in technischen Applikation eine große Rolle spielt, und aber auch die Grundlagenforschung an 2D-Materialien.
Die Untersuchung von geleiteten akustischen Wellen in Si-Membranen führte zu den bisher am höchsten generierten Frequenzen von Lambwellen. Diese hohen Frequenzen und kurzen Wellenlängen erlauben es, dünne Membrane zu charakterisieren, Grundlagenprobleme der Strömungslehre auf Membranen zu untersuchen und zu beeinflussen und die Wechselwirkung von Ladungsträgern und anderen Anregungen in Festkörpern mit akustischen Wellen in Nanostrukturen zu untersuchen.
Die Untersuchung des vielversprechenden 2D-Materials $SnSe_2$ erlaubt Einblicke in die Lebenszeiten und den Wärmetransport von akustischen und optischen Phononen. Das Wissen um akustische Dämpfung ist von besonderer Bedeutung für jegliche Anwendungen bezüglich Phononen in Nanostrukturen, z.B. in optomechanischen Kristallen oder thermoelektrischen Bauelementen.

Appendix

A.1. Material parameters and Si dispersion

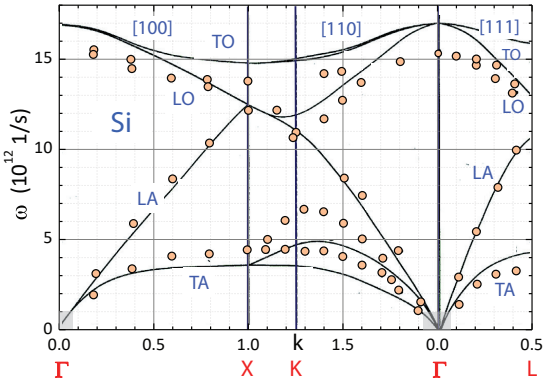

Figure A.1.: Phonon dispersion relation of Si. The lines show the ab-initio calculated dispersion and the dots indicate the experimental values from inelastic neutron scattering. The wave vector k is in units of $2\pi/a$, $\sqrt{2}2\pi/a$, and $\sqrt{3}2\pi/a$ for the [100], [110], and [111] direction (source: [Van85, Gro12]).

The theory in this thesis is limited to linear wave propagation. In Fig. A.1 the entire dispersion relation for Si is shown. The gray shaded areas at the bottom left mark the wave vectors used in this thesis. A linear dispersion relation can be seen.

	ρ $(\frac{\mathrm{g}}{\mathrm{cm}^3})$	v_L m/s	v_T m/s
Si [100]	2.3 [Mor96]	8430 [Mor96]	5840 [Dol03]
Al	2.69 [Li14]	6320 [Che89]	3040 [Li14]
	n ($\lambda = 800\,\mathrm{nm}$)	α ($\lambda = 800\,\mathrm{nm}$) $10^2\,/\mathrm{cm}$	β (T = 300 K) $10^{-6}\,/\mathrm{K}$
Si [100]	3.69 [Gre95]	8.5 [Gre95]	23 [Lyo08]
Al	2.77 [Rak95]	13120 [Rak95]	2.6 [Kro77]

Table A.1.: Material parameters of Silicon and Aluminum.

A.2. Compendium of acoustic phonon lifetimes in Si

In Fig. A.2 longitudinal acoustic phonon lifetimes in Si for different geometries are shown. The data stems from values found in the literature, calculated from theory, and data obtained in this thesis. In earlier experiments by Duquesne et al. (Daly et al.) measured the dissipation of an acoustic pulse during one round trip in bulk Si of 110 µm and 198 µm (50 µm) thickness. The acoustic pulses were generated and detected in a 30 nm (20 nm) thick Al film on the surface [Duq03, Dal09]. Later experiments from Bruchhausen et al. and Cuffe et al. determined the decay of the fundamental longitudinal acoustic eigenmode of a pure Si membrane of 222 nm thickness [Bru11] and thicknesses between 7.7 and 194 nm [Cuf13]. Maznev et al. determined the decay of a short acoustic pulse – generated due to the short absorption length of highly energetic light – in Si membranes between 0.4 and 15.3 µm [Maz15].
The values obtained in this thesis are taken from the measurements of different systems with 330 to 350 nm thick Si membranes as main component. The fundamental mode is measured on a bare membrane with smooth surfaces (Roughness: $T_{2.0}$). The other measurements evaluated acoustic pulses generated and detected in an evaporated Al film.: Perfectly adhered Al films with 17 and 40 nm thickness as well as a 13 nm thick Al film weakly adhered to the membrane (Adhesion fit).
The theoretical predictions for surface-roughness induced dissipation, Akhieser attenuation, three-phonon decay, and thermoelastic damping (TED) are discussed in detail in Section 2.7. In Fig. A.2 the evaluated upper lifetimes for a 300 nm thick Si membrane with 1 nm root-mean-square surface roughness are shown.
There are still some open questions within the calculation of the three-phonon decay damping time: The Debye approximation is used for the theoretical value, which neglects changes in the phonon density of states, which was claimed to yield reasonable results for thicknesses above 30 nm [Cuf13]. The values obtained by Daly et al. should also be limited by this behavior, but are above the limit – suggesting a different decay process.

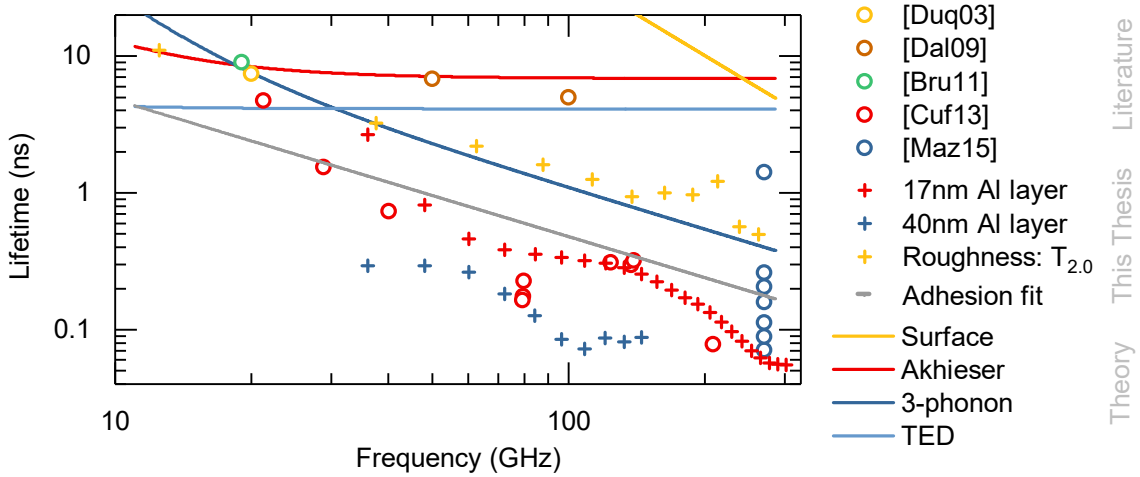

Figure A.2.: Comparison of the longitudinal acoustic phonon lifetimes in different Si geometries: literature values, selected measurements performed during this thesis, and theoretical predictions. Further details are given in the text.

A.3. List of publications

1. K. A. Wepasnick, X. Li, T. Mangler, S. Noessner, C. Wolke, M. Grossmann, G. Gantefoer, D. H. Fairbrother, and K. H. Bowen, *Surface Morphologies of Size-Selected Mo100±2.5 and (MoO3)67±1.5 Clusters Soft-Landed onto HOPG*, The Journal of Physical Chemistry C **115**, 12299–12307 (2011).

2. A. Bruchhausen, J. Lloyd-Hughes, M. Hettich, R. Gebs, M. Grossmann, O. Ristow, A. Bartels, M. Fischer, M. Beck, G. Scalari, J. Faist, A. Rudra, P. Gallo, E. Kapon, and T. Dekorsy, *Investigation of coherent acoustic phonons in Terahertz quantum cascade laser structures using femtosecond pump-probe spectroscopy*, Journal of Applied Physics **112**, 033517 (2012).

3. M. Schubert, M. Grossmann, O. Ristow, M. Hettich, A. Bruchhausen, E. C. S. Barretto, E. Scheer, V. Gusev, and T. Dekorsy, *Spatial-temporally resolved high-frequency surface acoustic waves on silicon investigated by femtosecond spectroscopy*, Applied Physics Letters **101**, 013108 (2012).

4. M. Grossmann, M. Klingele, P. Scheel, O. Ristow, M. Hettich, C. He, R. Waitz, M. Schubert, A. Bruchhausen, V. Gusev, E. Scheer, and T. Dekorsy, *Femtosecond spectroscopy of acoustic frequency combs in the 100-GHz frequency range in Al/Si membranes*, Physical Review B **88**, 205202 (2013).

5. O. Ristow, M. Merklein, M. Grossmann, M. Hettich, M. Schubert, A. Bruchhausen, J. Grebing, A. Erbe, D. Mounier, V. Gusev, E. Scheer, T. Dekorsy, and E. C. S. Barretto, *Ultrafast spectroscopy of super high frequency mechanical modes of doubly clamped beams*, Applied Physics Letters **103**, 233114 (2013).

6. X. Tang, X. Li, Y. Wang, K. Wepasnick, A. Lim, D. H. Fairbrother, K. H. Bowen, T. Mangler, S. Noessner, C. Wolke, M. Grossmann, A. Koop, G. Gantefoer, B. Kiran, and A. K. Kandalam, *Size Selected Clusters on Surfaces*, Journal of Physics: Conference Series **438**, 012005 (2013).

7. C. He, M. Daniel, M. Grossmann, O. Ristow, D. Brick, M. Schubert, M. Albrecht, and T. Dekorsy, *Dynamics of coherent acoustic phonons in thin films of CoSb3 and partially filled YbxCo4Sb12 skutterudites*, Physical Review B **89**, 174303 (2014).

8. M. Schubert, M. Grossmann, C. He, D. Brick, P. Scheel, O. Ristow, V. Gusev, and T. Dekorsy, *Generation and detection of gigahertz acoustic oscillations in thin membranes*, Ultrasonics **56**, 109 (2015).

9. M. Grossmann, O. Ristow, M. Hettich, C. He, R. Waitz, E. Scheer, V. Gusev, T. Dekorsy, and M. Schubert, *Time-resolved detection of propagating Lamb waves in thin silicon membranes with frequencies up to 197 GHz*, Applied Physics Letters **106**, 171904 (2015).

10. C. He, M. Grossmann, D. Brick, M. Schubert, S. V. Novikov, C. Thomas Foxon, V. Gusev, A. J. Kent, and T. Dekorsy, *Study of confined coherent acoustic phonon modes in a free-standing cubic GaN membrane by femtosecond spectroscopy*, Applied Physics Letters **107** (2015).

11. M. Schubert, H. Schaefer, J. Mayer, A. Laptev, M. Hettich, M. Merklein, C. He, C. Rummel, O. Ristow, M. Grossmann, Y. Luo, V. Gusev, K. Samwer, M. Fonin, T. Dekorsy, and J. Demsar, *Collective Modes and Structural Modulation in Ni-Mn-Ga(Co) Martensite Thin Films Probed by Femtosecond Spectroscopy and Scanning Tunneling Microscopy*, Physical Review Letters **115**, 1–5 (2015).

12. S. Volz, J. Ordonez-Miranda, A. Shchepetov, M. Prunnila, J. Ahopelto, T. Pezeril, G. Vaudel, V. Gusev, P. Ruello, E. M. Weig, M. Schubert, M. Hettich, M. Grossmann, T. Dekorsy, F. Alzina, B. Graczykowski, E. Chavez-Angel, J. Sebastian Reparaz, M. R. Wagner, C. M. Sotomayor-Torres, S. Xiong, S. Neogi, and D. Donadio, *Nanophononics: state of the art and perspectives*, The European Physical Journal B **89**, 15 (2016).

13. M. Grossmann, M. Schubert, D. Brick, E. Scheer, M. Hettich, and T. Dekorsy, *Characterization of thin-film adhesion and phonon-lifetimes in Al / Si membranes by picosecond ultrasonics*, New Journal of Physics (2017).

14. C. He, O. Ristow, M. Grossmann, D. Brick, Y. Guo, M. Schubert, M. Hettich, V. Gusev, and T. Dekorsy, *Acoustic waves undetectable by transient reflectivity measurements*, Physical Review B **95**, 184302 (2017).

15. D. Brick, V. Engemaier, Y. Guo, M. Grossmann, G. Li, D. Grimm, O. G. Schmidt, M. Schubert, V. E. Gusev, M. Hettich, and T. Dekorsy, *Interface Adhesion and Structural Characterization of Rolled-up GaAs/In0.2Ga0.8As Multilayer Tubes by Coherent Phonon Spectroscopy*, Scientific Reports **7**, 5385 (2017).

16. D. Brick, E. Emre, M. Grossmann, T. Dekorsy, and M. Hettich, *Picosecond Photoacoustic Metrology of SiO2 and LiNbO3 Layer Systems Used for High Frequency Surface-Acoustic-Wave Filters*, Applied Sciences **7**, 822 (2017).

17. Y. Guo, D. Brick, M. Grossmann, M. Hettich, and T. Dekorsy, *Acoustic beam splitting at low GHz frequencies in a defect-free phononic crystal*, Applied Physics Letters **110**, 1–5 (2017).

A.4. Acknowledgments

I want to thank all the people who contributed to the creation and finalization of this thesis. Thus, I express my gratitude to

Prof. Dr. Thomas Dekorsy for being my supervisor, research guide, and pool of knowledge for all areas of research. For introducing me to the scientific community and the rich possibilities to present my work internationally. And especially for always giving me the right nudge in the right direction.

Prof. Dr. Vitalyi Gusev for being my second reviewer and deepening my understanding of phonon propagation physics. Without him most of the theoretical background in this thesis would not have been developed.

Dr. Oliver Ristow and Dr. Mike Hettich – my predecessors – for the introduction to the experimental setup and continued support during all following steps. This includes help in finishing publications and proof-reading this thesis.

Dr. Martin Schubert for supervising the acoustics part of AG Dekorsy and helping to find my own voice in the scientific community.

Matthias Hagner for his profound knowledge about and intense help during the fabrication and characterization of nearly all samples.

Patricia Scheel, Dr. Matthias Klingele, Christoph Widmann, Lukas Ebner, Susanne Sprenger, Daniel Möhrle, Jan Haberland, Wilhelm Jackel, and Paul Stritt – Bachelor, Master, and Diploma students. Many results in this thesis base on their work in fabrication of samples, optimizing the measurement setup, and doing measurements on their own.

Delia Brick for being a friend and a colleague and for always having a friendly ear during the occurring up-and-downs.

Dr. Dirk Heinecke, Oliver Kliebisch, Dr. Chuan He, and Dr. Nico Krauss for helping in the lab, discussing results, and contributing to a good working atmosphere.

Dr. Albrecht Bartels, Dr. Matthias Beck, Dr. Stefan Facsko, and Dr. Reimar Waitz for providing samples and measurement setups.

All secretaries in the physics department and in the administration for helping with bureaucratic processes.

My WG, my friends, my family, and Nora for all their support and love during all steps.

Bibliography

[Ada95] S. Adachi, S. Takeyama, and Y. Takagi, *Dual wavelength optical sampling technique for ultrafast transient bleaching spectroscopy*, Optics Communications **117**, 1–7 (1995).

[Akh39] A. Akhieser, *On the absorption of sound in solids*, Journal of Physics-USSR **1**, 277–287 (1939).

[Ant] S. Anthony, *IBM unveils world's first 5nm chip.*

[Ant02] G. Antonelli, P. Zannitto, and H. J. Maris, *New method for the generation of surface acoustic waves of high frequency*, Physica B: Condensed Matter **316-317**, 377–379 (2002).

[Ant06] G. A. Antonelli, B. Perrin, B. C. Daly, and D. G. Cahill, *Characterization of Mechanical and Thermal Properties Using Ultrafast Optical Metrology*, MRS Bulletin **31**, 607–613 (2006).

[Aul73a] B. A. Auld, *Acoustic Fields and Waves in Solids - Volume I*, Wiley, New York, 1973.

[Aul73b] B. A. Auld, *Acoustic Fields and Waves in Solids - Volume II*, Wiley, New York, 1973.

[Bar02] A. Barbara, P. Quémerais, E. Bustarret, and T. Lopez-Rios, *Optical transmission through subwavelength metallic gratings*, Physical Review B **66**, 161403 (2002).

[Bar07] A. Bartels, R. Cerna, C. Kistner, A. Thoma, F. Hudert, C. Janke, and T. Dekorsy, *Ultrafast time-domain spectroscopy based on high-speed asynchronous optical sampling*, Review of Scientific Instruments **78**, 035107 (2007).

[Bel08] L. E. Bell, *Cooling, Heating, Generating Power, and Recovering Waste Heat with Thermoelectric Systems*, Science **321**, 1457–1462 (2008).

[Bon01] B. Bonello, A. Ajinou, V. Richard, P. Djemia, and S. M. Cherif, *Surface acoustic waves in the GHz range generated by periodically patterned metallic stripes illuminated by an ultrashort laser pulse*, The Journal of the Acoustical Society of America **110**, 1943 (2001).

[Bre77] J. L. Brebner, S. Jandl, and B. M. Powell, *Acoustic phonons in SnSe2*, Il Nuovo Cimento B Series 11 **38**, 263–270 (1977).

[Bre78] W. Breckenridge, O. K. Malmin, W. L. Nikolai, and D. Oba, *A rapid "pump-and-probe" laser technique for determining state-resolved product distributions*, Chemical Physics Letters **59**, 38 (1978).

[Bru97] M. Bruel, B. Aspar, and A.-J. Auberton-Hervé, *Smart-Cut: A New Silicon On Insulator Material Technology Based on Hydrogen Implantation and Wafer Bonding*, Japanese Journal of Applied Physics **36**, 1636–1641 (1997).

[Bru11] A. Bruchhausen, R. Gebs, F. Hudert, D. Issenmann, G. Klatt, A. Bartels, O. Schecker, R. Waitz, A. Erbe, E. Scheer, J.-R. Huntzinger, A. Mlayah, and T. Dekorsy, *Subharmonic Resonant Optical Excitation of Confined Acoustic Modes in a Free-Standing Semiconductor Membrane at GHz Frequencies with a High-Repetition-Rate Femtosecond Laser*, Physical Review Letters **106**, 077401 (2011).

[Bry10] J. Bryner, T. Kehoe, J. Vollmann, L. Aebi, I. Wenke, and J. Dual, *Phonon attenuation in the GHz regime: Measurements and simulations with a visco-elastic material model*, Physics Procedia **3**, 343–350 (2010).

[Büy13] S. Büyükköse, B. Vratzov, J. van der Veen, P. V. Santos, and W. G. van der Wiel, *Ultrahigh-frequency surface acoustic wave generation for acoustic charge transport in silicon*, Applied Physics Letters **102**, 013112 (2013).

[Cep16] A. Cepellotti and N. Marzari, *Thermal Transport in Crystals as a Kinetic Theory of Relaxons*, Physical Review X **6**, 041013 (2016).

[Che89] E. J. Chern and H. T. C. Nielsen, *Generalized formulas for reflected pulse response of multilayered structures*, Journal of Applied Physics **66**, 2833 (1989).

[Chi03] T. K. Chini, F. Okuyama, M. Tanemura, and K. Nordlund, *Structural investigation of keV Ar-ion-induced surface ripples in Si by cross-sectional transmission electron microscopy*, Physical Review B **67** (2003).

[Cle03] A. N. Cleland, *Foundations of Nanomechanics: From Solid-State Theory to Device Applications*, Springer, 2003.

[CM10] E. A. Cerda-Méndez, D. N. Krizhanovskii, M. Wouters, R. Bradley, K. Biermann, K. Guda, R. Hey, P. V. Santos, D. Sarkar, and M. S. Skolnick, *Polariton Condensation in Dynamic Acoustic Lattices*, Physical Review Letters **105**, 116402 (2010).

[CS85] I. R. Cox-Smith, H. C. Liang, and R. O. Dillion, *Sound velocity in amorphous films of germanium and silicon*, Journal of Vacuum Science & Technology A: Vacuum, Surfaces, and Films **3**, 674–677 (1985).

[Cuf13] J. Cuffe, O. Ristow, E. Chávez, A. Shchepetov, P.-O. Chapuis, F. Alzina, M. Hettich, M. Prunnila, J. Ahopelto, T. Dekorsy, and C. M. Sotomayor-Torres, *Lifetimes of Confined Acoustic Phonons in Ultrathin Silicon Membranes*, Physical Review Letters **110**, 095503 (2013).

[Cus94] J. S. Custer, M. O. Thompson, D. C. Jacobson, J. M. Poate, S. Roorda, W. C. Sinke, and F. Spaepen, *Density of amorphous Si*, Applied Physics Letters **64**, 437–439 (1994).

[Dal09] B. C. Daly, K. Kang, Y. Wang, and D. G. Cahill, *Picosecond ultrasonic measurements of attenuation of longitudinal acoustic phonons in silicon*, Physical Review B **80**, 174112 (2009).

[De16] S. De, *Theory and simulation of surface effects on intrinsic dissipation*, University of Illinois at Urbana-Champaign, PhD thesis, 2016.

[Deh15] T. Dehoux, M. A. Ghanem, and O. F. Zouani, *Probing single-cell mechanics with picosecond ultrasonics*, Ultrasonics **56**, 160 (2015).

[Dek95] T. Dekorsy, H. Auer, C. Waschke, H. J. Bakker, H. G. Roskos, H. Kurz, V. Wagner, and P. Grosse, *Emission of submillimeter electromagnetic waves by coherent phonons*, Physical Review Letters **74**, 738–741 (1995).

[Dem11] J. Demsar and T. Dekorsy, *Carrier Dynamics in Bulk Semiconductors and Metals after Ultrashort Pulse Excitation*, Optical Techniques for Solid-State Materials Characterization, CRC Press, 2011.

[Dol03] P. Dold, M. Heidler, A. Drevermann, and G. Zimmermann, *In situ observation of growth interfaces by ultrasound*, Journal of Crystal Growth **256**, 352–360 (2003).

[Duq03] J.-Y. Duquesne and B. Perrin, *Ultrasonic attenuation in a quasicrystal studied by picosecond acoustics as a function of temperature and frequency*, Physical Review B **68**, 134205 (2003).

[Elz87] P. A. Elzinga, F. E. Lytle, Y. Jian, G. B. King, and N. M. Laurendeau, *Pump/Probe Spectroscopy by Asynchronous Optical Sampling*, Applied Spectroscopy **41**, 2 (1987).

[Eva69] B. L. Evans and R. A. Hazelwood, *Optical and electrical properties of SnSe2*, Journal of Physics D: Applied Physics **2**, 4–10 (1969).

[Eve16] A. G. Every, *Intersections of the Lamb mode dispersion curves of free isotropic plates*, The Journal of the Acoustical Society of America **139**, 1793–1798 (2016).

[Gar08] T. Garl, E. G. Gamaly, D. Boschetto, A. V. Rode, B. Luther-Davies, and A. Rousse, *Birth and decay of coherent optical phonons in femtosecond-laser-excited bismuth*, Phys. Rev. B **78**, 134302 (2008).

[Gau67] W. B. Gauster and D. H. Habing, *Electronic volume effect in silicon*, Physical Review Letters **18**, 1058–1061 (1967).

[Gel16] D. Gelda, J. Sadhu, M. G. Ghossoub, E. Ertekin, and S. Sinha, *Reducing extrinsic damping of surface acoustic waves at gigahertz frequencies*, Journal of Applied Physics **119**, 164301 (2016).

[Gra75] K. F. Graff, *Wave Motion in Elastic Solids*, Oxford Engineering Science Series, Clarendon Press, 1975.

[Gre95] M. A. Green and M. J. Keevers, *Optical properties of intrinsic silicon at 300 K*, Progress in Photovoltaics: Research and Applications **3**, 189–192 (1995).

[Gro08] J. Groenen, F. Poinsotte, A. Zwick, C. Sotomayor-Torres, M. Prunnila, and J. Ahopelto, *Inelastic light scattering by longitudinal acoustic phonons in thin silicon layers: From membranes to silicon-on-insulator structures*, Physical Review B **77**, 045420 (2008).

[Gro11] M. Großmann, *Kohärent akustische Anregung von Nanostrukturen*, Universität Konstanz, Diplomarbeit, 2011.

[Gro12] R. Gross and A. Marx, *Festkörperphysik*, Oldenbourg Wissenschaftsverlag GmbH, München, 2012.

[Hab15] J. Haberland, *Untersuchung der akustischen Dämpfungseigenschaften von Silizium mittels optischer Ultrakurzzeitspektroskopie*, Universität Konstanz, Masterarbeit, 2015.

[Had13] V. G. Hadjiev, D. De, H. B. Peng, J. Manongdo, and A. M. Guloy, *Phonon probe of local strains in SnSxSe2-x mixed crystals*, Physical Review B - Condensed Matter and Materials Physics **87**, 1–5 (2013).

[He15] C. He, *Ultrafast Dynamics of Coherent Phonons in Thin Films and Free-Standing Membranes*, Universität Konstanz, PhD thesis, 2015.

[Her54] C. Herring, *Role of Low-Energy Phonons in Thermal Conduction*, Physical Review **95**, 954–965 (1954).

[Her74] G. Herrmann, *R. D. Mindlin and applied mechanics*, Pergamon Press, New York, 1974.

[Her13] J. P. Heremans, M. S. Dresselhaus, L. E. Bell, and D. T. Morelli, *When thermoelectrics reached the nanoscale*, Nature Nanotechnology **8**, 471–473 (2013).

[Hoh00] J. Hohlfeld, S.-S. Wellershoff, J. Güdde, U. Conrad, V. Jähnke, and E. Matthias, *Electron and lattice dynamics following optical excitation of metals*, Chemical Physics **251**, 237–258 (2000).

[Hos99] J. L. Hostetler, A. N. Smith, D. M. Czajkowsky, and P. M. Norris, *Measurement of the electron-phonon coupling factor dependence on film thickness and grain size in Au, Cr, and Al.*, Applied optics **38**, 3614–3620 (1999).

[Hud09] F. Hudert, A. Bruchhausen, D. Issenmann, O. Schecker, R. Waitz, A. Erbe, E. Scheer, T. Dekorsy, A. Mlayah, and J.-R. Huntzinger, *Confined longitudinal acoustic phonon modes in free-standing Si membranes coherently excited by femtosecond laser pulses*, Physical Review B **79**, 201307 (2009).

[Imb14] M. Imboden and P. Mohanty, *Dissipation in nanoelectromechanical systems*, Physics Reports **534**, 89–146 (2014).

[Jeo99] S. Jeong and J. Bokor, *Ultrafast carrier dynamics near the Si(100)2x1 surface*, Physical Review B **59**, 4943–4951 (1999).

[Kar07] D. M. Karabacak, V. Yakhot, and K. L. Ekinci, *High-Frequency Nanofluidics: An Experimental Study Using Nanomechanical Resonators*, Physical Review Letters **98**, 254505 (2007).

[Kel08] A. Keller, S. Roßbach, S. Facsko, and W. Möller, *Simultaneous formation of two ripple modes on ion sputtered silicon*, Nanotechnology **19**, 135303 (2008).

[Kli13] M. Klingele, *Excitation and Detection of Coherent Phonons in Silicon Membrane based Material Systems by Femtosecond Pump and Probe Experiments*, Universität Konstanz, Master Thesis, 2013.

[Kor08] C. V. Korff Schmising, A. Harpoeth, N. Zhavoronkov, Z. Ansari, C. Aku-Leh, M. Woerner, T. Elsaesser, M. Bargheer, M. Schmidbauer, I. Vrejoiu, D. Hesse, and M. Alexe, *Ultrafast magnetostriction and phonon-mediated stress in a photoexcited ferromagnet*, Physical Review B - Condensed Matter and Materials Physics **78**, 1–4 (2008).

[Kro77] F. R. Kroeger and C. A. Swenson, *Absolute linear thermal-expansion measurements on copper and aluminum from 5 to 320 K*, Journal of Applied Physics **48**, 853 (1977).

[Lan37] L. Landau and G. Rumer, *Überschallabsorption in festen Körpern*, Physikalische Zeitschrift der Sowjetunion **11**, 1 (1937).

[Li12] Q. Li, K. Hoogeboom-Pot, D. Nardi, M. M. Murnane, H. C. Kapteyn, M. E. Siemens, E. H. Anderson, O. Hellwig, E. Dobisz, B. Gurney, R. Yang, and K. a. Nelson, *Generation and control of ultrashort-wavelength two-dimensional surface acoustic waves at nanoscale interfaces*, Physical Review B **85**, 195431 (2012).

[Li14] T. Li and M. Ueda, *Sound scattering of a plane wave obliquely incident on a cylinder*, The Journal of the Acoustical Society of America **86**, 2363–2368 (2014).

[Lia16] B. Liao, A. A. Maznev, K. A. Nelson, and G. Chen, *Photo-excited charge carriers suppress sub-terahertz phonon mode in silicon at room temperature*, Nature Communications **7**, 13174 (2016).

[Lin93] H. N. Lin, H. J. Maris, L. B. Freund, K. Y. Lee, H. Luhn, and D. P. Kern, *Study of vibrational modes of gold nanostructures by picosecond ultrasonics*, Journal of Applied Physics **73**, 37–45 (1993).

[Luc76] G. Lucovsky, J. Mikkelsen Jr, W. Liang, R. White, and R. Martin, *Optical phonon anisotropies in the layer crystals SnS2 and SnSe2*, Physical Review B **14** (1976).

[Lyo08] K. G. Lyon, G. L. Salinger, and C. A. S. K. White, *Linear thermal expansion measurements on silicon from 6 to 340 K*, Journal of Applied Physics **48** (2008).

[Lyt85] F. E. Lytle, R. Parrish, and W. Barnes, *An introduction to time-resolved pump/probe spectroscopy*, Applied Spectroscopy **39**, 444 (1985).

[Mar71] H. J. Maris, *Interaction of sound waves with thermal phonons in dielectric crystals*, Physical Acoustics **8**, 279–345 (1971).

[Mar76] A. A. Maradudin and D. L. Mills, *Attenuation of Rayleigh surface waves by surface roughness*, Applied Physics Letters **28**, 573–575 (1976).

[Mar11] H. J. Maris and S. Tamura, *Propagation of acoustic phonon solitons in nonmetallic crystals*, Physical Review B **84**, 024301 (2011).

[Mat15] O. Matsuda, M. Cristina, R. Li, and O. B. Wright, *Fundamentals of picosecond laser ultrasonics*, Ultrasonics **56**, 3–20 (2015).

[Maz13] A. A. Maznev, F. Hofmann, A. Jandl, K. Esfarjani, M. T. Bulsara, E. A. Fitzgerald, G. Chen, and K. A. Nelson, *Lifetime of sub-THz coherent acoustic phonons in a GaAs-AlAs superlattice*, Applied Physics Letters **102**, 041901 (2013).

[Maz14] A. A. Maznev, *Dirac cone dispersion of acoustic waves in plates without phononic crystals (L)*, J Acoust Soc Am **135**, 577–580 (2014).

[Maz15] A. Maznev, F. Hofmann, J. Cuffe, J. Eliason, and K. Nelson, *Lifetime of high-order thickness resonances of thin silicon membranes*, Ultrasonics **56**, 116–121 (2015).

[Mec12] C. Mechri, P. Ruello, and V. Gusev, *Confined coherent acoustic modes in a tubular nanoporous alumina film probed by picosecond acoustics methods*, New Journal of Physics **14**, 023048 (2012).

[Mor96] C. J. Morath and H. J. Maris, *Phonon attenuation in amorphous solids studied by picosecond ultrasonics*, Physical Review B **54**, 203–213 (1996).

[Nel82] K. A. Nelson, R. J. Dwayne Miller, D. R. Lutz, and M. D. Fayer, *Optical generation of tunable ultrasonic waves*, Journal of Applied Physics **53**, 1144 (1982).

[Neo15] S. Neogi, J. S. Reparaz, L. F. C. Pereira, B. Graczykowski, M. R. Wagner, M. Sledzinska, A. Shchepetov, M. Prunnila, J. Ahopelto, C. M. Sotomayor-torres, and D. Donadio, *Tuning Thermal Transport in Ultrathin Silicon Membranes by Surface Nanoscale Engineering*, ACS Nano **9**, 3820–3828 (2015).

[Nov04] K. S. Novoselov, A. K. Geim, S. V. Morozov, D. Jiang, Y. Zhang, S. V. Dubonos, I. V. Grigorieva, and A. A. Firsov, *Electric Field Effect in Atomically Thin Carbon Films*, Science **306**, 666–670 (2004).

[OI09] G. Ozaydin-Ince and K. F. Ludwig Jr, *In situ x-ray studies of native and Mo-seeded surface nanostructuring during ion bombardment of Si(100)*, Journal of Physics: Condensed Matter **21**, 224008 (2009).

[Oli12] E. C. Oliveira, E. Deflon, K. D. Machado, T. G. Silva, and A. S. Mangrich, *Structural, vibrational and optical studies on an amorphous Se90P10 alloy produced by mechanical alloying*, Journal of Physics: Condensed Matter **24**, 115802 (2012).

[Oma10] M. S. Omar and H. T. Taha, *Effects of nanoscale size dependent parameters on lattice thermal conductivity in Si nanowire*, Sadhana **35**, 177–193 (2010).

[Paw16] A. S. Pawbake, A. Date, S. R. Jadkar, and D. J. Late, *Temperature Dependent Raman Spectroscopy and Sensing Behavior of Few Layer SnSe 2 Nanosheets*, ChemistrySelect **1**, 5380–5387 (2016).

[Pei29] R. Peierls, *Zur kinetischen Theorie der Wärmeleitung in Kristallen*, Annalen der Physik **395**, 1055–1101 (1929).

[Pip55] A. B. Pippard, *Magazine and Journal of Science CXXII . Ultrasonic attenuation in metals*, The London, Edinburgh, and Dublin Philosophical Magazine and Journal of Science **46:381**, 1104–1114 (1955).

[Rak95] A. D. Rakić, *Algorithm for the determination of intrinsic optical constants of metal films: application to aluminum.*, Applied Optics **34**, 4755–67 (1995).

[Rei73] J. A. Reissland, *The physics of phonons*, Wiley-Interscience, 1973.

[Ret02] B. Rethfeld, A. Kaiser, M. Vicanek, and G. Simon, *Ultrafast dynamics of nonequilibrium electrons in metals under femtosecond laser irradiation*, Physical Review B **65**, 214303 (2002).

[Ris16] O. Ristow, *High-Frequency Acoustic Phonons in Confined Geometries*, Universität Konstanz, PhD thesis, 2016.

[Rog11] J. A. Rogers, M. G. Lagally, and R. G. Nuzzo, *Synthesis, assembly and applications of semiconductor nanomembranes.*, Nature **477**, 45–53 (2011).

[Ros00] J. L. Rose and P. B. Nagy, *Ultrasonic Waves in Solid Media*, no. 4, Cambridge University Press, Cambridge, apr 2000.

[Rue15] P. Ruello and V. E. Gusev, *Physical mechanisms of coherent acoustic phonons generation by ultrafast laser action*, Ultrasonics **56**, 21–35 (2015).

[Sab02] A. Sabbah and D. Riffe, *Femtosecond pump-probe reflectivity study of silicon carrier dynamics*, Physical Review B **66**, 165217 (2002).

[Sad10] J. Sadhu, J. H. Lee, and S. Sinha, *Frequency shift and attenuation of hypersonic surface acoustic phonons under metallic gratings*, Applied Physics Letters **97**, 133106 (2010).

[San11] H. Sanada, T. Sogawa, H. Gotoh, K. Onomitsu, M. Kohda, J. Nitta, and P. V. Santos, *Acoustically Induced Spin-Orbit Interactions Revealed by Two-Dimensional Imaging of Spin Transport in GaAs*, Physical Review Letters **106**, 216602 (2011).

[Sch12] M. Schubert, M. Grossmann, O. Ristow, M. Hettich, A. Bruchhausen, E. C. S. Barretto, E. Scheer, V. Gusev, and T. Dekorsy, *Spatial-temporally resolved high-frequency surface acoustic waves on silicon investigated by femtosecond spectroscopy*, Applied Physics Letters **101**, 013108 (2012).

[Sch15] M. Schubert, M. Grossmann, C. He, D. Brick, P. Scheel, O. Ristow, V. Gusev, and T. Dekorsy, *Generation and detection of gigahertz acoustic oscillations in thin membranes*, Ultrasonics **56**, 109 (2015).

[Sha99] J. Shah, *Ultrafast spectroscopy of semiconductors and semiconductor nanostructures*, Springer, 1999.

[Sim57] S. Simons, *The absorption of very high frequency sound in dielectric solids*, Mathematical Proceedings of the Cambridge Philosophical Society **53**, 702–716 (1957).

[Sin14] A. K. Sinha, A. K. Sasmal, S. K. Mehetor, M. Pradhan, and T. Pal, *Evolution of amorphous selenium nanoballs in silicone oil and their solvent induced morphological transformation*, Chemical Communications **50**, 15733–15736 (2014).

[Sny08] G. J. Snyder and E. S. Toberer, *Complex thermoelectric materials*, Nature Materials **7**, 105–114 (2008).

[Sri76] G. P. Srivastava, *Calculations of anharmonic phonon relaxation times*, Pramana **6**, 1–18 (1976).

[Ste70] R. G. Steg and P. G. Klemens, *Scattering of Rayleigh Waves by Surface Irregularities*, Physical Review Letters **24**, 381–383 (1970).

[Ste03] J. M. Steele, C. E. Moran, A. Lee, C. M. Aguirre, and N. J. Halas, *Metallodielectric gratings with subwavelength slots: Optical properties*, Physical Review B **68**, 205103 (2003).

[Str15] P. J. Stritt, *Realisierung eines Doppellasersystems für die Femtosekunden-Spektroskopie*, Universität Konstanz, Bachelorarbeit, 2015.

[Sun94] C.-K. Sun, F. Valle, L. H. Acioli, E. P. Ippen, and J. G. Fujimoto, *Femtosecond-tunable measurement of electron thermalization in gold*, Physical Review B **50**, 15337–15348 (1994).

[Tac06] T. Tachizaki, T. Muroya, O. Matsuda, Y. Sugawara, D. H. Hurley, and O. B. Wright, *Scanning ultrafast Sagnac interferometry for imaging two-dimensional surface wave propagation*, Review of Scientific Instruments **77**, 043713 (2006).

[Tak99] Y. Takagi and S. Adachi, *Subpicosecond optical sampling spectrometer using asynchronous tunable mode-locked lasers*, Review of Scientific Instruments **70**, 2218 (1999).

[Tam83] S.-I. Tamura, *Isotope scattering of dispersive phonons in Ge*, Physical Review B **27**, 858–866 (1983).

[Tas94] G. Tas and H. Maris, *Electron diffusion in metals studied by picosecond ultrasonics*, Physical Review B **49**, 15046 (1994).

[Tas98] G. Tas, J. J. Loomis, H. J. Maris, A. A. Bailes, and L. E. Seiberling, *Picosecond ultrasonics study of the modification of interfacial bonding by ion implantation*, Applied Physics Letters **72**, 2235–2237 (1998).

[Tho86] C. Thomsen, H. Grahn, H. Maris, and J. Tauc, *Surface generation and detection of phonons by picosecond light pulses*, Physical Review B **34**, 4129–4138 (1986).

[Tor04] C. M. S. Torres, A. Zwick, F. Poinsotte, J. Groenen, and M. Prunnila, *Observations of confined acoustic phonons in silicon membranes*, Phys. stat. sol. **1**, 2609–2612 (2004).

[Tru69] R. Truell, *Ultrasonic methods in solid state physics*, New York, N.Y. : Academic Press, 1969.

[Val07] F. Vallée, *Energy Exchange at Short Time Scales: Electron–Phonon Interactionsin Metals and Metallic Nanostructures*, Microscale and Nanoscale Heat Transfer, 309–332 (2007).

[Van85] P. E. Van Camp, V. E. Van Doren, and J. T. Devreese, *Ab initio phonon dispersion curves of Si*, Physical Review B **31**, 4089–4091 (1985).

[Ver06] S. S. Verbridge, L. M. Bellan, J. M. Parpia, and H. G. Craighead, *Optically Driven Resonance of Nanoscale Flexural Oscillators in Liquid*, Nano Letters **6**, 2109–2114 (2006).

[Vik67] I. A. Viktorov, *Rayleigh and Lamb Waves: Physical Theory and Applications*, Ultrasonic technology : a series of monographs, Plenum Press, 1967.

[Vin10] C. J. Vineis, A. Shakouri, A. Majumdar, and M. G. Kanatzidis, *Nanostructured Thermoelectrics: Big Efficiency Gains from Small Features*, Advanced Materials **22**, 3970–3980 (2010).

[Wai12a] R. Waitz, *Nanomembranen : Ein Prüfstand für Probleme aus der Nanophysik*, Universität Konstanz, PhD thesis, 2012.

[Wai12b] R. Waitz, S. Nößner, M. Hertkorn, O. Schecker, and E. Scheer, *Mode shape and dispersion relation of bending waves in thin silicon membranes*, Physical Review B **85**, 035324 (2012).

[Wan14] X. Wang and B. Huang, *Computational study of in-plane phonon transport in Si thin films.*, Scientific reports **4**, 6399 (2014).

[War10] A. Ward and D. A. Broido, *Intrinsic phonon relaxation times from first-principles studies of the thermal conductivities of Si and Ge*, Physical Review B **81**, 1–5 (2010).

[Wev06] M. Wevers and F. Fransens, *Ultrasonic Lamb Wave Inspection of Aircraft Components Using Integrated Optical Fibre Sensing Technology*, ECNDT, 1–10 (2006).

[Wid15] C. Widmann, *Zeitaufgelöste Spektroskopie akustischer Anregungen von Membranen*, Universität Konstanz, Masterarbeit, 2015.

[Wri95] O. B. Wright and V. E. Gusev, *Acoustic generation in crystalline silicon with femtosecond optical pulses*, Applied Physics Letters **66**, 1190 (1995).

[Yu10] P. Y. Yu and M. Cardona, *Fundamentals of semiconductors: physics and materials properties*, Springer Science & Business Media, 2010.

[Zei92] H. J. Zeiger, J. Vidal, T. K. Cheng, E. P. Ippen, G. Dresselhaus, and M. S. Dresselhaus, *Theory for displacive excitation of coherent phonons*, Phys. Rev. B **45**, 768–778 (1992).

[Zen38] C. Zener, *Internal friction in solids II. General theory of thermoelastic internal friction*, Physical Review **53**, 90–99 (1938).

[Zha14] L.-d. Zhao, V. P. Dravid, and M. G. Kanatzidis, *The panoscopic approach to high performance thermoelectrics*, Energy Environ. Sci. **7**, 251–268 (2014).

[Zho16] X. Zhou, Q. Zhang, L. Gan, H. Li, J. Xiong, and T. Zhai, *Booming Development of Group IV-VI Semiconductors: Fresh Blood of 2D family*, ChemistrySelect **1** (2016).

[Zim60] J. M. Ziman, *Electrons and phonons: the theory of transport phenomena in solids*, Oxford University Press, 1960.